IDENTIFICATION OF INERTIAL SENSOR ERROR PARAMETERS

A THESIS SUBMITTED TO
THE GRADUATE SCHOOL OF NATURAL AND APPLIED SCIENCES
OF
MIDDLE EAST TECHNICAL UNIVERSITY

BY

BAĞIŞ ALTINÖZ

IN PARTIAL FULFILLMENT OF THE REQUIREMENTS
FOR
THE DEGREE OF MASTER OF SCIENCE
IN
ELECTRICAL AND ELECTRONICS ENGINEERING

SEPTEMBER 2015

Approval of the thesis:

IDENTIFICATION OF INERTIAL SENSOR ERROR PARAMETERS

submitted by **BAĞIŞ ALTINÖZ** in partial fulfillment of the requirements for the degree of **Master of Science in Electrical and Electronics Engineering Department, Middle East Technical University** by,

Prof. Dr. Gülbin Dural Ünver _____
Dean**,** Graduate School of **Natural and Applied Sciences**

Prof. Dr. Gönül Turhan Sayan _____
Head of Department, **Electrical and Electronics Engineering**

Prof. Dr. M. Kemal Leblebicioğlu _____
Supervisor, **Electrical and Electronics Engineering Dept., METU**

Examining Committee Members:

Prof. Dr. Mübeccel Demirekler _____
Electrical and Electronics Engineering Dept., METU

Prof. Dr. M. Kemal Leblebicioğlu _____
Electrical and Electronics Engineering Dept., METU

Assoc. Prof. Dr. Umut Orguner _____
Electrical and Electronics Engineering Dept., METU

Assoc. Prof. Dr. Mustafa Doğan _____
Electrical and Electronics Engineering Dept., Başkent University

Asst. Prof. Dr. Yakup Özkazanç _____
Electrical and Electronics Engineering Dept., Hacettepe University

Date: 04/09/2015

I hereby declare that all information in this document has been obtained and presented in accordance with academic rules and ethical conduct. I also declare that, as required by these rules and conduct, I have fully cited and referenced all material and results that are not original to this work.

Name, Last name: Bağış ALTINÖZ

Signature:

ABSTRACT
IDENTIFICATION OF INERTIAL SENSOR ERROR PARAMETERS

Altınöz, Bağış

M.S., Department of Electrical and Electronics Engineering

Supervisor: Prof. Dr. Kemal Leblebicioğlu

September 2015, 169 Pages

Inertial sensors (gyroscopes and accelerometers) that are used in navigation systems have distinct error characteristics such as bias, scale factor, random walk, etc. Calibration and characterization tests are done with 2 or 3 axes rate tables in order to identify these errors. It is possible to utilize error characteristics of these devices, and the navigation accuracy is directly dependent on the accuracy of this identification process. In this thesis, inertial sensor error parameters are identified by a membership function based method which also uses Allan deviation parameters. Additionally, traditional line method is used to identify random error parameters. Different types of sensors are modeled according to the identified parameters and Allan deviation curves of simulated and real data are compared. Error identification techniques are used to decrease errors in fiber optic gyroscope.

Keywords: Inertial sensors, quantization error, fiber optic gyroscope, error compensation, membership functions ,Allan deviation.

ÖZ
ATALETSEL SENSÖR HATA PARAMETRELERİNİN TANIMLANMASI

Altınöz, Bağış

Yüksek Lisans, Elektrik ve Elektronik Mühendisliği Bölümü

Tez Yöneticisi: Prof. Dr. Kemal Leblebicioğlu

Eylül 2015, 169 Sayfa

Navigasyon sistemlerinde kullanılan ataletsel sensörler (dönüölçerler ve ivmeölçerler) sabit kayma, ölçeklendirme katsayısı ve rastgele yürüyüş gibi ayrı hata parametrelerine sahiptir. Hata parametrelerinin belirlenmesi için yapılan testler 2 ya da 3 eksenli dönü tablalarında gerçekleştirilmektedir. Navigasyon doğruluğu, hata belirleme işlemi ile direkt ilişkili olduğundan, bu cihazların hata özelliklerini faydalı kılmak mümkündür. Bu tezde, Allan sapma verilerini kullanan üyelik fonksiyonlarıyla rastgele hata parametreleri belirlenmiştir. Ek olarak, rastgele hataların belirlenmesinde genellikle kullanılan doğru yöntemiyle de hata parametreleri belirlenmiştir. Farklı tip sensörler belirlenen hata parametrelerine göre modellenmiştir ve gerçek sensör verileri ile benzetim verileri birbirlerine göre kıyaslanmıştır. Hata tanımlama yöntemleri fiber optic ataletsel algılayıcı hatalarının azaltılması için kullanılacaktır.

Anahtar Kelimeler: Nicemleme hatası, fiber optik dönüölçer, kalibrasyon, üyelik fonksiyonları, Allan sapma yöntemi.

To my family…

ACKNOWLEDGMENTS

I would like to express my gratitude and thanks to my supervisor Prof. Dr. Kemal LEBLEBİCİOĞLU who guided me throughout this work with his valuable comments, support, understanding and patience.

I would also like to express my greatest appreciation to M. Erçin ÖZGENECİ for his enthusiasm and inspiring advices which are guided me at the most critical parts of the study.

I extend my deepest thanks to Derya ÜNSAL, Yeşim GÜNHAN and Duygu DEMİRKOL for their endless support and friendship.

I would like to thank to Assoc. Prof. Mustafa DOĞAN and Asst. Prof. Dr. Gökhan SOYSAL for their helpful advises during modeling and error estimation phases. I am grateful to Şaziye ŞİRİNNAR and Celil ŞİRİNNAR for their never ending supports in my entire life. Special thanks to my friends, Damla PARLAR, Yusuf GÖÇMEN and Aslı GÖÇMEN, A.İlden AK, Sultan CAN for their motivation, patience and assists.

I am indebted to my parents and my sisters who have always enlightened me with their caring, understanding, wisdom and love through my entire life.

TABLE OF CONTENTS

LIST OF TABLES

TABLES

LIST OF FIGURES

FIGURES

LIST OF ABBREVIATIONS

mg: milli-g (gravity)

deg: degree(s)

s: second

IMU: Inertial Measurement Unit

FOG: Fiber Optic Gyroscope

RLG: Ring Laser Gyroscope

log: Natural Logarithm

AD: Allan Deviation

h: hour

m: meter

rad: radian

ppm: parts per million

CHAPTER 1

INTRODUCTION

1.1 Literature Survey

Navigation is a process that defines position, velocity or direction of a platform using information about a movement [1]. Throughout the history, some devices or landmarks which are used by human to reach true destination. Ancient people observed stars, mosses and anthills to learn their direction. Modern people have observed same environmental objects but big advances have been made in navigation technology after fabrication of electronic components. Global Navigation Satellite System (GNSS), magnetometers, barometers, altimeters and inertial sensors (e.g., accelerometers and gyroscopes) are examples of these advanced devices. Inertial navigation systems (INS) and GNSS are of great help in navigation, but these systems individually have several disadvantages.

GNSS determines the navigation parameters (e.g., velocity, position and attitude) with respect to the satellites, which are in orbit around the earth [2]. GNSS helps to produce very accurate navigation parameters but it can be jammed or signals from satellites can be very weak to produce true parameters in bad weather or in urban areas. In contrast to GNSS, inertial sensors cannot be jammed and always produce data.

IMU is the heart of the navigation process because it gives angular velocity and linear acceleration information to INS [1]. Angular velocity data is produced by gyroscopes and linear acceleration data is produced by accelerometers. INS algorithms integrate gyroscope and accelerometer outputs to generate navigation

parameters. Unfortunately, inertial sensor errors degrade the accuracy of navigation. These errors are divided into 2 parts: deterministic and random (stochastic) errors [3]. Deterministic part is usually the major error source and it depends mostly on temperature [4]. Deterministic errors are estimated and compensated through the calibration tests [4, 5]. Calibration tests are performed under different temperatures with two-axis rate table and a polynomial is obtained for each error source [4, 5]. IMU error compensation algorithm parameters are formed according to calibration tests. IMU error compensation algorithm is generally responsible from digital to physical data conversion, deterministic error degradation and digital filtering [6].

Random or stochastic errors also have considerable effects on measurement accuracy of inertial sensors; therefore, they have to be estimated properly. Random errors can be split into two categories: uncorrelated and correlated [7, 8]. Uncorrelated errors have white noise characteristics and correlated errors have random walk characteristic. Several models have been suggested [9, 10] to estimate random error parameters; but, the most well-known and standard method is Allan deviation method [11]. Yet, some important disturbances such as dithering and unexpected sinusoidal noises cause slightly inaccurate determination of IMU random error terms that are usually ignored ([11]). After obtaining random error parameters from Allan deviation curve, a dynamical mathematical model is used to model random errors [7, 12]. Accurate modeling of inertial sensor errors is essential because a designer meets cost and performance requirements according to error models.

Inertial sensor errors affect the IMU level such as navigation, tactical and control grade [2, 13]. Several types of inertial sensors have been produced with different technologies over the past two decades. Optical sensors, microelectromechanical sensors (MEMS), quartz sensors are widely used in navigation applications [14]. MEMS sensors are generally in the control level but optical sensors and quartz sensors are generally in the tactical level [14]. Navigation grade sensors are evaluated for long-range applications such that ballistic missiles and aircrafts [14].

1.2 Scope of this Study

Scope of this thesis is about identification and modeling of deterministic and stochastic errors of an inertial sensor. Some important comments about quantization error are given and confusions about this error are clarified. Autocorrelation function is generally used for identification of correlation time of bias instability, but autocorrelation is also used to investigate sinusoidal noise in this study. Power spectral density (PSD) shows different random error sources but it is mainly used to identify quantization error. Moreover, traditional line method has some problems; therefore, separate errors in their dominant time range give opportunity to identify the error parameters accurately. A simple modification to modeling Allan deviation curves has been suggested. Allan deviation curves of simulated data and real data are compared for validation of proposed estimation technique. Allan deviation curves of fiber optic gyroscopes, ring laser gyroscopes, MEMS and quartz IMUs are investigated to determine dominant random error sources for each sensor type. Temperature calibration is very important for all sensors and it has to be performed in rate tables to find deterministic error parameters. Real data examples demonstrate that determined error parameters decrease the total error levels.

1.3 Organization of the Thesis

Gyroscope and accelerometer technologies are explained in CHAPTER 2. Several sensor types are discussed in this chapter and general measurement principles are given. CHAPTER 3 presents important error terms, which have effect on the accuracy of navigation sensors. CHAPTER 4 investigates several error estimation techniques for random error sources. CHAPTER 5 discusses modeling issues and difference equations are generated to model an IMU error. In CHAPTER 6, stochastic error parameters are identified with two different methods for MEMS, quartz, ring laser gyro (RLG), and fiber optic gyro (FOG) sensors. CHAPTER 7

discusses temperature calibration for FOG sensor. This chapter also shows the effect of temperature calibration on the total error.

CHAPTER 2

INERTIAL SENSORS

An IMU contains different components such that gyroscopes, accelerometers, a processor and an integrated power supply [2, 13, 14]. Mostly, an IMU has three gyroscopes and three accelerometers that are placed perpendicularly to each other [2]. Digital filtering, size effect compensation, data type conversions, sampling are executed by the processor [14]. Therefore, performance of an IMU does not only depend on the capability of inertial sensors, but, true determination of error parameters and error compensation algorithm is also important. In this section, we concentrate on several sensor types and their measurement principles and structures.

2.1 Accelerometers

An accelerometer mainly has four parts to measure the specific force on it [1]. A proof mass moves along the case and it is attached to two springs that satisfy free movement environment for the proof mass [4]. A pick-off circuit generates electrical voltage proportional to applied acceleration [4]. In this way, total acceleration can be detected and it can be used for navigation. Figure 1 shows basic parts of an accelerometer at equilibrium state.

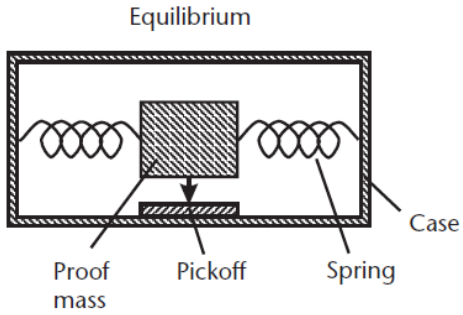

Figure 1 Components of an accelerometer [2] .

In Figure 2 , a force is applied on the accelerometer and proof mass moves left side of the case. In that case, 1g value is read from the accelerometer. An accelerometer can be used to measure the gravitational acceleration as shown in Figure 3. Specific force equation is given by,

$$f = a - g \tag{2.1}$$

f = *specific force*
g = *gravitational force*
a = *acceleration at the inertial frame*

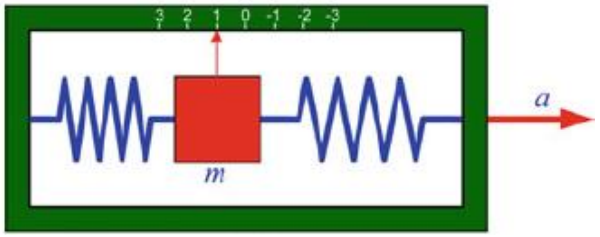

Figure 2 Linear acceleration is applied to accelerometer and it causes positive acceleration [13].

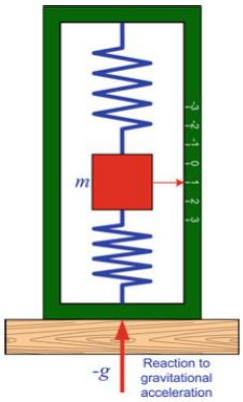

Figure 3 Gravitational force measurement of an accelerometer [13].

There are different types of the accelerometers such as mechanical and solid-state. Although, mechanical accelerometers still provide very accurate measurements, MEMS accelerometers are widely used because their error levels are acceptable and their costs are very low.

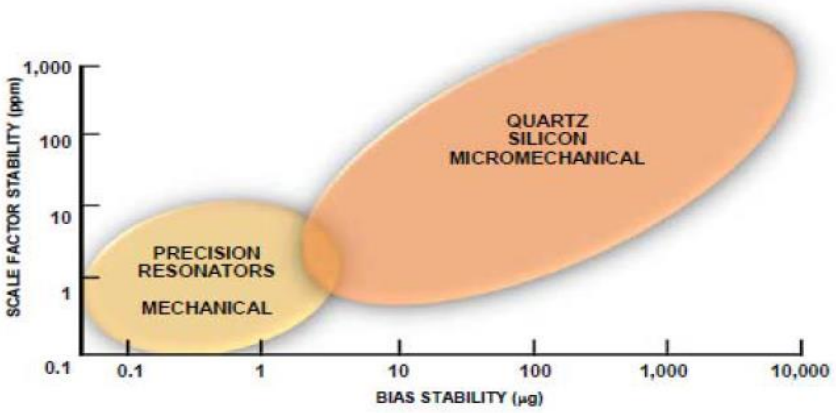

Figure 4 Current error levels of different accelerometer technologies [15].

As shown in Figure 4, solid-state sensors have very low error levels and they will replace mechanical sensors in the future. Solid-state accelerometers can be divided into three categories: piezoresistive accelerometers, piezoelectric accelerometers, and capacitive accelerometers [14].

Capacitive accelerometers work similar to mechanical accelerometers but their measurement principle is different. Two 180 degrees out-of-phase signals are applied to capacitive fingers. Capacitance changes between fingers when force is applied to pendulous mass as shown in Figure 5. Due to the capacitive change, phase difference increase or decrease according to direction of movement [16]. Then, demodulation of phase difference generates voltage.

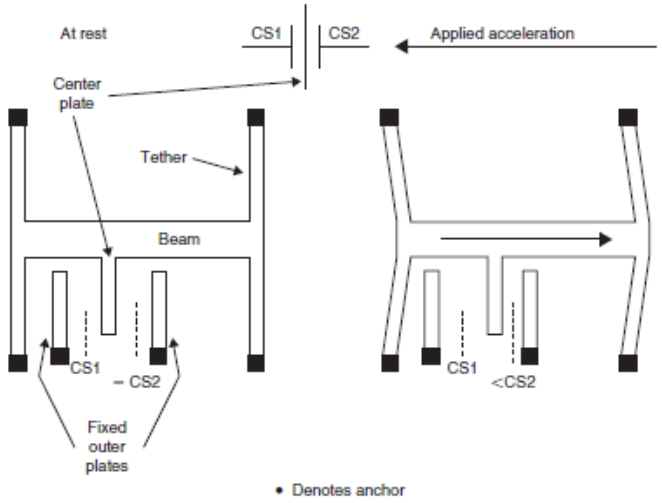

Figure 5 Applied acceleration changes capacitance between fingers [16]

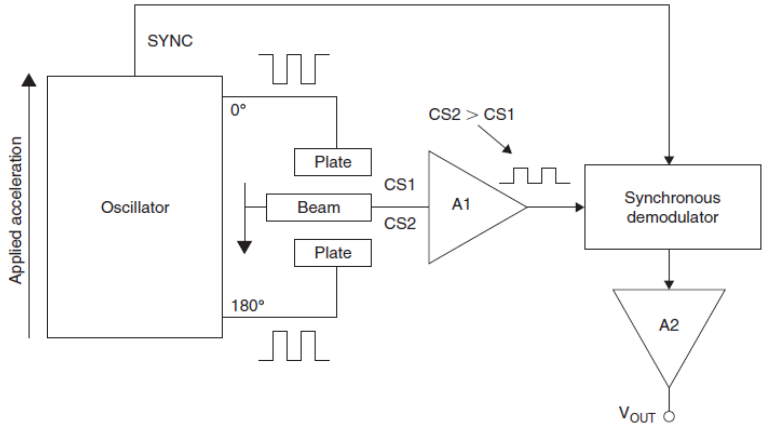

Figure 6 Working principle of a capacitive accelerometer [16]

A block diagram of a capacitive accelerometer is given in Figure 6. Capacitive sensors are commonly used in navigation applications. Quartz accelerometers and MEMS accelerometers are important members of capacitive accelerometers [14].

Piezoelectric accelerometers converts applied acceleration to electrical signal as indicated in Figure 7. Proof mass changes its position relative to the applied acceleration; therefore, piezoelectric material generates voltage related to acceleration [17]. These accelerometers are generally used for vibration measurements.

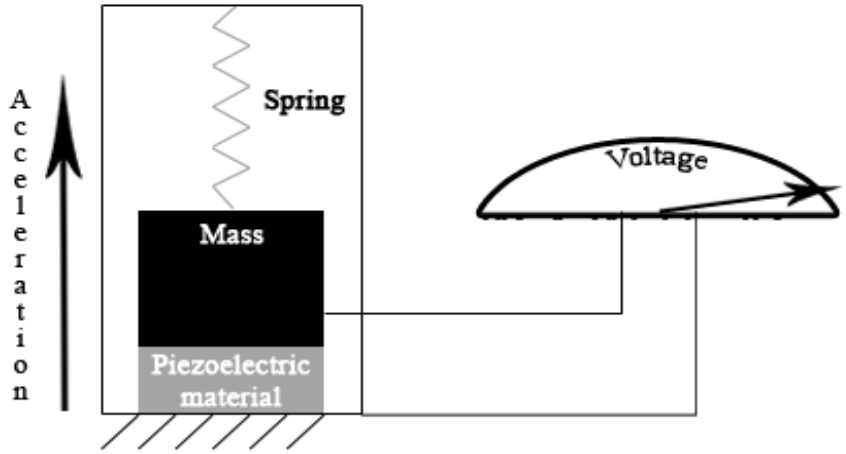

Figure 7 Applied acceleration trigs voltage generation for piezoelectric material [18].

A piezoresistive accelerometer is composed of six different parts [19]. Seismic or proof mass is fixed to a rigid frame with acceleration stress sensing piezoresistive sensor being connected to a Wheatstone bridge as illustrated in Figure 8. Acceleration changes the location of the proof mass; thus, resistances of Wheatstone bridge also change. As a result, a voltage that is related to the applied acceleration is produced at the Wheatstone bridge. Temperature dependency and offsets on Wheatstone bridge are disadvantage of these sensors [19]. Piezoresistive sensors are commonly evaluated for shock and vibration measurements. Table 1 presents advantages and disadvantages of different accelerometer technologies.

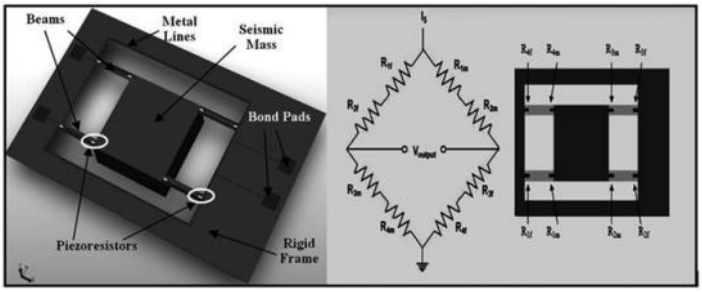

Figure 8 Elements of piezoresistive accelerometer is shown in left side of figure [19]. Wheatstone bridge (right side) provides voltage relevant to applied acceleration

Table 1 Comparison of different accelerometer types

Type of sensor	Advantages	Disadvantages
Capacitive	• Measures constant (e.g., gravitational) acceleration • High accuracy and reliability • Low costs	• Low bandwidth (nearly 5000 Hz) • Fragile
Piezoresistive	• Measures constant (e.g., gravitational) acceleration • High acceleration range	• Long term stability • Low temperature performance
Piezoelectric	• Large bandwidth • High acceleration range	• Constant acceleration cannot be measured • Poor stability and temperature performance

2.2 Gyroscopes

Gyroscopes detect angular velocity of a moving platform. Attitude parameters (i.e., roll, pitch and yaw) are calculated with respect to the gyroscope measurements. Therefore, if one wants to obtain full navigation parameters, accurate gyroscope

measurements are needed. Four main categories are available in gyroscope technology. These are optical, mechanical, quartz and MEMS gyroscopes [14].

The evaluation of both gyroscope and accelerometer technologies are illustrated in Figure 9. This figure indicates that no further developments for mechanical gyros. Yet, fiber optic gyros (FOG), quartz and MEMS gyros are still being developed.

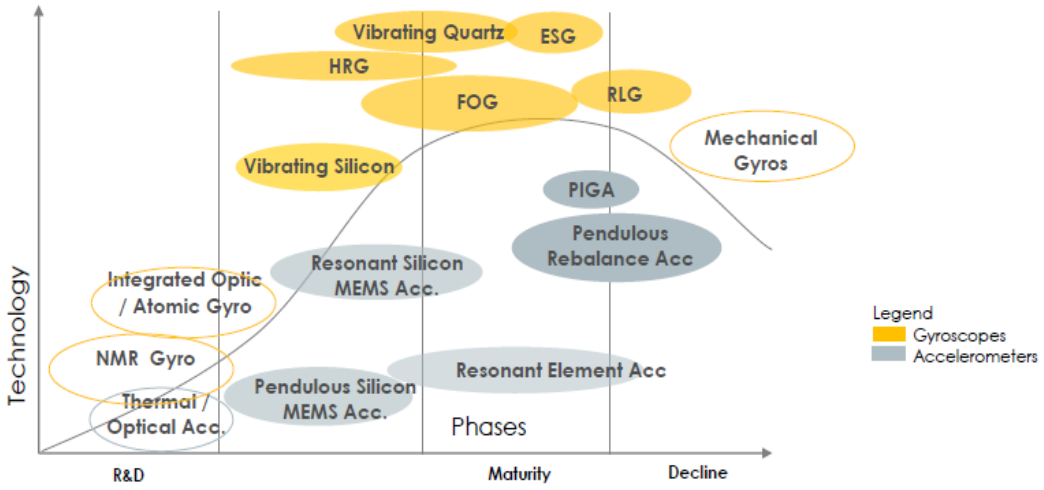

Figure 9 Development of accelerometer and gyroscope technology [14].

Mechanical gyros (i.e. MEMS gyroscopes) use Coriolis force to measure angular rate. These gyroscopes are stimulated by vibration and high rotation. As shown in Figure 10, linear motion is applied to gyroscope structure and if rotation occurs, Coriolis acceleration that is related to angular rotation can be sensed. Coriolis acceleration is perpendicular to both rotation axis and linear motion axis.

$$a_c = -2V \times \Omega \tag{2.2}$$

V, *linear velocity*
Ω, *rotation velocity*

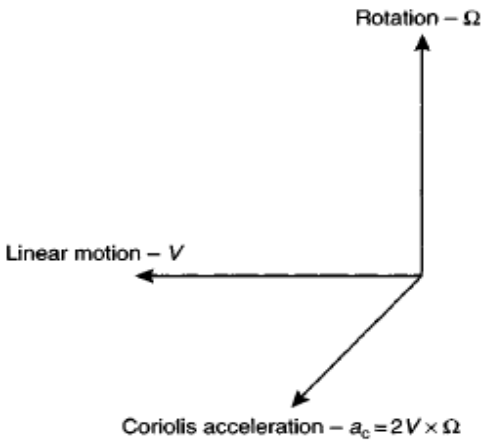

Figure 10 Coriolis acceleration is generated by linear motion and rotation [14].

MEMS gyroscopes can be categorized into 3 main groups: tuning fork, vibrating plate and resonant ring gyros. Tuning fork gyros basically have two plates that vibrate in different directions. Due to the Coriolis acceleration, tuning forks come closer or move away from the sensing elements when rotation occurs [14]. Capacitive sensing elements generate voltage proportional to applied rotation. A simple tuning fork structure is demonstrated in Figure 11 .

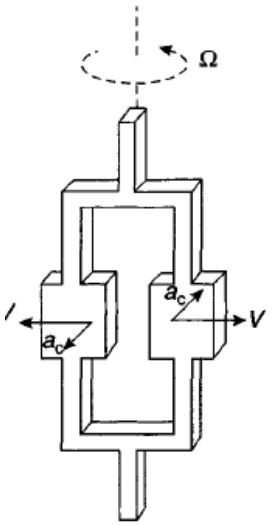

Figure 11 Working principle of tuning fork gyroscope [14]

Two silicon proof mass plates are hanged over a glass substrate by folded beams and they can vibrate in-plane 180 degrees out of phase as shown in Figure 12.

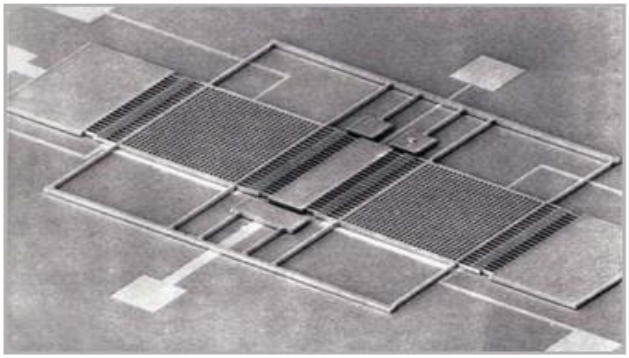

Figure 12 Vibrating plate MEMS gyroscope [14]

Vibrating piezoceramic cylinders are used to detect angular motion in resonant ring gyroscopes [14]. A metal disc or a disc resonator is used as the sensing element. Resonant ring gyroscope generates a resonance in the ring structure through a sequence of current flowing through the metal structure on the surface of the ring and a magnetic field vertical to the sensor [14]. When the sensor is rotated, energy is coupled from another mode (e.g., primary mode to secondary mode). This coupling generates a voltage which is related to angular motion.

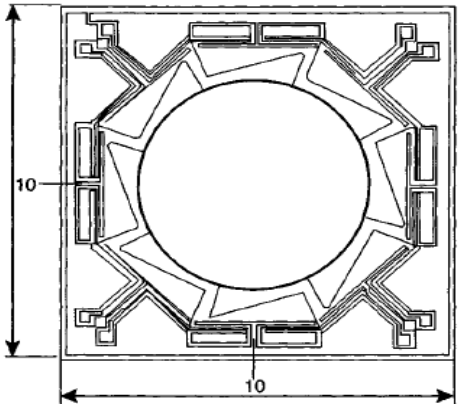

Figure 13 Structure of resonant ring gyroscope [14].

Optical gyroscopes use Sagnac effect to measure angular motion [2, 14]. Sagnac effect can be described as follows: if rotation occurs in a direction of light, total path of laser beam increases, rotation in the opposite direction leads to a reduction of the total path [2] as shown in the Figure 14.

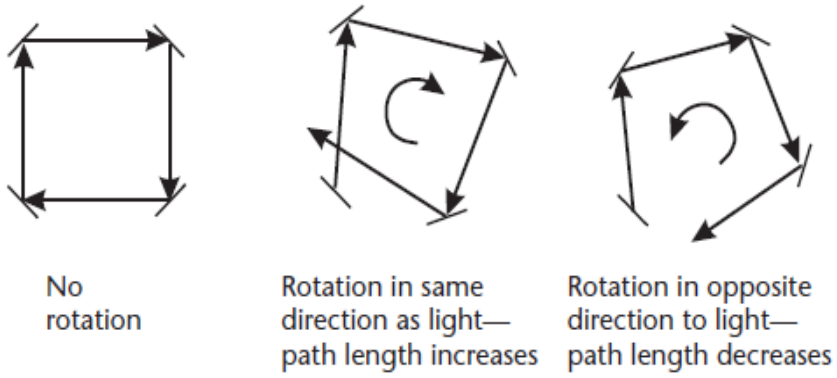

Figure 14 Illustration of Sagnac effect for a rotating system [2].

Three or more mirrors can be used in a triangular shaped laser path. Each light beam is generated at any point on path; light beam rotates around the path and it is reflected by all of the mirrors and turns back again its initial point [14]. Optical oscillations are produces when the transmitted laser beam is in phase with the received laser beam. Two laser beams track two different directions (e.g., clockwise and counter clockwise directions) in an RLG. These two laser beams have same frequency when sensor is in stable position [14]. If sensor is rotated along one direction, laser beams have different path length due to the Sagnac effect. This difference has effect on frequency of laser beams and it can be converted to rotation information [14]. Yet, because of the backscatter from mirrors, lock-in phenomena occurs when very low input rates are applied to RLG. An artificial bias that is called dither is used to remove lock-in problem. A simple RLG is illustrated in Figure 15.

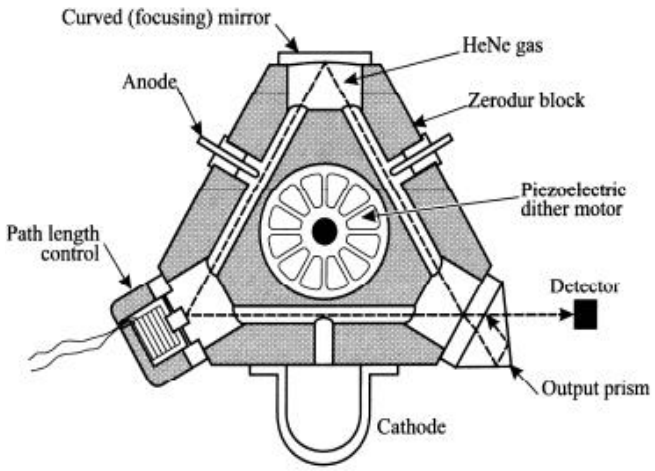

Figure 15 Components of an RLG [14].

Measurements of the fiber optic gyroscope are also based on the Sagnac effect. Light from a broadband source is divided into two beams and rotate in different directions in the fiber optic coil. Second beam splitter mixes two beams to produce an interference pattern. Photo-detector senses resulting intensity of the interference pattern. In the stationary position, two light beams are in phase and interference pattern is in the maximum amplitude. One light beam travels larger than other light beam when the sensor is rotated around an axis, which is perpendicular to the sensor plane [2, 14]. The change in path length of one light causes phase difference that is directly observed as a change in the amplitude of interference pattern. Advantages and disadvantages of different gyroscope technologies are summarized in Table 2.

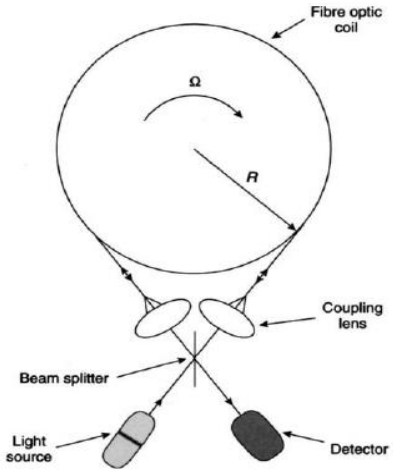

Figure 16 FOG sensors contain different parts: beam splitter, detector, light source, coupling lens and fiber optic coil [14].

Table 2 Comparison of different gyroscope technologies

Type of sensor	Advantages	Disadvantages
MEMS gyroscope	• Small size • Cheap • Suitable for aided navigation	• Limited performance range • Low bias repeatability performance
FOG	• Suitable for strapdown applications • Very rugged • Very small residual bias • No moving parts	• Complex electronic parts • Sensitive to changes in temperature
RLG	• Stable in different temperature • Simple electronics • Suitable for strapdown applications	• High voltage requirement • Expensive

CHAPTER 3

INERTIAL SENSOR ERRORS

Dead-reckoning is based on the knowledge of previous or initial velocity and position that can be added by the integration of recent acceleration and angular rate [14]. Inertial navigation systems perform dead-reckoning procedure. Velocity and position can be calculated by once and twice integration of accelerometer measurements, respectively. Body angles (i.e., roll, pitch and yaw) are formed by integration of gyroscope measurements. Due to the integration process, position and velocity errors increase with time [7].

Inertial sensor errors can be divided into two categories: deterministic and stochastic errors. Estimation and compensation of these errors is essential for navigation process [4, 14]. Magnitudes of sensor errors also determine the classification of an IMU such as navigation grade, tactical grade, control grade (automotive grade) [13].

Table 3 IMU classes according to random and deterministic errors.

Performance	**Navigation Grade**	**Tactical Grade**	**Control/Automotive Grade**
Gyroscope Bias (deg/h)	<0.01	1-10	>10
Accelerometer Bias (mg)	<0.1	1-10	>10
Gyroscope Random Walk (deg/√h)	0.05 to 0.005	0.5 to 0.05	>0.5

A sensor output can be described by,

$$o(t) = i(t) + D(T) + n(t) \tag{3.1}$$

$o(t) = output$
$i(t) = input$
$D(T) = Deterministic\,error$
$n(t) = noise\,term$
$t = time$
$T = temperature$

According to Equation (3.1), it is important that measurement accuracy depends on true determination of deterministic errors and noise term [20]. Deterministic errors are generally dependent on the temperature and they can be investigated by application of different temperatures [4, 5]. Stochastic errors terms (noise terms) change with time [7, 20]. Therefore, noise has to be modeled by stochastic models [21].

In this section, stochastic errors and their characteristics in different types of sensors are investigated. Deterministic errors are explained and discussed in details

3.1 Deterministic Errors

Deterministic errors are split into four categories such that bias, scale factor, misalignment and g-dependent bias [15]. Scale factor, bias and misalignment generally define the accelerometer deterministic errors while a gyroscope contains all of the error parameters in the measurements.

3.1.1 Bias

Ideally, when no input is applied to an inertial sensor, the output signal received from the sensor should be zero [1]. However, an offset occurs on the output signal.

Average value of a sensor output in stationary position over a predetermined time is called bias. Unit of the bias is mg or m/s^2 for accelerometer and deg/h for gyroscope.

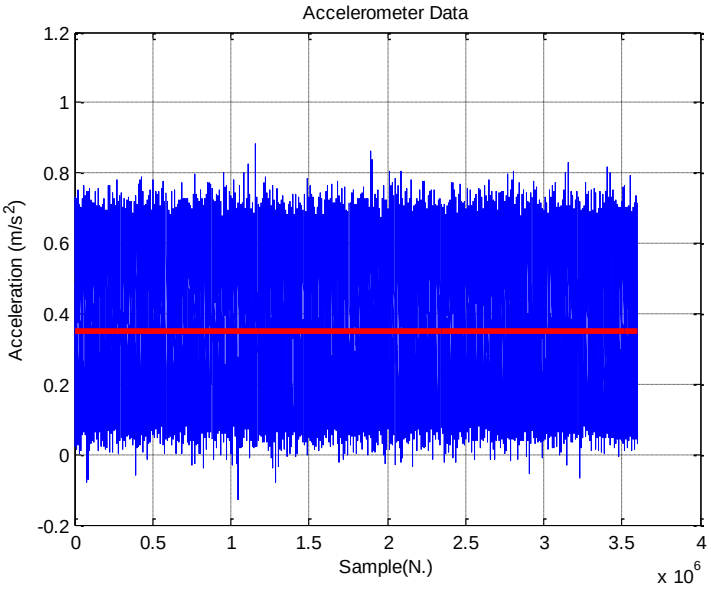

Figure 17 Bias offset is determined as a constant drift from true value. Red line shows bias offset at zero acceleration.

3.1.2 Scale Factor Error

Ratio between the output and the related input is defined as scale factor error. Expected value of the scale factor is 1, but, in general, this value is not observed in most cases. Unit of scale-factor error is percentage (%) or ppm (parts per million) [14]. Accelerometer scale factor error causes position error which is proportional to t^2 (square of time) [11].

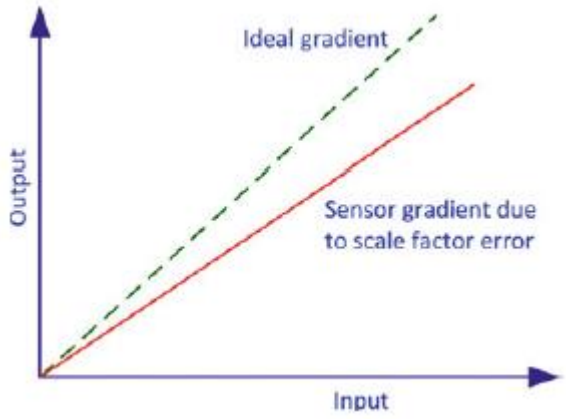

Figure 18 Scale factor error for an inertial sensor [13]

3.1.3 Misalignment Error

There are two types of the misalignment error. Firstly, there is the misalignment error which is non-orthogonality between the body axis of the vehicle and IMU [13]. Secondly, imperfect mounting of the inertial sensors to body of the inertial measurement unit is another source of misalignment error. This error source causes continuous drift of the sensor data. Unit of this error is mrad (mili-radian).

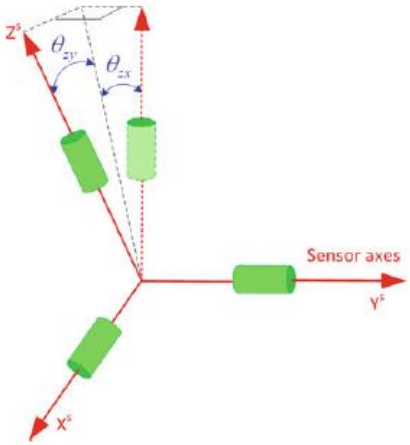

Figure 19 Non-orthogonality error between sensor axes [13]

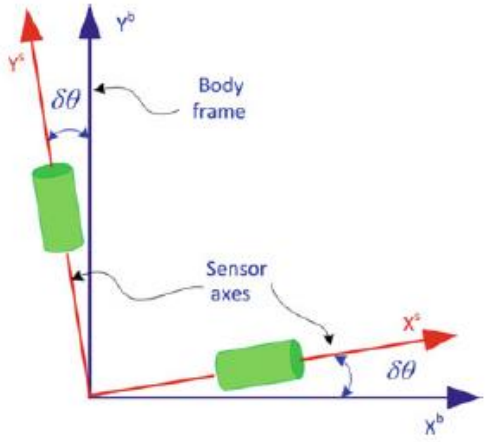

Figure 20 Angle between the body frame and the sensor frame determines the misalignment error [13]

3.1.4 G-Dependent Bias

MEMS gyroscopes have solid materials, proof mass and springs etc., to detect the rotation [15]. Acceleration causes additional motion on these components. This additional term is directly proportional to applied acceleration; hence it is determined by calibration tests. G-dependent bias is only observed in gyroscope measurements. Unit of this error term is deg/h/g.

3.2 Stochastic (Random) Errors

Inertial sensor data have random characteristics due to electrical circuits, interferences and temperature [8]. Random errors are categorized as Quantization Noise, Rate Random Walk, Bias Instability, Angle/Velocity Random Walk, Rate Ramp errors as shown in Equation (3.2).

$$n(t) = Q(t) + N(t) + B(t) + R(t) + P(t) + s(t) \tag{3.2}$$

$Q(t) = quantization\ noise$
$N(t) = angle\ /\ velocity\ random\ walk$
$B(t) = bias\ instability$
$R(t) = rate\ random\ walk$
$P(t) = rate\ ramp$
$s(t) = sinusoidal\ noise$
$n(t) = total\ noise\ term$

All of the random errors, which are given in the Equation (3.2), are dependent on time. In this section, random errors and their sources are explained.

3.2.1 Quantization Error

Generally, optical sensors measure angle increments through the fringes on the output of the sensor. Quantization error occurs when all fringes on the output of the optical sensor is not counted in a sampling time interval [22]. Remainder of the rotation is included in the next iteration. Hence, a non-integrating error occurs on the output of the sensor. Quantization error is observed in rate integrated sensors such as ring laser gyros (RLG). There is a confusion about bit quantization and time quantization in the literature [11]. Bit-quantization error is another type of error but it is not the stochastic type because maximum value of bit quantization error is somewhat deterministic (i.e., half of the least significant bit) [20]. If quantization noise is modeled as a bit-quantization noise, power of total error grows when number of samples increases [20]. On the other hand, time quantization error does not increase in time [20, 22]

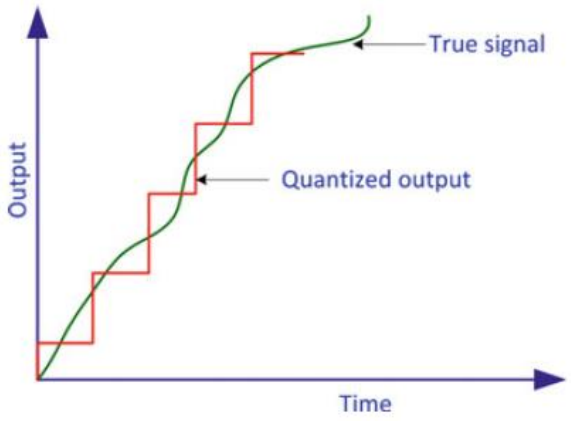

Figure 21 Bit-quantization error occurs during the conversion the true (analog output) signal to the quantized output [13]

3.2.2 Angle/Velocity Random Walk

Inertial sensor output is disturbed by thermo-mechanical noise and the correlation time of this disturbance is smaller than the sampling period of an inertial sensor [8]. Therefore, angle/velocity random walk has white noise characteristic hence, it is assumed to be in the uncorrelated noise type. Angle/velocity random walk is the dominant error source for all of sensor type [8, 20]. Angle random walk is referred to white noise of a gyroscope and velocity random walk is also referred to white noise of an accelerometer. This noise has a constant level in the frequency domain [23]. Thus, low pass filtering techniques can be applied to corrupted data to decrease this white noise like error source.

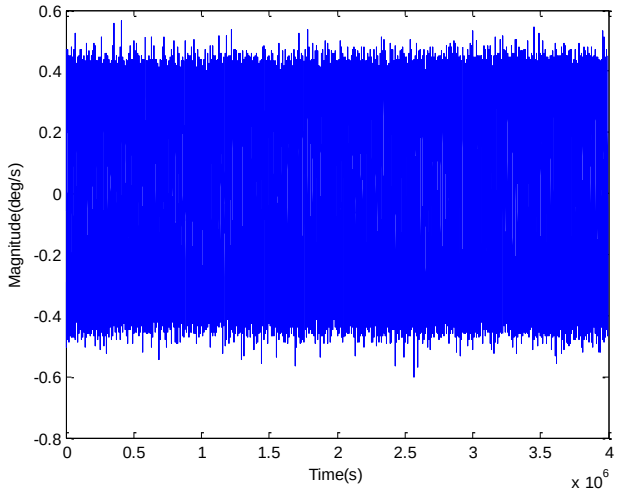

Figure 22 Effect of the angle/velocity random walk on an inertial sensor measurement.

3.2.3 Exponentially Correlated Noise

Exponentially correlated noise term is characterized by an exponentially decaying function with a finite correlation time [11]. PSD of this error term is [11],

$$S_{\Omega}(f) = \frac{(q_c T_c)^2}{1+(2\pi f T_c)^2} \tag{3.3}$$

Therefore,

$$\sigma^2(\tau) = \frac{(q_c T_c)^2}{\tau}\left[1-\frac{T_c}{2\tau}\left(3-4e^{-\frac{\tau}{T_c}}+e^{-\frac{2\tau}{T_c}}\right)\right] \tag{3.4}$$

$$q_c = noise\,amplitude$$

$$T_c = correlation\,time$$

If we assume that $q_c T_c = Q$ and $T \gg T_c$, we would obtain angle/velocity random walk [11].

$$\sigma^2(\tau) = \frac{(q_c T_c)^2}{\tau} \qquad \tau >> T_c \tag{3.5}$$

If we perform Taylor expansion for exponential terms in the Equation (3.4) we can obtain the following equation for $T \ll T_c$ which means that selected time values always smaller than correlation time. Hence, it represents low frequency correlated noise.

$$\sigma^2(\tau) = \frac{(q_c)^2}{3}\tau \qquad \tau << T_c \tag{3.6}$$

Plot of Equation (3.4) is shown in Figure 23. According to Figure 23,

- Curve approaches its maximum value at $T \cong 1.89T_c$
- Maximum value of curve is $\sigma_{max} \cong 0.437\ q_c\sqrt{T_c}$

These observations are used to model the flat region of Allan deviation curve.

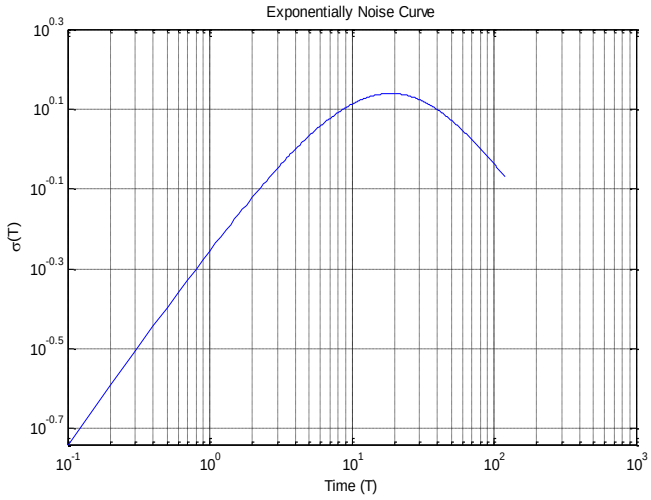

Figure 23 Exponentially correlated noise. This figure is drawn with the following parameters: $T_c = 10s$ and $q_c = 1$.

3.2.4 Bias Instability

Bias instability is named as “flicker noise” [20] , “low-frequency noise” which is used to describe the specific class of perturbations due to the oscillator. Flicks can be classified as noise on electronic equipment and/or environmental noises. Bias instability has low-frequency characteristic; therefore, it is assumed that bias drift on constant (residual) bias error. Sometimes, bias instability is called as 1/f noise because power spectral density (PSD) of bias instability is proportional to 1/f [24].

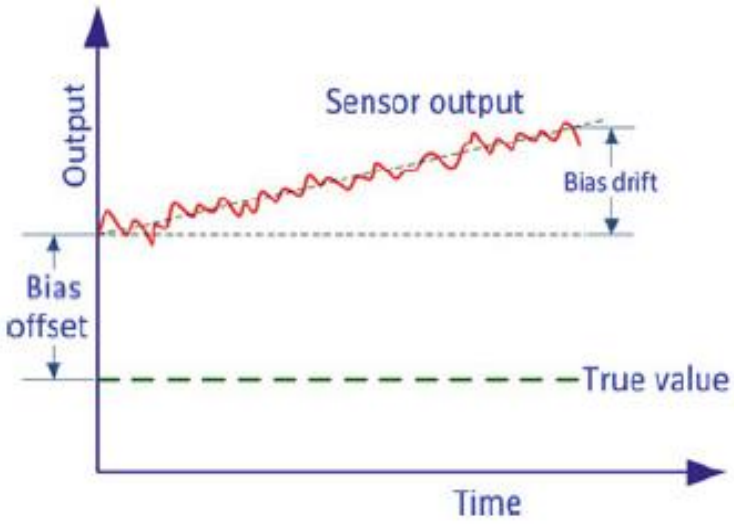

Figure 24 Effect of bias instability on the sensor output [13].

3.2.5 Rate Random Walk

Rate random walk occurs at larger cluster time [11]. As the name indicates, this error has random walk characteristic but identification of the rate random walk is very hard because of the temperature variations for long-time data acquisition [20]. Rate random walk is generally observed in tactical and control grade sensors.

3.2.6 Sinusoidal Noise

MEMS sensors are excited by sinusoidal vibrations to measure physical quantity. Sinusoidal input has effect on input axis of a sensor. Therefore, sinusoidal noise may be observed at the output of the sensor. Sinusoidal components are filtered out from data by low-pass filters. This is why several sensor producers use a filter in their sensor design [20]. If the frequency of sinusoidal noise is same with the motion frequency it is very hard to filter out sinusoidal component without manipulating the motion signal. Accuracy of inertial navigation system decreases due to this type of sinusoidal components.

General measurement models for accelerometer and gyroscope are given below. Acceleration error model can be modified as follows,

$$\hat{a}_x = (1 + S_{ax})a_x + M_{axy}a_y + M_{axz}a_z + B_{ax} + n_{ax} \tag{3.7}$$

$\hat{a}_x = acceleration\ output$

$B_{ax} = accelerometer\ bias\ term$

$M_{axy} = Misalignment\ between\ x\ and\ y\ axes$

$M_{axz} = Misalignment\ between\ x\ and\ z\ axes$

$a_x = real\ acceleretion\ term$

$n_{ax} = accelerometer\ noise\ term$

$S_{ax} = scale\text{-}\ factor\ error$

Gyroscope error model is given by,

$$\hat{w}_x = (1 + S_{gx})w_x + M_{gxy}w_y + M_{gxz}w_z + B_{gx} + G_{gx}a_x + n_{gx} \tag{3.8}$$

$\hat{w}_x = gyroscope\,output$

$B_{gx} = gyroscope\,bias\,term$

$M_{gxy} = Misalignment\,between\,x\,and\,y\,axes$

$M_{gxz} = Misalignment\,between\,x\,and\,z\,axes$

$a_x = real\,acceleretion\,term$

$G_{gx} = g - dependent\,bias$

$S_{gx} = scale - \ factor\,error$

$n_{gx} = gyroscope\,noise\,term$

CHAPTER 4

IDENTIFICATION OF THE STOCHASTIC ERRORS

Stochastic errors cause position and velocity errors in INS measurements. Since, they have to be estimated and modeled. Accurate modeling of an inertial sensor is the difficult problem because estimation techniques are based on error models. If a model parameter does not approach the real value, navigation algorithm cannot give accurate results. Estimation of stochastic error parameters is the other problem because several methods are available in the literature but many of them do not satisfy enough accuracy level.

Autocorrelation, PSD and Allan deviation methods are commonly used to estimate random error parameters. Allan deviation is standardizing method to estimate random errors therefore Allan deviation is selected as main reference in this chapter. Autocorrelation function is used to identify sinusoidal components on the output of a sensor. PSD is used to illustrate all error terms in an inertial sensor. Moreover, membership function based error identification technique will be discussed in this chapter.

4.1 Autocorrelation Method

Autocorrelation function describes the time constant of an inertial sensor. Time constant has special meaning because bias instability starts correlating the IMU data after time constant [7, 11]. Autocorrelation function is calculated according to Equation (4.1).

$$R_{xx} = E[x(t)x(t+\tau)] \tag{4.1}$$

$\tau = time\,lag$
$R_{xx}, = autocorrelation\ function$

Important properties of autocorrelation function can be expressed as [23],

- $|R_{xx}(\tau)| \leq R_x(0)\ where\ \tau > 0.$ The amplitude of the autocorrelation coefficient always smaller than $R_x(0)$.
- If $x(t)$ has some periodic parts, $R_{xx}(\tau)$ also has periodic parts with same frequency. However, phase information cannot be estimated from autocorrelation data if periodic data is sinusoidal.
- If $x(t)$ does not have any periodic or correlated parts, $R_{xx}(\tau)$ approaches zero when $\tau \to \infty$.

Second property is about behavior of an autocorrelation function when it contains periodic components. If an inertial sensor contains periodic parts such as a sinusoidal signal, we remember this property of an autocorrelation function. Third property is mainly about the correlated parts; autocorrelation function of an inertial sensor data approaches the zero value.

Bias instability is modeled as correlated noise because autocorrelation function of this process reaches zero when t goes to infinity [3]. Therefore, true determination of time constant is important for inertial sensor bias instability models. However, IMU output is generally corrupted by uncorrelated noise (e.g., white noise), which causes inaccurate identification of inertial sensors' time constant.

Before autocorrelation analysis, uncorrelated random errors are removed from inertial sensor data [7]. Some methods are suggested to filter IMU data and then obtain the correlated part of inertial sensor data, but these methods are not standard [12]. Furthermore, cut-off frequency of the filter is an important issue to get desired

correlated signal. Generally, cut-off frequency is selected very close to zero frequency due to the low-frequency characteristic of correlated signal [7]. Expected autocorrelation function after low-pass filter is given in Figure 25.

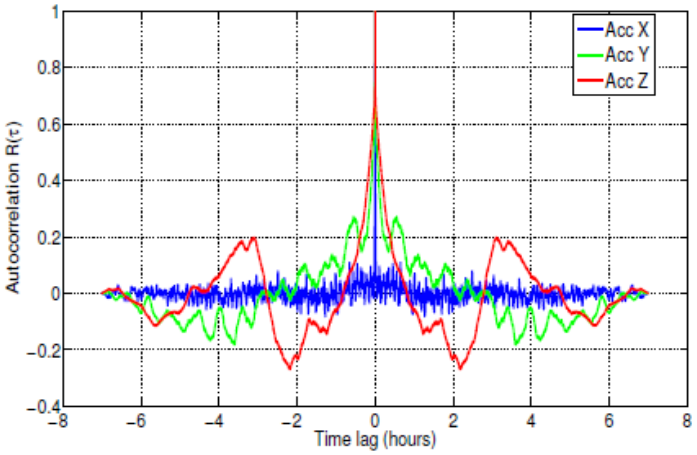

Figure 25 Simple autocorrelation function after low-pass filter [7]

If no filter is applied to data contaminated by white noise, autocorrelation function does not have any meaning because autocorrelation function reaches its minimum value too sharply due to the effect of uncorrelated parts. One example of this situation is shown in Figure 26.

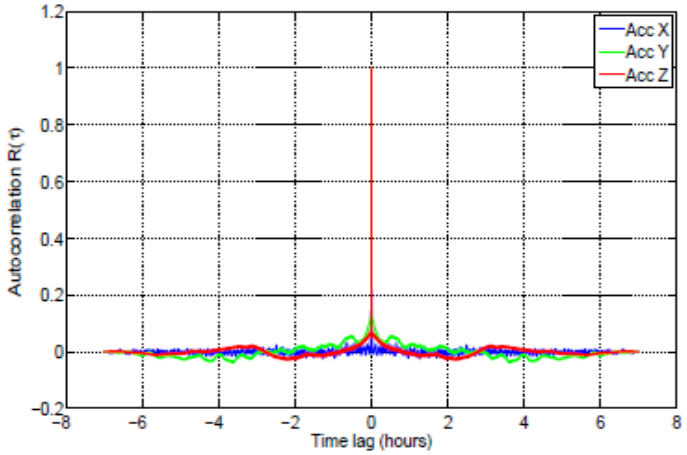

Figure 26 Autocorrelation function if low-pass filter is not applied [7]

The value of the time constant of an inertial sensor can be obtained from the %36.8 point of autocorrelation function of Gauss-Markov process.

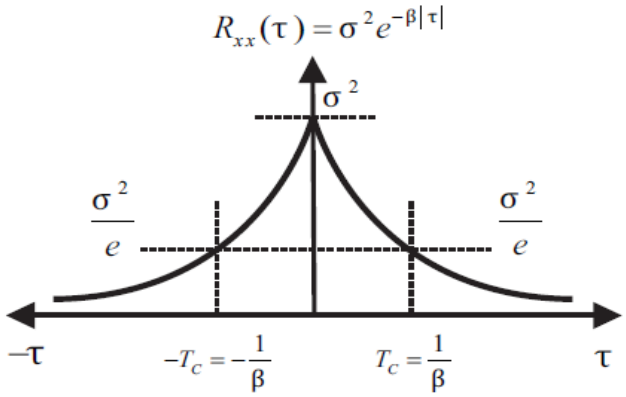

Figure 27 Autocorrelation function represents time constant value of an inertial sensor. Corresponding time value of 1/e point equals to time constant [7].

Figure 28 gives important real-data example of determination of time constant. In this configuration, Butterworth filter is selected as the low-pass filter [12] and f_c is set to four different cut-off frequencies. In this example, sampling frequency is set to 1000 Hz.

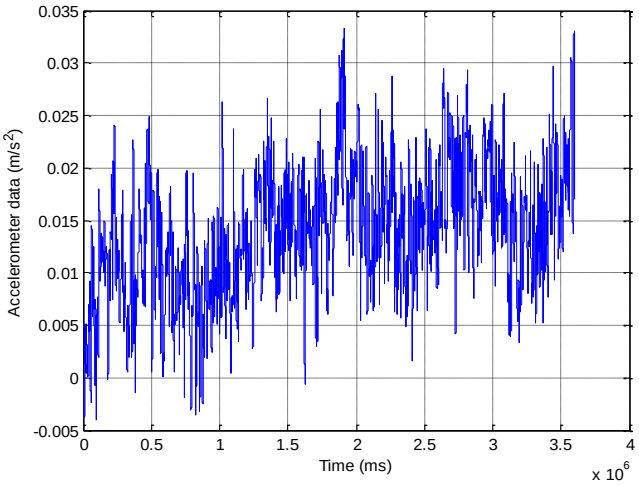

Figure 28 Accelerometer data after filtering. Bias instability can be observed from data.

Different cut-off frequencies yield different autocorrelation function as shown in Figure 29. Four cutoff frequencies (e.g., 0.003 Hz, 0.01 Hz, 0.03 Hz and 1 Hz) are tried. Identification of true cutoff frequency is empirical but autocorrelation gives an important approximation when comparison is made between same sensor types.

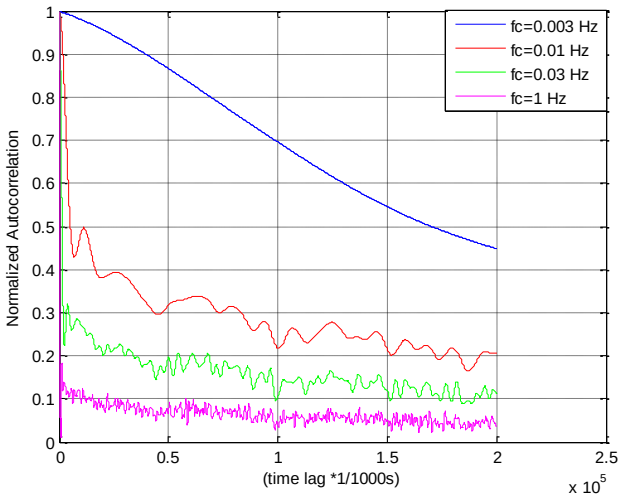

Figure 29 Normalized autocorrelation function of a gyroscope output that filtered with Butterworth filter at different cutoff frequency.

In this example, fc = 0.01 Hz is selected because it is smoother than other two types (e.g., fc = 0.03 Hz and fc = 1 Hz). Moreover, it is more realistic than the case with fc = 0.003 Hz example because fc = 0.003 Hz moves very slowly to zero value. Time constant value equals to 33.18 s (33180 (data number)*1/10^3 (sampling period) = 33.18s).

Accuracy level of autocorrelation function is determined by the following equations [23].

$$Var\,V_x(\tau) \le \frac{4}{T}\int_0^{\infty} R_x^2(\tau)d\tau$$

$$T = measurement\ interval \tag{4.2}$$

$$R_x(\tau) = autocorrelation\ function\ of\ the\ Gaussian\ process$$

$$V_x(\tau) = \exp erimentally\ \det er\ \min ed\ autocorrelation\ function$$

$$V_x(\tau) = \frac{1}{T-\tau}\int_0^{T-\tau} X_T(t)X_T(t+\tau)dt \tag{4.3}$$

$$R_x(\tau) = \sigma^2 e^{-\beta|\tau|} \tag{4.4}$$

$$\beta = reciprocal\ value\ of\ time\ constant$$

$$Var[V_x(\tau)] \le \frac{2\sigma^4}{\beta T} \tag{4.5}$$

$$\sqrt{\frac{Var[V_x(\tau)]}{\sigma^4}} \le \sqrt{\frac{2}{\beta T}} \tag{4.6}$$

$$\sqrt{\frac{Var[V_x(\tau)]}{\sigma^4}} = deviation\ from\ actual\ autocorrelation\ function$$

Accuracy of an experimentally determined autocorrelation function is defined by Equation (4.6). Accuracy of data, which is shown in Figure 30, is calculated as follows:

$$\beta = 33.18\,s$$

$$T = 3600s\,(1hour)$$

$$accuracy \le \sqrt{\frac{2x33.18}{3600}}x100$$

$$accuracy \cong \%13$$

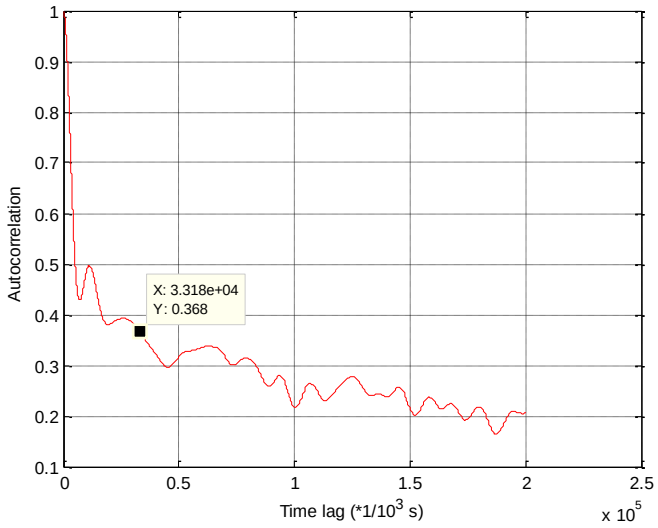

Figure 30 Identification of time constant with autocorrelation method. Time lags of 0.368 (1/e value) point equals to 33.18 s.

Besides the correlation time estimation, autocorrelation function can be used to investigate sinusoidal noise in the output of an inertial sensor [20]. Figure 31 and Figure 32 show autocorrelation functions of two different accelerometers. While former suffers from sinusoidal noise and the latter does not have this noise but it is still effected by other noise terms. Before applying autocorrelation function to data, these two data is filtered with a high-pass filter (Butterworth, f_c = 1 Hz). It is assumed that high-pass filter reduces the effect of correlated part. So that there is no correlated part on the output of the sensor and we only observe uncorrelated parts and sinusoidal parts.

Autocorrelation analysis is an accurate method to test whether a signal contains periodic parts or not. Thus, autocorrelation function is examined if sinusoidal parts are expected.

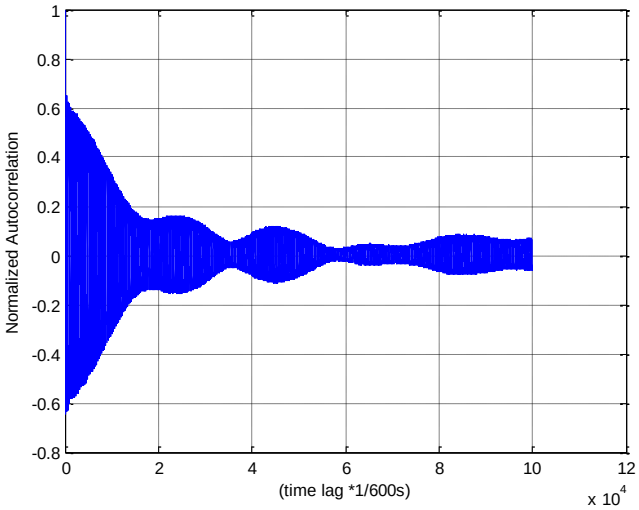

Figure 31 Sinusoidal parts can be observed in the autocorrelation function

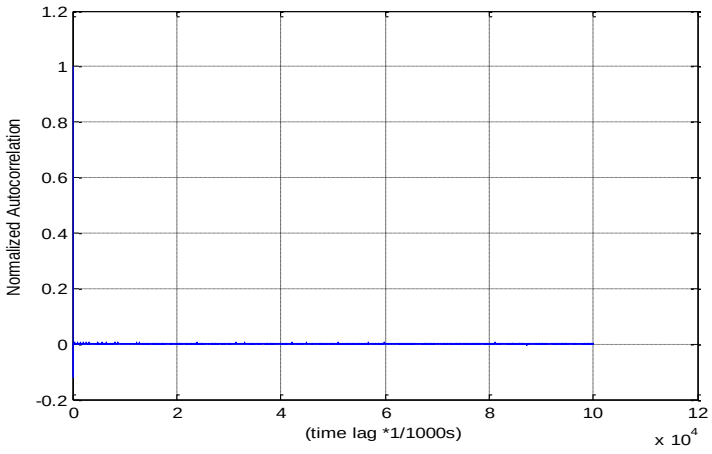

Figure 32 Autocorrelation function reaches zero value in small time lags due to the uncorrelated parts.

4.2 Power Spectral Density function

Power spectral density (PSD) is another descriptor of inertial sensor noise terms. Uncorrelated parts have high frequency components, while correlated parts have low

frequency components. PSD contains information about the frequency components of the time series and "power" indicates the amount of noise in the data [25].

If the random process $x(t)$ is stationary, it is not absolutely integrable; therefore, Fourier transform of this signal does not converge. In order to assure absolutely integrability of Fourier transform of a random process, data is truncated to a finite time interval such that [0, T] and this data can be indicated as $x_T(t)$ [23].

Relationship between autocorrelation and PSD is given in Equation (4.7).

$$S_x(jw) = F[R_x(\tau)] = \int_{-\infty}^{\infty} R_x(\tau) e^{-jw\tau} d\tau$$
$$S_x, \textit{power spectral density}$$
$$R_x(\tau), \textit{autocorrelation function of the data} \qquad (4.7)$$
$$F[*], \textit{Fourier transform of a given function}$$

In another approach, we take the expectation value of the periodogram, expressed in Equation (4.8) for large time interval (T).

$$S_x(jw) = E\left[\frac{1}{T} | F\{x_T(t)\} |^2\right]$$
$$S_x, \textit{power spectral density} \qquad (4.8)$$
$$F[*], \textit{Fourier transform of a given function}$$

One sided power spectral density is shown in Equation (4.9) but we usually use discrete signals; therefore an approximation is indicated in Equation (4.10) has to be used. This equation converts Fourier transform of discrete signal to Fourier transform of continuous signal at discrete frequencies.

$$S^1(f) = \frac{1}{T} |X(f)|^2 \qquad (4.9)$$

$$S, one-sided\ power\ spectral\ density$$

$$X(f), Fourier\ transform\ of\ a\ continuous\ signal$$

$$X(f_j) \cong X_j\, \delta t\ where\ j = 1,2,3,\ldots,\left[\frac{N}{2} - 1\right] \qquad (4.10)$$

$$\delta t = sampling\ interval$$

$$X_j = Discrete\ Fourier\ Transform\ of\ the\ signal$$

Substituting Equation (4.10) into Equation (4.9) gives discrete one-side equivalent of the PSD function. Equation (4.11) shows the resulting equation for power spectral density function of discrete data.

$$S^1(f_j) = \frac{\delta t^2}{T} |X_j|^2 \ \ if\ N\ is\ odd$$

$$S^1(f_j) = \frac{\delta t^2}{2T} |X_j|^2\ if\ N\ is\ even \qquad (4.11)$$

Each random noise term has a different PSD equation, hence, loglog plot of an inertial sensor gives different slopes and these slopes indicate that different error terms are available in data. A simple PSD with different error characters is given in Figure 33 .

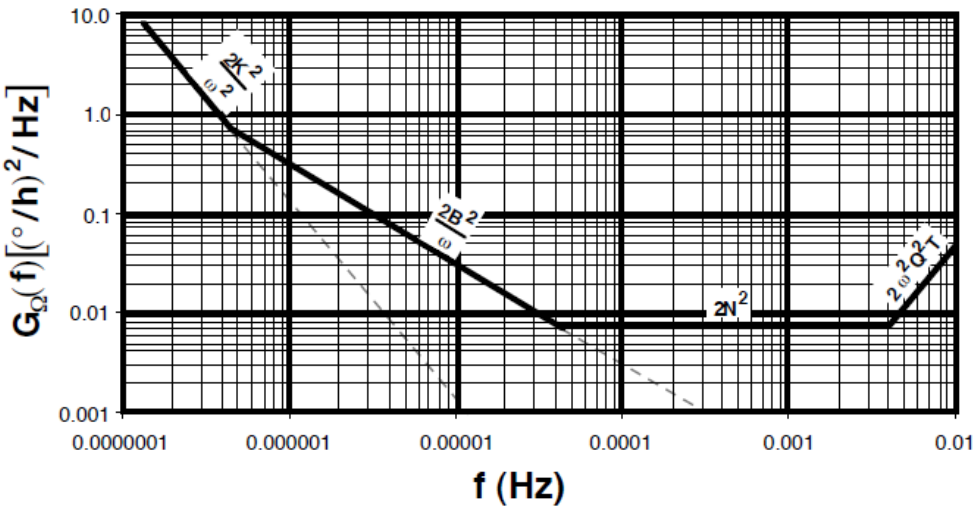

Figure 33 PSD gives information about different error terms [21].

According to Figure 33, rate random walk, bias instability, angle/velocity random walk and quantization noise can be found in the regions of slope -2, -1, 0 and +2, respectively.

PSD plot of an accelerometer is illustrated in the Figure 34. Angle random walk is observed from data due to the flat region. However, PSD function spreads too much; because of that, frequency averaging has to be performed [11]. Frequency averaging technique reduces the frequency points and magnitude of error terms are identified easily [11].

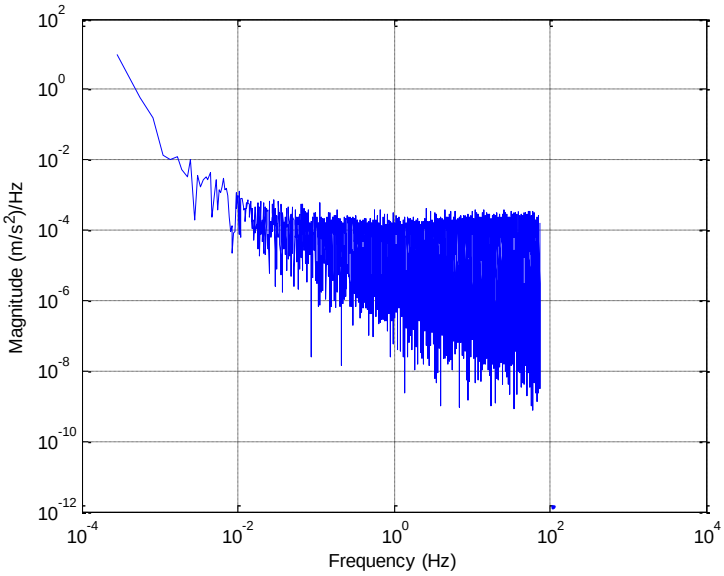

Figure 34 PSD function of an accelerometer data. Identification of noise is not easy because PSD spreads too much.

Frequency averaging can be performed in the logarithmic order at orders of 2. According to this method, first 32 frequency points are assigned to frequency averaged data and then continue with orders of 2^N, N=1,2,..n frequency points and calculate the mean value of each group. This averaging technique is applied until the last frequency point. This technique prevents the bunching at high frequencies and slope of error parameters easily intersects with PSD estimate. An example of application of frequency averaging technique on PSD given in Figure 34 and resulting PSD graph is illustrated in Figure 35.

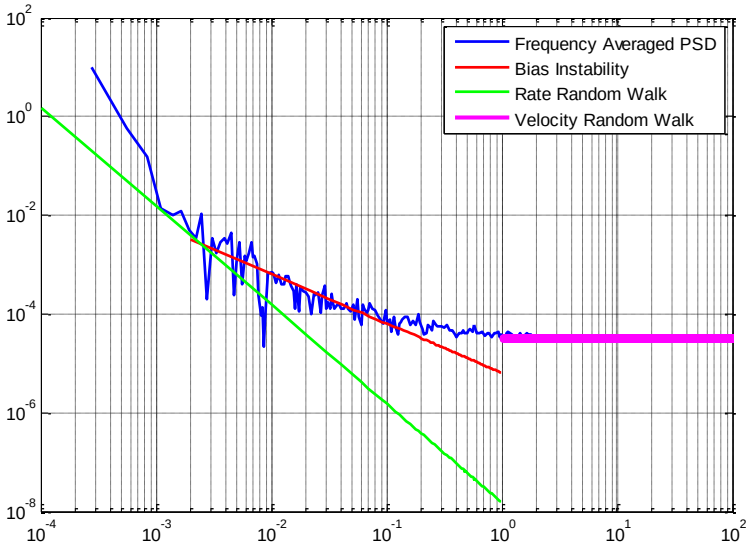

Figure 35 Different error parameters are identified after frequency averaging technique.

Identified error parameters are stated in Table 4.

Table 4 Error parameters with respect to the Figure 35.

Error parameter (Unit)	**Magnitude**
Rate random Walk ($m/s/h^{3/2}$)	97.2
Bias Instability (m/s^2)	0.0035
Velocity Random Walk($m/s/\sqrt{s}$)	0.0041

In some applications, cut-off frequency of an inertial sensor is not known. There are some useful methods are available in the literature to extract transfer function of an inertial sensor. Yet, PSD gives quick information about cutoff frequency of a sensor but details are not available in the PSD estimation. An example of above discussion is shown in Figure 36. In this example, the producer of this inertial sensor only declares that minimum bandwidth which is 75 Hz but exact bandwidth is larger than 75 Hz.

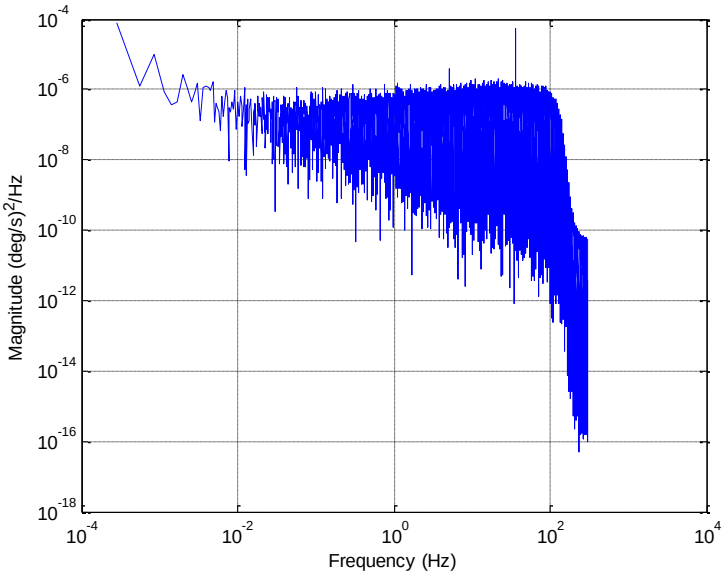

Figure 36 Cut-off frequency of the inertial sensor is nearly 100 Hz.

4.3 Allan Deviation Technique

Allan deviation method was first used for oscillator stability and this method extracted the instability errors of the oscillators [26]. Yet, these errors have many similarities with inertial sensor random errors. Furthermore, some studies introduce that how this method can be used for identification of random errors of inertial sensors [27]. Allan variance method is accepted by IEEE as a standard method for identification of stochastic errors for inertial sensors [21].

Allan deviation method considers on time-domain analysis of a data and it gives error parameters of noises that corrupt the inertial sensor data. This method assumes a noise is produced by specific character [11]. This method estimates the standard deviation of a noise character from collected data. Allan variance curve represents an identification of the underlying processes in the time-dependent stochastic error term n(t).

4.3.1 Calculation of Allan Deviation

Allan deviation method splits a signal into different clusters. Number of data in each cluster is different. For example, time difference between two consecutive samples is 1 second (τ_1) in cluster 1 but this difference can be 2 seconds (τ_2) for cluster 2. If total number of the collected data is N, the last cluster may be divided into two consecutive parts. Therefore, $\frac{N}{2}$ data defines the last time index (τ_n) value ($\frac{N}{2}$ *Δt). τ_n determines the maximum cluster time which can be presented by an Allan variance curve. It means that Allan deviation method needs more data points than other methods to extract true noise characteristic. Generally, it is necessary to collect data over an hour.

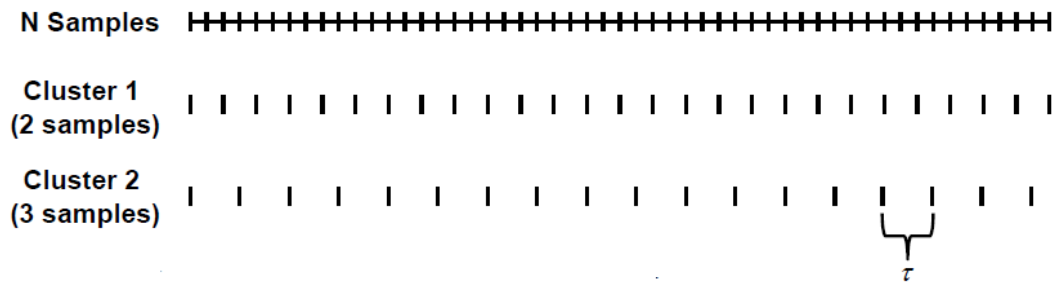

Figure 37 Clusters in Allan deviation method. Each cluster has different time (tau) information.

Allan deviation curve is obtained by following steps:

- Determine the τ (cluster time) values.
- Separate the data with one of the pre-determined τ_k values and take the average value of each division. Assign these mean values to $y(i)$ variable where $i \geq 0$ and i is an integer value.

- Note that the term $y(i)$ includes the mean value of data between $i * \tau$ and $(i + 1) * \tau$.
- Calculate $\sigma(\tau)$ from the following equation:

$$\sigma(\tau) = \left[\frac{1}{2M} \sum_{i=0}^{M-1} (y(i+1) - y(i))^2 \right]^{1/2}$$
$$M = [\frac{T}{\tau_k} - 1] \quad (4.12)$$
$$T = measurement\ interval$$

- Draw loglog plot of the sigma ($\sigma(\tau)$) values with corresponding tau values (τ_k).
- Obtain the sigma values (standard deviation) of each error term. For example, if the unit of the raw measurements deg/s, then, unit of sigma values is also deg/s.

According to [21], relationship with PSD and Allan Variance is given in Equation (4.13). Therefore, we can extract special characteristic of each noise term with given PSD function.

$$\sigma^2(\tau) = 4 \int_0^\infty S_\Omega(f) . \frac{sin^4(\pi f \tau)}{(\pi f \tau)^2} df \quad (4.13)$$
$$S_\Omega(f) = PSD\ of\ a\ random\ process$$

Allan deviation is related to the noise power after PSD of the random process is passed through a filter with transfer function $\frac{sin^4(\pi f \tau)}{(\pi f \tau)^2}$ [7, 11] . Response of the filter depends on varying τ; therefore, several types of noise characters can be inspected by the Allan deviation method [7].

Error level of the Allan deviation method can be calculated by Equation (4.14) [11]. In this thesis, at least 88 % accuracy level is satisfied to identify random error coefficients.

$$\%Error\ level\ in\ AD\ Method = \frac{1}{\sqrt{2(\frac{M}{n})-1}}\ x100$$

$$M = total\ data\ points \tag{4.14}$$

$$n = total\ data\ points\ used\ to\ identify\ error\ coefficient$$

Allan deviation technique is a powerful technique to identify five major stochastic error terms as shown in Figure 38.

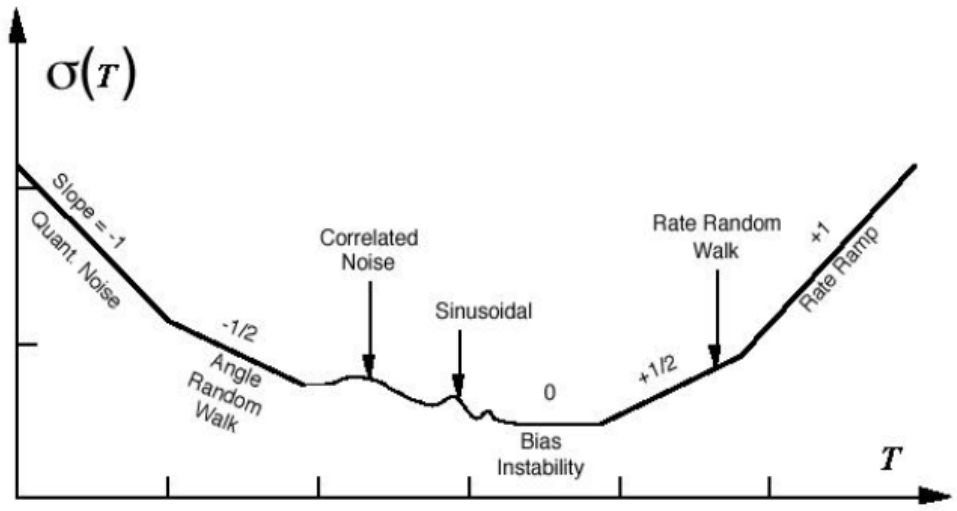

Figure 38 A simple Allan deviation curve [11]

4.3.1.1 Quantization Noise Parameter

PSD of the quantization noise is shown in Equation (4.15). This PSD function can be used in Allan variance expression given in Equation (4.13) [21].

$$S_{\Omega}(f) = \frac{4Q_z^{\,2}}{T_s}\sin^2(\pi f T_s) \approx (2\pi f)^2 T_s Q_z^{\,2} \; where \; f < \frac{1}{2T_s}$$
$$Q_z = quantization\, noise\, parameter \qquad (4.15)$$
$$T_s = sampling\; period$$

Resulting Allan deviation sigma value is expressed in Equation (4.16) [11].

$$\sigma(T) = Q_z \frac{\sqrt{3}}{T} \qquad (4.16)$$

Therefore, slope of quantization noise is -1 in a logarithmic plot. Quantization noise parameter is obtained by intersection line which slope is -1 with the Allan deviation curve.

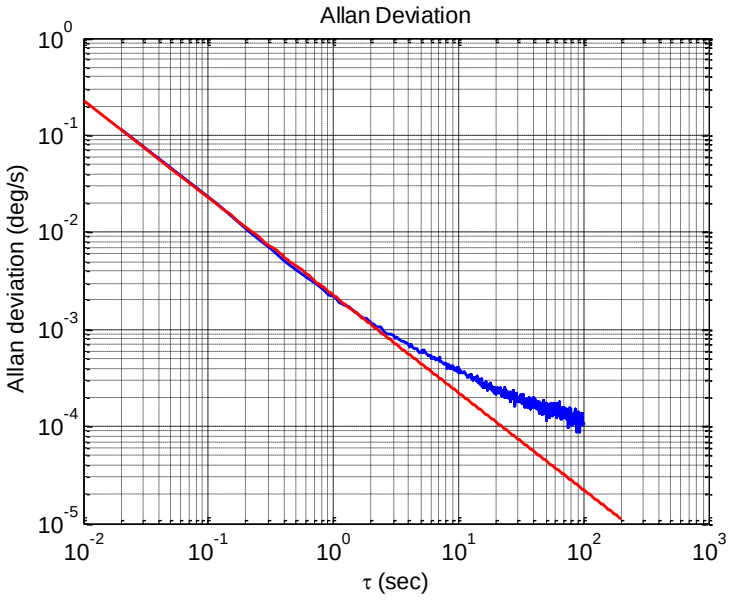

Figure 39 Allan deviation curve of an RLG. Red line indicates that slope equals to -1.

4.3.1.2 Angle/Velocity Random Walk Coefficient

As indicated in Section 3.2.2, angle/velocity random walk has constant level in frequency domain. Hence, its PSD function is the square of a constant, N^2

$$S_{\Omega}(f) = N^2 \tag{4.17}$$

Assume that, $k = \pi f \tau$ and substitude PSD function into the Equation (4.13) [11].

$$\sigma^2(\tau) = \frac{4}{\pi\tau}\int_0^{\infty} N^2 . \frac{sin^4(k)}{(k)^2} dk \tag{4.18}$$

$$\sigma^2(\tau) = \frac{4}{\pi\tau} N^2 \int_0^{\infty} \frac{sin^4(k)}{(k)^2} dk \tag{4.19}$$

$$\int_0^{\infty} \frac{sin^4(k)}{(k)^2} dk = \frac{\pi}{4} \tag{4.20}$$

$$\sigma(\tau) = \frac{N}{\sqrt{\tau}} \tag{4.21}$$

Equation (4.21) shows sigma value of angle/velocity random walk. Slope of logarithmic plot of the Equation (4.21) equals to -1/2 due to the square root in denominator. Angle/ velocity random walk can be estimated directly from the τ=1s or the actual value of angle/velocity random walk can be identified with the intersection of a line (slope equals to -1/2) with the τ = 1s. Sometimes, there is small difference between former and latter methods. Unit of angle/velocity random walk is $\deg/\sqrt{h}$ for gyroscopes and $\frac{m}{s\sqrt{s}}$ or $\frac{g}{\sqrt{Hz}}$ for accelerometers. Suppose that, corresponding value of τ = 1s is $9x10^{-3}$ deg/s. According to Equation (4.21), supposed that, $\sigma(\tau = 1s)$ equivalence of Allan deviation curve is given as $9x10^{-3}$ deg/s and parameter N is identified by the following conversion.

$$9x10^{-3}\frac{\deg}{s}=\frac{N}{\sqrt{\tau}}\rightarrow 9x10^{-3}\frac{\deg}{s}=\frac{N}{\sqrt{1s}}\rightarrow N=9x10^{-3}\frac{\deg}{\sqrt{s}}\ where\ \tau=1s$$

$$1hour=3600s$$

$$N=9x10^{-3}\frac{\deg}{\sqrt{h/3600}}\rightarrow N=54x10^{-2}\frac{\deg}{\sqrt{h}}$$

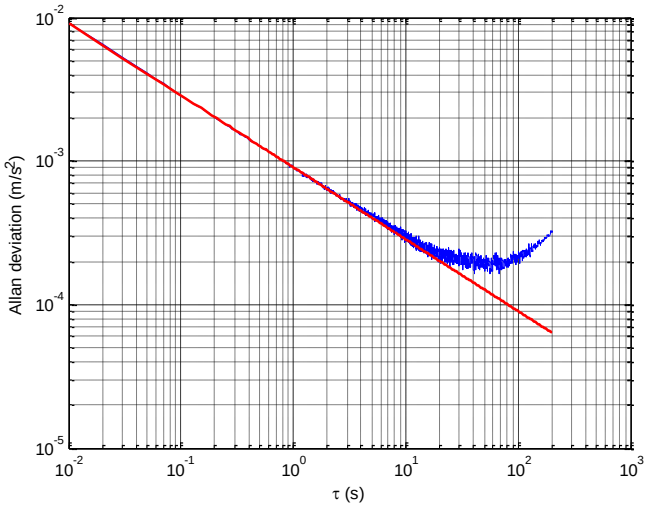

Figure 40 Allan deviation curve of a MEMS accelerometer. Velocity random walk coefficient is estimated from τ=1s.

4.3.1.3 Bias Instability Coefficient

Bias instability affects the output of an inertial sensor after some time constant as stated before. Therefore, determination of both correlation time and noise coefficient is important for navigation algorithms. These two parameters can be estimated by the Allan deviation curve. Bias instability is a low-frequency noise term; thus, its PSD is zero in high frequency and it cannot be estimated in small τ values in the Allan deviation curve. PSD of bias instability is given by [11],

$$S_{\Omega}(f)=\begin{cases}\dfrac{B^2}{2\pi f}, f \le f_c \\ 0, f > f_c\end{cases} \tag{4.22}$$

$$f_c = cut-off\ frequency$$

f_c indicates that bias instability starts to vanish in an inertial sensor output; therefore, it has a relationship with time constant (T_c) of an inertial sensor.

$$\sigma^2(\tau)=\frac{4}{\pi\tau}\int_0^{\infty}\frac{B^2}{2\pi f}.\frac{sin^4(\pi f\tau)}{(\pi f\tau)^2}df \tag{4.23}$$

$$\sigma^2(\tau)=\frac{2B^2}{\pi}\int_0^{\pi f_c\tau}\frac{sin^4(\pi f\tau)}{(\pi f\tau)^3}df \tag{4.24}$$

$$\sigma^2(\tau)=0\ for T \ll 1/\ f_c \tag{4.25}$$

$$\sigma^2(\tau)=\frac{2B^2}{\pi}ln2\ for T \gg 1/\ f_c \tag{4.26}$$

$$\sigma(\tau)=0.664B\ for T \gg 1/\ f_c \tag{4.27}$$

Equation (4.27) does not depend on time. Therefore, bias instability is obtained from flat region of an Allan deviation curve. Sigma value of the bias instability can be taken as the minimum value of the flat region. When slope of Allan deviation curve becomes zero, corresponding cluster time is the correlation time (time constant) of the bias instability [7]. Unit of this error is deg/h or m/s^2 for gyroscope and accelerometer, respectively. Unit conversion is given by,

$$0.002041\frac{m}{s^2}=0.664B \rightarrow B=\frac{0.002041}{0.664}\frac{m}{s^2}\rightarrow B=0.0031\frac{m}{s^2}$$

$$1g=9.80665\frac{m}{s^2}$$

$$B=0.3mg\ and\ T_c=20s$$

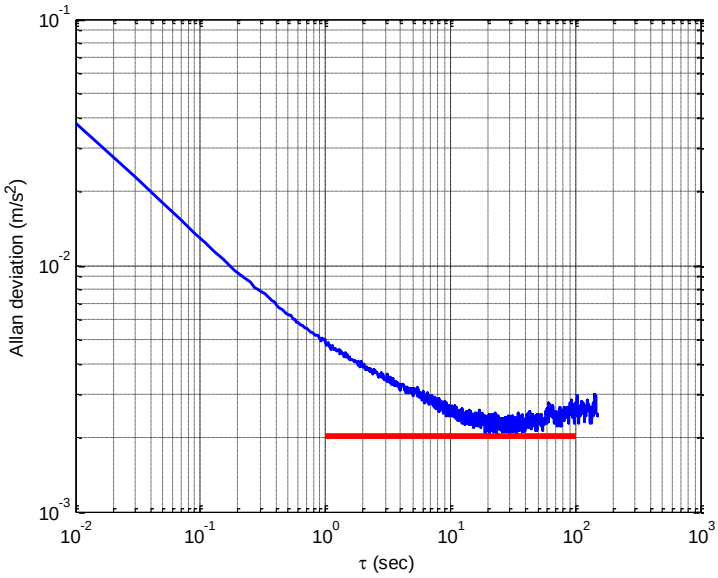

Figure 41 Red line indicates that slope equals to zero. Time constant is 20s and sigma value of bias instability is 0.002041 m/s^2

4.3.1.4 Rate Random Walk Coefficient

Rate random walk appears at higher cluster time than other errors and it can be observed at larger τ values than other noises. Therefore, if an inertial sensor works in short-time applications this error may not be modeled. Rate random walk is generally seen in MEMS accelerometer and quartz-MEMS gyroscope measurements. PSD density of the rate random walk is given in Equation (4.28). Resulting sigma value of the rate random walk in the Allan deviation curve is expressed in (4.29).

$$S_{\Omega}(f) = \frac{K^2}{(2\pi f)^2} \tag{4.28}$$

$$K = rate\, random\, walk\, parameter$$

$$\sigma(\tau) = K\sqrt{\frac{\tau}{3}} \tag{4.29}$$

Slope of the rate random walk is 1/2 and K is estimated by the intersection of rate random walk line with the Allan deviation curve using Equation (4.29) as shown in Figure 42.

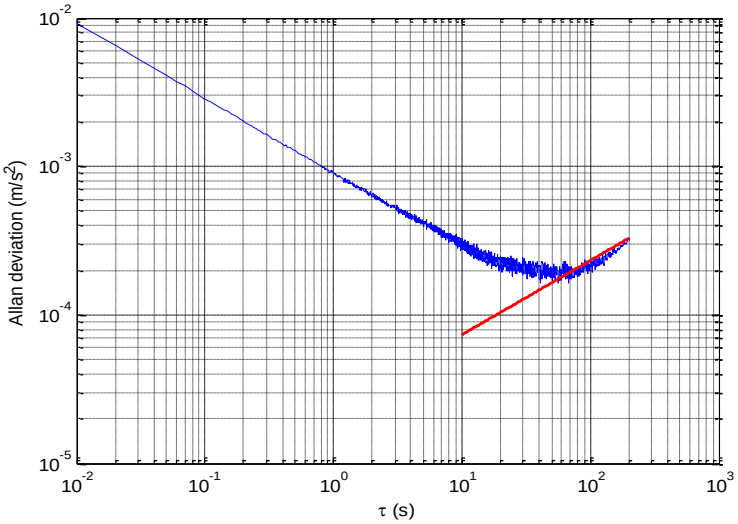

Figure 42 Rate random walk line which is indicated as red line. This line intersects with Allan deviation curve to define rate random walk coefficient. Slope of red line is +1/2.

Related sigma value of the rate random walk coefficient is 0.0004 m/s^2. Conversion from sigma value to rate random walk coefficient value is given by,

$$0.0004\frac{m}{s^2} = K\sqrt{\frac{\tau}{3}} \; where \; 10s \le \tau \le 200s \; (red\ line\ in\ the\ figure\ lie\ in\ that\ range)$$

$$0.0004\frac{m}{s^2\sqrt{s}} \rightarrow \frac{m}{s^{5/2}} \rightarrow \frac{1h}{3600} = 1s \rightarrow m/s/h^{3/2} * (3600)^{3/2}$$

$$K = 84.67\, m/s/h^{3/2}$$

4.3.1.5 Sinusoidal Noise

Sinusoidal noise cannot be determined from Allan deviation curve because white noise characters conceal sinusoidal noise. There are some indicators about sinusoidal

noise in an Allan deviation curve [20]. Firstly, if some bulges are observed they can be sign of sinusoidal noise. Secondly, sinusoidal noise is directly detected from an Allan deviation curve in some examples [11]. Allan deviation curve of an RLG usually has sinusoidal noise due to dithering. Some imperfections in a power supply or vibrations in MEMS sensors also cause sinusoidal noise. Expression of sinusoidal noise, which has a particular frequency component, is given in Equation (4.30) [21].

$$S_{\Omega}(f) = \frac{1}{2}\Omega_0{}^2[\delta(f - f_p) + \delta(f + f_p)] \tag{4.30}$$

$\Omega_0 = magnitude\,of\,noise$
$f_p = particular\ frequency$
$\delta = dirac\ function$

There are some relationships in Allan deviation curve of sinusoidal noise if it is not corrupted by another noise source. These relationships are given below:

- Peak values of sinusoidal noise decrease as time index increases. Slope of the line formed by combining peak values of sinusoidal noise is -1.
- Slope of the curve at the first peak is +1.
- Substituting Equation (4.30) into (4.13) gives Equation (4.31). According to this equation, magnitude of sinusoidal noise can be determined.

$$\sigma(\tau) = \frac{\sin^2(\pi f_p T)}{\pi f_p T}\Omega_0 \tag{4.31}$$

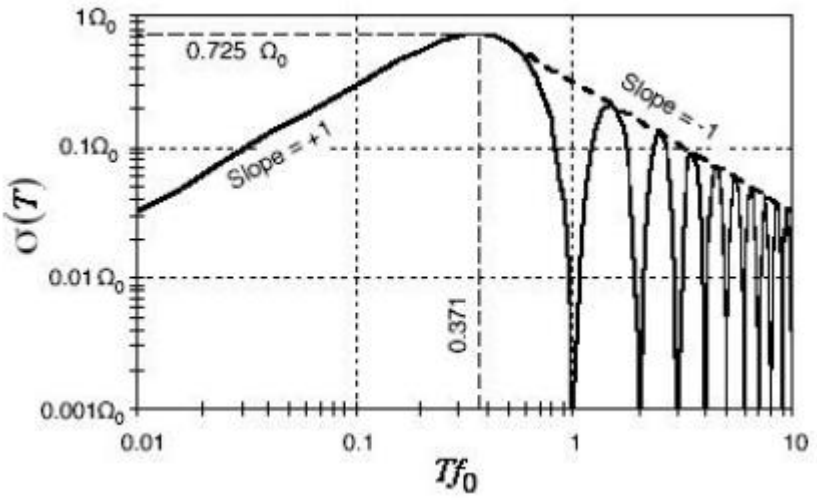

Figure 43 Representation of sinusoidal noise in Allan deviation curve [11] .

A real accelerometer data example of sinusoidal noise is given in Figure 44. The signal in this figure satisfies the sinusoidal noise criteria. This information is crucial for IMU design because sinusoidal noise has to be filtered or the source of the error must be investigated in order to increase the accuracy of the IMU.

Frequency information of sinusoidal data can be found from the autocorrelation function or FFT. The data which Allan deviation curve is obtained in Figure 44 is affected by two different sinusoidal sources and frequencies of these sinusoidal sources are 8.3 Hz and 25 Hz. Our system can be influenced by these sinusoidal signals and they may be in the measured frequency range. Therefore, source of sinusoidal noise has to be inspected. Autocorrelation function of affected data is given in Figure 45. Before performing this autocorrelation analysis, data has to be filtered out, because of the correlated noises.

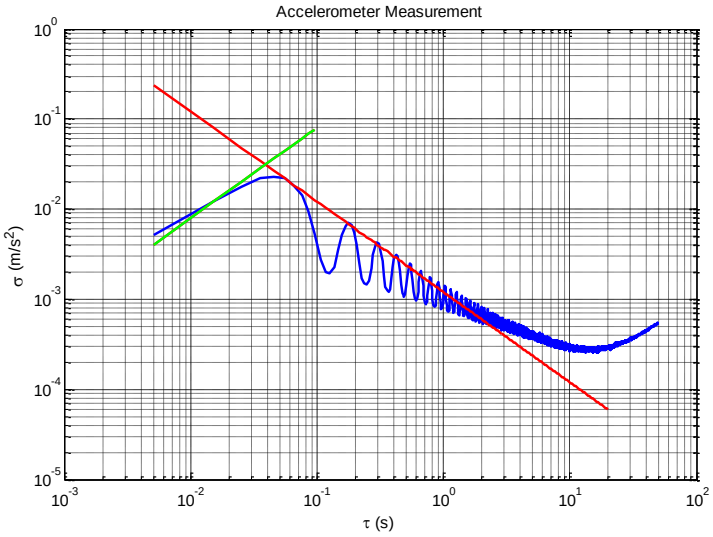

Figure 44 Allan deviation curve of an accelerometer that is effected by the sinusoidal noise. Green line indicates that slope is +1, red line represents that slope is -1.

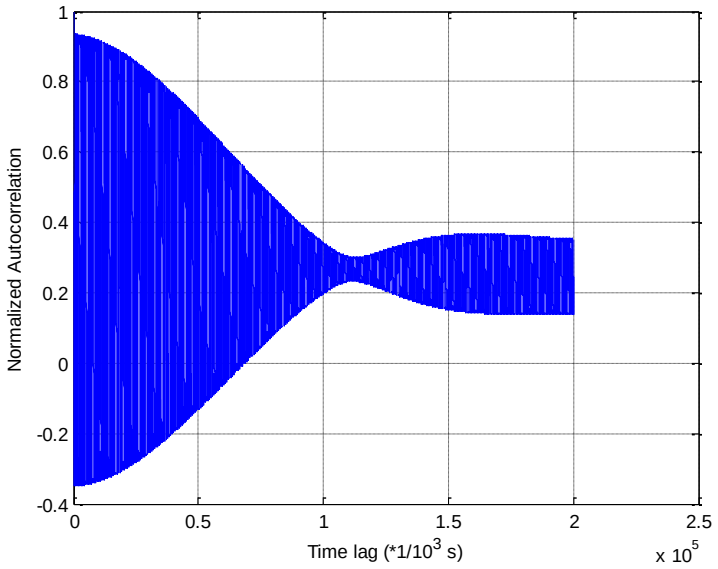

Figure 45 Autocorrelation function of an accelerometer. This data is affected by the sinusoidal noise.

One supposes that there is nothing abnormal in Allan deviation curve, which is given in Figure 46 at the first glance. Yet, it has some suspicious bulges in the

angle/velocity random walk side. Therefore, this data can be analyzed with autocorrelation function.

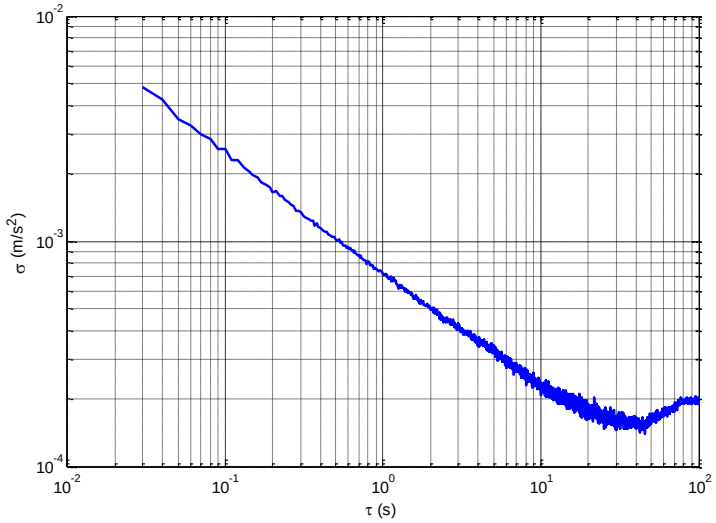

Figure 46 Allan deviation curve of a quartz accelerometer. This accelerometer is also affected by sinusoidal noise. There are some bulges at velocity random walk region.

Figure 47 shows the close view of angle/velocity random walk region and some bulges can be observed from this figure. Therefore, autocorrelation analysis can be performed with this data in order to reveal sinusoidal characteristic of the data.

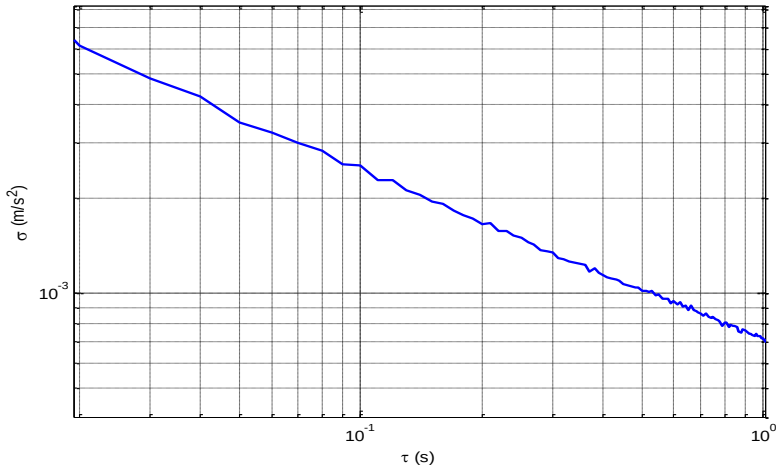

Figure 47 Suspicious bulges in the velocity random walk region.

Autocorrelation function of data is given in Figure 48; and it is obvious this data is also affected by sinusoidal noise.

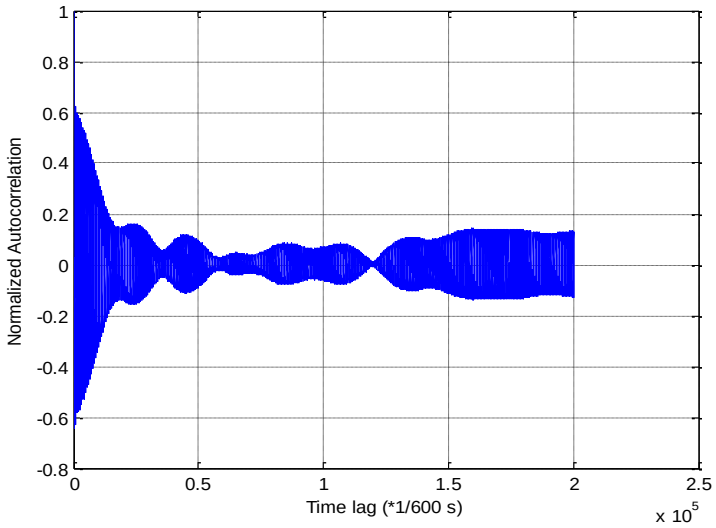

Figure 48 Autocorrelation function of a quartz accelerometer. Sinusoidal noise cannot be directly detected from Allan deviation curve.

To sum up, all of the methods are summarized in the Table 5.

Table 5 Comparison of different error estimation methods.

Parameter	Autocorrelation	Allan Deviation	PSD
Sinusoidal	+	+	-
Quantization	-	+	+
ARW/VRW	-	+	+
Bias Instability	-	+	+
Time Constant	-	+	-
Rate Random Walk	-	+	+
Bandwidth	-	-	+

+ = Applicable

- = Not Applicable

4.4 Error Parameter Estimation with Proposed Method

Allan deviation is the one of the main method to find random errors of an inertial sensor, as indicated before. Yet, line method is very intuitive because line can be intersected with the Allan deviation curve after several iterations. Additionally, line method is disturbed by another dominant noise and it causes incorrect estimation of error term. Therefore, we can use the dominant region of the specific error terms and estimate error through this method.

Another important argument of this chapter is that we can extract an equation which satisfies sigma values of Allan deviation curve for each time (tau) value as given by,

$$\sigma(\tau_k) = \frac{Q\sqrt{3}}{\tau_k} + \frac{N}{\sqrt{\tau_k}} + B\sqrt{\frac{2\ln 2}{\pi}} + K\sqrt{\frac{\tau_k}{3}}$$

$$Q = quantization\ error$$

$$N = angle / velocity\ random\ walk \tag{4.32}$$

$$B = bias\ instability$$

$$K = rate\ random\ walk\ coefficient$$

Equation (4.32) is a generic equation for all kind of inertial sensors. For example, if an RLG is modeled, B and K may be selected as zero because we know that RLG generally does not have bias instability and rate random walk errors. This structure satisfies another important advantage that we do not have to investigate all of the errors individually; therefore, arbitrary lines are not required. Yet, equation (4.32) needs some important modifications to satisfy that all random errors are suited with their exact values.

These modifications are separate errors in time because, usually, only one random error dominates Allan deviation curve in a specific time range. Therefore, a membership function is used to modify Equation (4.32) , indicating the dominated time range. For instance, angle random walk is dominating error term up to correlation time of bias instability; bias instability becomes dominant term after correlation time. Modified generic random error equation can be stated as,

$$\sigma(\tau_k) = \alpha_1(\tau_k)\frac{Q\sqrt{3}}{\tau_k} + \alpha_2(\tau_k)\frac{N}{\sqrt{\tau_k}} + \alpha_3(\tau_k)B\sqrt{\frac{2\ln 2}{\pi}} + \alpha_4(\tau_k)K\sqrt{\frac{\tau_k}{3}}$$

$$Q = quantization\ error$$

$$N = angle\ /\ velocity\ random\ walk$$

$$B = bias\ instability \tag{4.33}$$

$$K = rate\ random\ walk\ coefficient$$

$$\alpha_n(\tau_k) = membership\ \ functions$$

$$k = 1, 2, ..., p(total\ tau\ points)$$

$$n = number\ of\ error\ terms$$

Membership functions change their values between one and zero in different time zones; thus, we can adapt a special error term in a special time zone. Mathematical expression of membership function is stated as,

$$\alpha_n(\tau_k)=\begin{cases}0,\tau_k>\tau_{s+p}\\ 1-\dfrac{\tau_k-\tau_{s+p-r}}{\tau_{s+p}-\tau_{s+p-r}},\tau_{s+p-r}<\tau_k\le\tau_{s+p}\\ 1,\tau_{s+p-r}>\tau_k>\tau_s\\ \dfrac{\tau_k-\tau_{s-m}}{\tau_s-\tau_{s-m}},\tau_s>\tau_k>\tau_{s-m}\\ 0,\tau_{s-m}>\tau_k\end{cases}$$

$$\alpha_1(\tau_k)+\alpha_2(\tau_k)+\ldots+\alpha_n(\tau_k)=1$$

$$\tau_s=correlation\,time\,of\ specific\,error\,term \qquad (4.34)$$

$$\tau_{s-m}=last\,dominant\,time\,index\,for\,previous\,error\,term$$

$$\tau_{s+p-r}=last\,dominant\,time\,index\,for\,present\,error\,term$$

An illustration of a membership function is given in Figure 49,

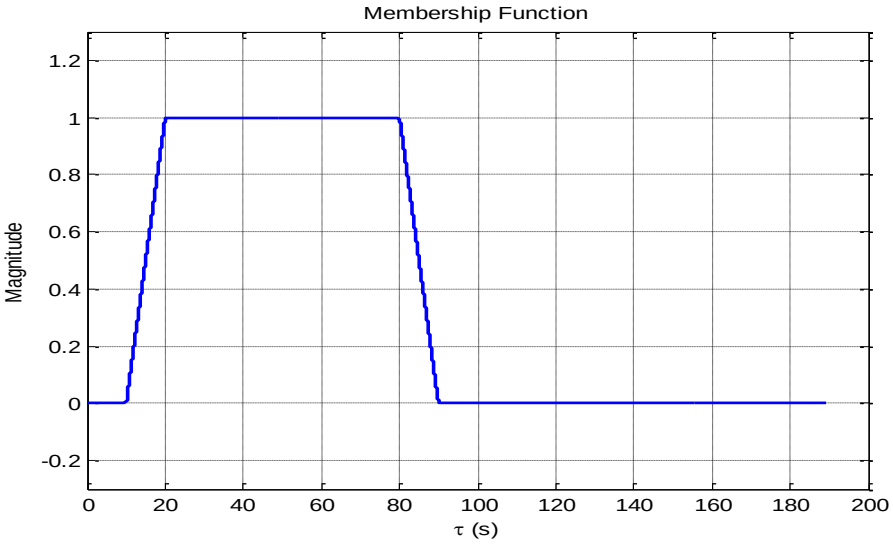

Figure 49 An example of a membership function

All of the error parameters are included in the state parameter vector and each error parameter has to be estimated. In this thesis, least-square estimation is used to estimate error terms. Therefore, we have to express error parameters in the matrix form. Matrix representation of Equation (4.33) is given by,

$$\underbrace{\begin{bmatrix}\sigma(\tau_1)\\ \sigma(\tau_2)\\ \vdots\\ \sigma(\tau_k)\end{bmatrix}}_{y} = \underbrace{\begin{bmatrix} \alpha_1(\tau_1)\frac{\sqrt{3}}{\tau_1} & \alpha_2(\tau_1)\frac{1}{\sqrt{\tau_1}} & \alpha_3(\tau_1)\sqrt{\frac{2\ln 2}{\pi}} & \alpha_4(\tau_1)\sqrt{\frac{\tau_1}{3}} \\ \alpha_1(\tau_2)\frac{\sqrt{3}}{\tau_2} & \alpha_2(\tau_2)\frac{1}{\sqrt{\tau_2}} & \alpha_3(\tau_2)\sqrt{\frac{2\ln 2}{\pi}} & \alpha_4(\tau_2)\sqrt{\frac{\tau_2}{3}} \\ & & \vdots & \\ \alpha_1(\tau_k)\frac{\sqrt{3}}{\tau_k} & \alpha_2(\tau_k)\frac{1}{\sqrt{\tau_k}} & \alpha_3(\tau_k)\sqrt{\frac{2\ln 2}{\pi}} & \alpha_4(\tau_k)\sqrt{\frac{\tau_k}{3}} \end{bmatrix}}_{H} \underbrace{\begin{bmatrix}Q\\ N\\ B\\ K\end{bmatrix}}_{x} \tag{4.35}$$

Error parameters are estimated by the least-square estimation. Details about this method are given in [4]. One important problem of Allan deviation technique is the determination of lines with suitable slopes accurately. Therefore, the line method gives approximate values of error parameters, but these levels sometimes are not accurate enough. For example, sinusoidal noise has effect on quantization noise region and this situation causes wrong estimation of quantization error parameter. If we take the corresponding value of the τ = 1 s in Allan deviation curve, we would have some errors in the estimated parameter.

The proposed method finds the error parameters for given Allan deviation values. Additionally, there is no special merit to look for each error term. Least-square method is applied to calculated error terms as indicated in Equation (4.36), but the important problem is to decide the true time indices of membership functions.

$$x = (HH^T)^{-1}H^T y \tag{4.36}$$

As discussed earlier, noise parameters have some important properties in the Allan deviation curve:

- Quantization error can be identified from smaller than the 0.5 s region of the Allan deviation curve.
- Time index of angle/velocity random walk is between 0.5 s and the correlation time of bias instability.
- Bias instability is the dominant error term from correlation time of bias instability to starting time of rate random walk. Furthermore, when τ approaches to correlation time of bias instability, slope of Allan deviation curve converges to zero.

Allan deviation is scattered too much when the higher time (tau) values come into investigation. Hence, if a polynomial is fitted to an Allan deviation curve, we can find the correlation time of bias instability and starting time of rate random walk. Polynomial is formed by exponential terms and their powers to perform the curve fitting.

If we analyze the simple Allan deviation curve, which is given in Figure 50, we can see the important indicators about time indices. Firstly, when the bias instability becomes correlate, slope of the Allan deviation curve is zero; thus, investigation of zero slope gives time constant. Moreover, rate random walk produces a local minimum point in the Allan deviation curve.

An example is shown to simplify the discussions above. A gyroscope of MEMS-IMU is used in this example. First of all, we extract the sigma values of Allan deviation curve for given time indices.

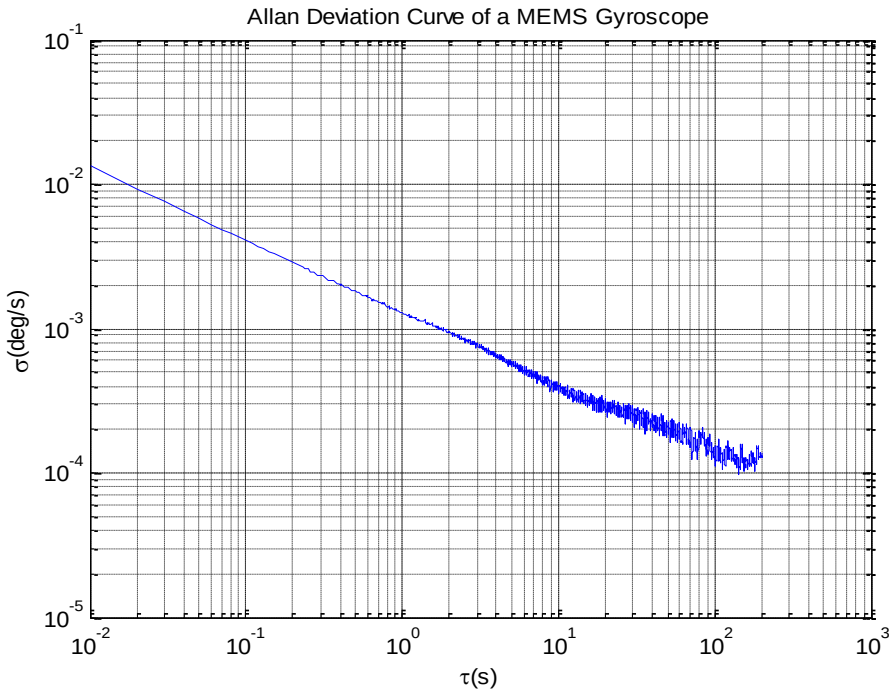

Figure 50 Allan deviation curve of a MEMS-Gyro

Secondly, we can fit a Gaussian expression to this curve; mathematical expression of the curve is given by,

$$y(x) = \sum_{n=1}^{8} a_n e^{-\left(\frac{x-b_n}{c_n}\right)^2} \tag{4.37}$$

$$x = any\ point\ on\ Allan\ deviation\ curve$$

$$a_n, b_n, c_n = coefficients\ of\ Gaussian\ expression$$

Before performing the fitting process, we take natural logarithm of both sigma and tau values, since Allan deviation works on the logarithmic plane. Coefficients in Equation (4.37) can be found by nonlinear estimation techniques and trust-region method is selected to determine these coefficients. Figure 51 shows the fitted curve and real Allan deviation curve.

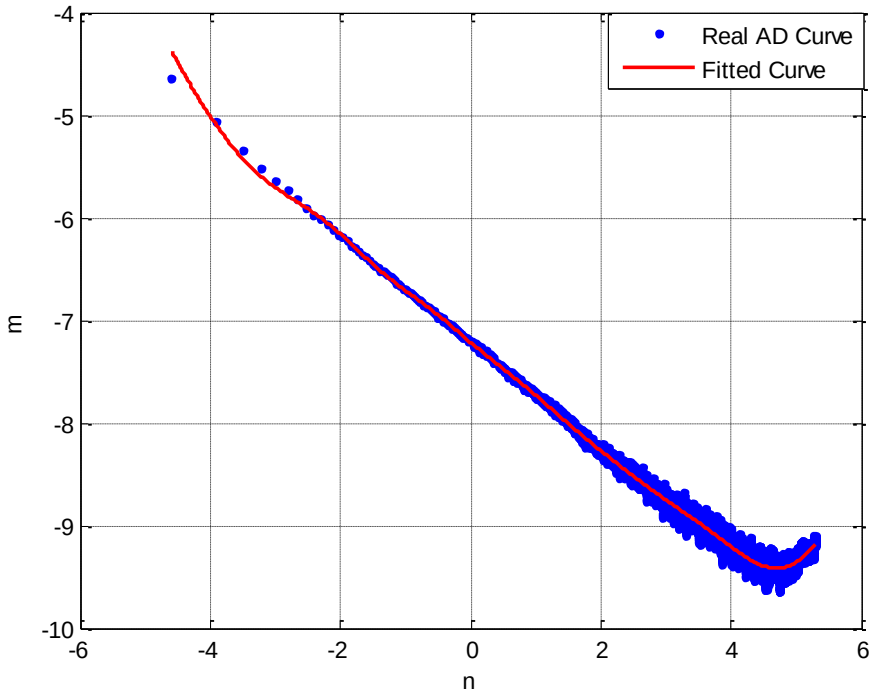

Figure 51 Fitted curve and real Allan deviation curve.

As mentioned before, due to the rate random walk a local minimum occurs; therefore, we have to find a local minima of this curve.

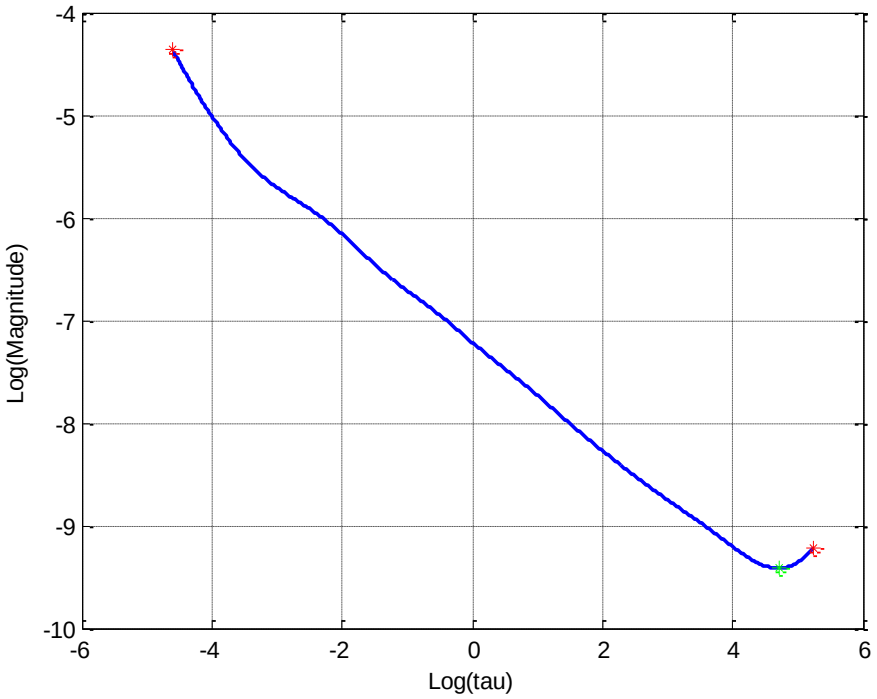

Figure 52 Local minimum (green) and local maximum (red) points.

As shown in Figure 52, green point indicates the minimizing point. Exponential of this point gives time index of the starting time of the rate random walk. Starting time of rate random walk equals to 154.8 s in this example. Membership functions can be set according to this information. Transition region between angle random walk and rate random walk is selected as 10 s. This region is selected according to general behavior of error terms. Membership functions can be formed by Equation (4.34), resulting functions are shown in Figure 53

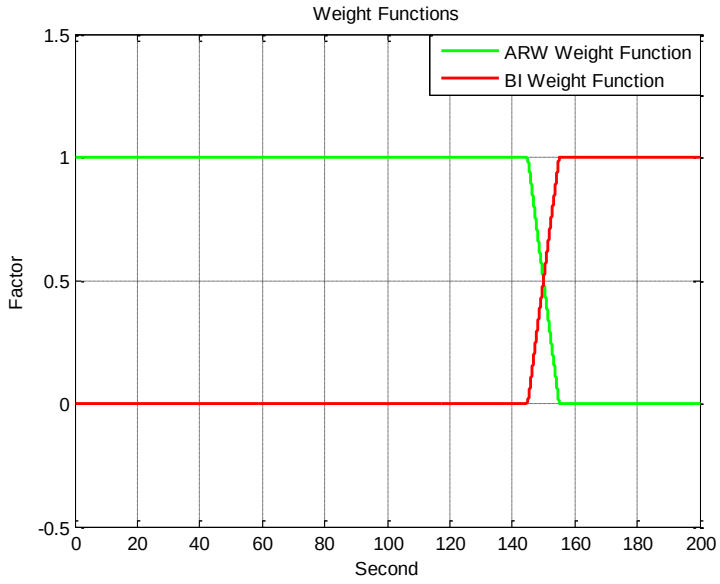

Figure 53 Membership functions for rate random walk and angle random walk

When the rate random walk reaches the time constant value, the associated membership function value is one. Last step of proposed method is the estimation of error parameters. Simplification of Equation (4.35) for this example is given in Equation (4.38). Least-square estimation is performed according to Equation (4.36) to find the error parameters.

$$\underbrace{\begin{bmatrix} \sigma(\tau_1) \\ \sigma(\tau_2) \\ \vdots \\ \sigma(\tau_k) \end{bmatrix}}_{y} = \underbrace{\begin{bmatrix} \alpha_{ARW}(\tau_1)\frac{1}{\sqrt{\tau_1}} & \alpha_{RRW}(\tau_1)\sqrt{\frac{\tau_1}{3}} \\ \alpha_{ARW}(\tau_2)\frac{1}{\sqrt{\tau_2}} & \alpha_{RRW}(\tau_2)\sqrt{\frac{\tau_2}{3}} \\ \vdots & \\ \alpha_{ARW}(\tau_k)\frac{1}{\sqrt{\tau_k}} & \alpha_{RRW}(\tau_k)\sqrt{\frac{\tau_k}{3}} \end{bmatrix}}_{H} \underbrace{\begin{bmatrix} N \\ K \end{bmatrix}}_{x} \tag{4.38}$$

Q and B parameters are selected as zero, because these terms are not observed in the Allan deviation curve. Table 6 shows the estimation results of the proposed method and the line method [7, 11]

Table 6 Estimated error parameters with different method

Method	Angle Random Walk (deg/√h)	Rate Random Walk (deg/h/√s)	Time Constant of RRW (s)
Proposed Method	0.078	0.059	154.8
Line Method	0.078	0.062	140

The major difference between the two methods is the magnitude of the rate random walk. It is, of course, due to the different measurement principles of these two methods. The proposed method finds the exact minimum point of the Allan deviation curve to investigate time constant of the rate random walk; but the line method says that when the slope of curve changes the corresponding time value can be selected as time constant. This example will be expanded in the next section for different inertial sensors. The proposed method also has very promising results for certain types of inertial sensors.

Steps of the proposed method are shown below:

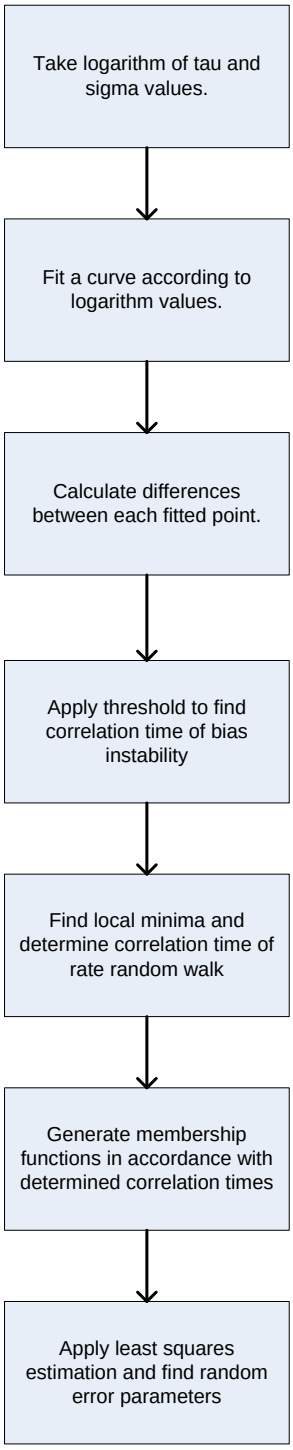

Figure 54 Flow diagram of the proposed method

CHAPTER 5

MODELING OF AN INERTIAL SENSOR

According to previous chapters, inertial sensor data is affected by deterministic and stochastic errors. Deterministic errors change with temperature and stochastic errors are usually dependent on time, as indicated before. Therefore, temperature dependency of deterministic errors and time variant characteristic of stochastic errors must be included in an inertial sensor model. Before performing Allan deviation tests, temperature dependency of such errors has to be defined, because performance of Allan deviation and other stochastic models are related to the deterministic error compensation techniques. Polynomial fitting is a common way to interpolate the deterministic errors. Calibration tests are performed under different temperatures by soak method [4]. Therefore, an algorithm which compensates deterministic errors must include a proper interpolation method such that linear interpolation, cubic spline and polynomial fitting [4, 5]. In addition, third, fourth and fifth-order polynomial fitting methods are performed in literature [4, 5]. Generally third or fourth order polynomial fitting is enough for deterministic errors [4]. Degree of polynomial fitting is important for the processing time of algorithm which is embedded in IMU processor. The more multiplication operations are, the more algorithm process time is [6]. On the other hand, modeling stochastic errors also improves the navigation accuracy [13]. To obtain better results, Kalman filtering is executed by INS processor to estimate stochastic errors. If one wants sensitive estimations of stochastic errors, number of states increases inevitably. This situation is another important problem when algorithms are executed in a processor.

An IMU error compensation algorithm or more generally, an IMU algorithm contains 4 steps: Digital to physical data conversion, data filtering, deterministic

error compensation and stochastic error estimation [2]. Therefore, IMU data modeling must include all of these steps. Additionally, some parameters of IMU stochastic data modeling, such as time constant, random error coefficients, etc. are obtained by post-processing.

5.1 Modeling Deterministic Errors

Deterministic errors (bias, scale factor, misalignment, g-dependent error) have to be modeled with temperature information after the calibration process. Magnitude of deterministic error is constant for certain temperature points [19, 20]. It means that there is no hysteresis for deterministic errors. Hence, look-up tables and fitting methods are used to model deterministic error.

Least-square technique is used for the estimation of deterministic error parameters. IMU tests are performed in different orientations for accelerometers and different angular rate for gyroscopes. Two methods are supposed in the literature: six position tests and multi position tests. Six position tests are performed in six different orientations to extract deterministic error parameters of an accelerometer. Multi position tests are executed for the same purpose; but the main difference between the two methods is the number of positions. In this thesis work, IMU calibration tests are performed under different temperatures. Calibration tests are thermal calibration of inertial systems; it means that temperature characteristics of deterministic errors are defined. Polynomial coefficients are obtained after calibration tests.

Changes in bias, misalignment and scale factor errors with respect to the temperature are also deterministic errors and polynomial fitting method is used to extract these errors from IMU raw data. Effect of g-dependent bias changes with applied acceleration; therefore, accelerometer data has to be obtained. G-dependent bias has to be multiplied with acceleration data and this value is subtracted from the gyroscope data.

Degree of polynomial is another important point of calibration process. A fourth degree polynomial is chosen for IMU deterministic error models.

Temperature information is needed for IMU deterministic error calibration. If any inertial sensor does not include temperature information, some methods are available to provide temperature information. Firstly, an additional temperature sensor may be attached to a PCB. Another option is having a temperature sensor directly attached to sensor structure. Finally, temperature of chamber can be obtained and this information is used in calibration process.

Temperature dependent deterministic error formula is given below:

$$B_x = a_1 + a_2 T + a_3 T^2 + a_4 T^3 + a_5 T^4 \tag{5.1}$$

$$B_x = bias\,error$$

$$T = temperature$$

$$a_1, a_2, a_3, a_4, a_5 = polynomial\,coefficients$$

One important point is that we have to collect raw data under 5 different thermal conditions, because the degree of polynomial is 4 (maximum degree of polynomial equals to n-1 where n = data points). The same procedure is applied to scale factor and misalignment errors. Difference between two temperature points is not chosen too separately but frequent temperature points increase test duration.

In this error modeling, IMU has 3 accelerometers and 3 gyroscopes. Therefore, we split temperature information into 3 individual accelerometer temperature measurements, because each inertial sensor has different polynomial coefficients.

Sometimes, it is impossible to know temperature dependency of deterministic errors. In this case, repeatability takes into account, since, if 1σ value of deterministic error is known, in worst case, error effects outputs at 3σ value. Hence, a random error generator (e.g., zero mean with known variance) is used to model this error. This kind of model is useful for Monte-Carlo analysis.

The same procedure is valid for scale factor error. Yet, misalignment error is different from others because there are 6 different misalignment parameters. These are misalignment between x and y axes, x and z axes, y and x axes, y and z axes, z and x axes, z and y axes.

Deterministic sensor errors are removed from raw inertial sensor data according to equations below, at each initialization.

$$A_c = M_{acc}^{-1}\left(S_{acc}^{-1}A_{uc} - B_{acc}\right) \tag{5.2}$$

$$W_c = M_{gyr}^{-1}\left(S_{gyr}^{-1}W_{uc} - B_{gyr} - GA_c\right) \tag{5.3}$$

$$B = Bias\,vector$$

$$M = Misalignment\,matrix$$

$$S = Scale\ factor\,matrix$$

$$G = g - dependent\,bias\,matrix$$

$$A_{uc} = uncompensated\,accelerometer\,data$$

$$A_c = compensated\,accelerometer\,data$$

$$W_{uc} = uncompensated\ gyroscope\,data$$

$$W_c = compensated\ gyroscope\,data$$

Gyroscope measurements are affected by scale factor errors, constant bias error, misalignment error and g-dependent error. All errors have the same modeling principle with accelerometer, but additional g-dependent bias has to be omitted.

5.2 Modeling Stochastic Errors:

Stochastic error parameters are identified by several methods such as autocorrelation, Allan Variance and PSD as explained in previous chapter. These methods reveal some important noise parameters (i.e., angle/velocity Random Walk, bias instability, time constant). Modeling of stochastic errors is a complicated problem; because one may consider the specific error type dependent on the application, time duration and sensor type etc. For example, angle/velocity random walk is inserted into all stochastic models because it corrupts all measurements. MEMS sensors do not integrate their measurements. Therefore, modeling the quantization error is not useful for MEMS sensors. If a vehicle/missile which has a ring laser gyro (RLG) working for ten seconds, then bias instability may not correlate it to the sensor output. Therefore, modeling bias instability is not a critical problem for this RLG application.

Stochastic errors are meaningful together with their difference equations, since state space equations of different error sources are primarily used by error estimation techniques (i.e., Kalman Filters) [7]. Some inertial sensors include deterministic disturbances; for example, dithering is a common application in ring laser gyros due to the lock-in phenomena and these kind of artificial effects have to be modeled. IMUs generally consist of dampers, which remove the additional vibration from the inertial sensor data. Bandwidth of an inertial sensor is usually not known exactly. PSD analysis satisfies good approximation to find the bandwidth. Bandwidth of a sensor has to be known, because magnitude of stochastic errors is also affected by filters. Thus, all of these effects have to be taken into account for IMU modeling. In this section, differential equation of each error terms will be given; and implementation of stochastic error parameters on difference is explained.

5.2.1 Quantization Error (Non-Integrating White Noise)

PSD function of quantization error is given as,

$$S_{\Omega}(f) = (2\pi f)^2 Q^2 \Delta t$$
$$Q = quantization\ error\ \ parameter \tag{5.4}$$
$$\Delta t = sampling\ \ period$$

Equation (5.4) can be considered as the output of a shaping filter. Details about the shaping filter can be found in [23]. Therefore, PSD function of input is unity.

$$S_{quant}(jw) = H(jw) S_w(jw) H^*(jw) \tag{5.5}$$

$$S_w(jw) = 1 \tag{5.6}$$

$$(2\pi f)^2 Q^2 T = H(jw).1.H^*(jw) \tag{5.7}$$

$$H(s) = sQ\sqrt{\Delta t} \tag{5.8}$$

$$H(s) = \frac{X(s)}{W(s)} = sQ\sqrt{\Delta t} \tag{5.9}$$

$$X(s) = sW(s)Q\sqrt{\Delta t} \tag{5.10}$$

Taking the inverse Laplace of Equation (5.10) gives,

$$x(t) = Q\sqrt{\Delta t}\,\dot{w}(t) \tag{5.11}$$

At that point, discretization process can be explained. First of all, assume that we have a linear system in the following form,

$$\begin{aligned} \dot{x}(t) &= Ax(t) + Bu(t) + w(t) \\ y(t) &= Cx(t) + Du(t) + n(t) \end{aligned} \tag{5.12}$$

$w(t)$ and $n(t)$ are process and measurement noise terms, respectively and these terms are distributed according to $N(0,\sigma_w{}^2)$ and $N(0,\sigma_n{}^2)$. Suppose that, $u(t)$ is passed through a zero-order hold system, Equation (5.12) is discretized as,

$$\begin{aligned} x[k+1] &= A_d x[k] + B_d u[k] + w[k] \\ y[k] &= C_d x[k] + D_d u[k] + n[k] \end{aligned} \tag{5.13}$$

$w[k]$ and $n[k]$ are distributed according to $N(0,\bar{\sigma}_w{}^2)$ and $N(0,\bar{\sigma}_n{}^2)$ other discretization equations can be summarized as,

$$\begin{aligned} A_d &= e^{A\Delta t} \\ B_d &= \left(\int_{\tau=0}^{\Delta t} e^{A\tau} d\tau \right) B \\ C_d &= C \\ D_d &= D \\ \bar{\sigma}_w{}^2 &= \int_{\tau=0}^{\Delta t} e^{A\tau} \sigma_w{}^2 e^{A^T\tau} d\tau \\ \bar{\sigma}_n{}^2 &= \frac{\sigma_n{}^2}{\Delta t} \end{aligned} \tag{5.14}$$

Equation (5.11) is not directly discretized because it does not satisfy the conditions of Equation (5.12). Additionally, Equation (5.11) cannot be implemented physically [28], but according to definition of the error term, quantization error is approximated by Equation (5.15).

$$\begin{aligned} x[k] &= \frac{Q}{\Delta t} w[k] \\ y[k] &= x[k] - x[k-1] \end{aligned} \tag{5.15}$$

$$Q = \textit{Quantization error coefficient}$$

$$\Delta t = \textit{sampling interval}$$

Quantization noise can be seen on the output of a rate or acceleration integrated sensors [28]. RLG is a rate integrated sensor; therefore, slope of -1 regime can be obtained from Allan deviation curve. Quantization noise does not accumulate with time as shown in Equation (5.15). Moreover, quantization error is not a dominant error source for MEMS accelerometers, MEMS gyros and quartz sensors.

5.2.2 Angle/Velocity Random Walk

Angle/Velocity random walk corrupts output of all types of sensor. Hence, it affects the measurements of an inertial sensor as white noise [8]. Continuous time expression of Angle/Velocity random Walk is given below:

$$y_{arw}(t) = \frac{N}{\sqrt{\Delta t}} w(t)$$
$$w(t) \sim N(0,1) \tag{5.16}$$

$$N = angular/velocity\ random\ walk\ coefficient$$

$$\Delta t = sampling\ rate$$

Discrete time expression of Equation (5.16) is given by

$$y_{arw}[k] = \frac{N}{\sqrt{\Delta t}} w[k]$$
$$w[k] \sim N(0,1) \tag{5.17}$$

5.2.3 Exponentially Correlated Noise

Exponentially correlated noise can be approximated by Gauss-Markov process [7, 13]. If one attempts to model correlated noise with autoregressive or autocorrelation

methods, collected data can be put into a filtering process [7, 24]. On the other hand, Gauss-Markov process needs correlation time and bias instability coefficient and these parameters can be found from Allan deviation curve [7].

Here, correlated noise has to be considered if correlation time is smaller than the total working time from turn on to turn off. For instance, Allan deviation curve of RLG sensors usually does not represent correlated noise for small tau values. The same condition is valid for quartz MEMS sensors. Yet, correlated noises become one of the major error sources for MEMS sensors.

Gauss-Markov process is a suitable approximation for modeling slope of zero region of Allan deviation curve, since formulations of Allan deviation and Gauss-Markov process can be approximately matched in slope of zero region [20]. Autoregressive process is another option, but it does not include time constant and sampling time of an inertial sensor [20]. Additionally, noise term of autoregressive process does not have any information from Allan deviation curve [7].

Gauss-Markov process can be given as [15, 20],

$$\begin{aligned} x[k+1] &= e^{-\frac{\Delta t}{T_c}} x[k] + \sigma_{corr}\sqrt{1-e^{-\frac{2\Delta t}{T_c}}}\, w[k] \\ y[k] &= x[k] \\ \sigma_{corr} &= 0.618\sigma_{BI} \\ w[k] &\sim N(0,1) \end{aligned} \tag{5.18}$$

σ_{BI} is selected as bias instability parameter which is identified by Allan deviation method or the proposed method. T_c is an unknown parameter but two methods are available to determine the time constant, namely autocorrelation and Allan variance [3, 11].

These methods to estimate T_c value are detailed below:

- Autocorrelation method is applied after sensor filtering process as mentioned in Section 4.1, and corresponding time value of % 36.8 point of autocorrelation function is equal to the correlation time.
- When the regime of Allan deviation becomes flat, related tau value determines the correlation time.

5.2.4 Bias Instability

PSD function of the bias instability noise is given in Equation (5.19)

$$S_{\Omega}(f) = \frac{B^2}{2\pi f} \tag{5.19}$$

If Equation (5.19) is solved by a shaping filter, denominator of system transfer function includes square root of frequency component. Therefore, this error cannot be simulated with common methods.

5.2.5 Rate Random Walk

Rate random walk has low-frequency characteristic and therefore, this error is obtained from higher tau values [20]. Therefore, if an inertial sensor works in short-range applications this error may not be modeled. Mathematical expressions of rate random walk are given below,

$$S_{rrw}(f) = \frac{K^2}{(2\pi f)^2} \tag{5.20}$$

$$S_{rrw}(jw) = H(jw)S_w(jw)H^*(jw) \tag{5.21}$$

Input of shaping filter, which converts the white noise input to rate random walk process. Hence, PSD function of input is unity.

$$S_w(jw) = 1 \tag{5.22}$$

$$\frac{K^2}{(2\pi f)^2} = H(jw).1.H^*(jw) \tag{5.23}$$

According to Equation (5.21), transfer function of shaping filter is given by,

$$H(s) = \frac{K}{s} \tag{5.24}$$

Therefore,

$$\frac{X(s)}{W(s)} = \frac{K}{s} \tag{5.25}$$

$$sX(s) = Kw(s) \tag{5.26}$$

Taking the inverse-Laplace transform gives,

$$\begin{aligned} \dot{x}(t) &= Kw(t) \\ y(t) &= x(t) \\ w(t) &\sim N(0,1) \end{aligned} \tag{5.27}$$

Discrete-time equation of rate random walk is expressed below,

$$\begin{aligned} x[k+1] &= x[k] + K\sqrt{\Delta t}\ w[k] \\ y[k] &= x[k] \\ K &= \text{rate random walk coefficient} \\ \Delta t &= \text{sampling time} \end{aligned} \tag{5.28}$$

To sum up, we had identified all of the equations about the random inertial sensor errors. These equations are formed by discretization of continuous time equations of random errors. Some of errors become dominant with time; therefore, time duration of an application is important for IMU modeling. There are some constraints about modeling an IMU output. Firstly, filtering has important effects on random errors;

because of that, before modeling an IMU output we have to know the filtering structure. Secondly, some kinds of sensors (i.e., RLG) have disturbances in their measurements. For instance, dither movement of RLG sensors has to be modeled because these movement changes noise level of sensor. Thirdly, designers use insulator on their IMUs in order to prevent undesired vibrations. These insulators have some effect on stochastic errors of an inertial sensor because they work like a low-pass filter. Random error modeling structure is shown in Figure 55.

.

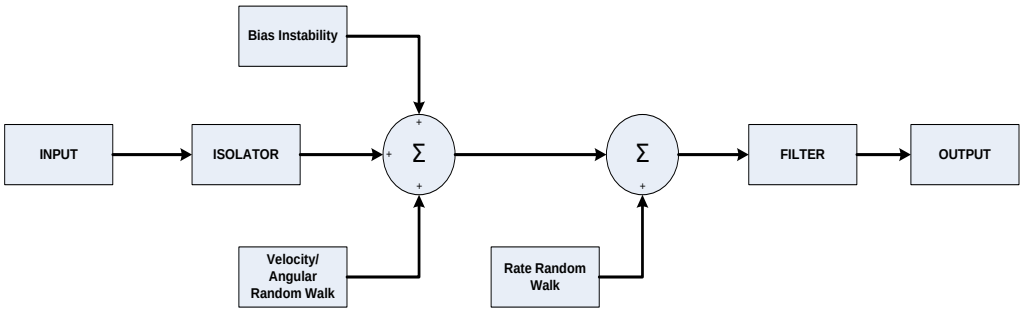

Figure 55 General modeling structure of a random inertial sensor data

CHAPTER 6

SIMULATION RESULTS OF IMU MODELING

Inertial sensors have different noise characteristics related to their structure and their materials. For example, optical sensors generally do not suffer from rate random walk for short cluster time (τ), but MEMS sensors are affected by rate random walk. Allan deviation curve shows errors in different slope regions and this implies that random errors have different frequency characteristic. Therefore, they have to be modeled by different random processes. Dampers and digital filters are modeled according to PSD or manual of inertial sensors. PSD is suitable method to reveal frequency characteristic of an inertial sensor. It also shows error parameters but identifying true error parameters is relatively hard because PSD spreads too much at high frequency thus frequency averaging is needed. Hence, Allan deviation method is selected as the main method to identify error parameters because it works in time domain and Allan deviation shows starting time of each correlated noise parameter.

Additionally, comparisons of proposed error estimation method and line methods are given for each sensor. In addition, all sensors are modeled by the line and the proposed methods. Model outputs of the line method, the proposed method and real data are compared with each other to show performance of the proposed method.

6.1 Modeling MEMS Sensors

6.1.1 Estimation of Sensor Errors with the Line Method for the MEMS IMU 1

MEMS sensors are usually influenced by angle/velocity random walk, bias instability and rate random walk errors. MEMS sensors can be affected by deterministic errors very dramatically, because of their structure. Allan deviation curve does not give any information about deterministic errors and levels of Allan deviation curve independent from the deterministic errors. Yet, temperature calibration has to be performed before performing Allan deviation tests.

Two different MEMS IMUs are investigated in this thesis work; one of them has automotive grade sensors, and the other one has tactical grade sensors Therefore, we expect different noise levels between Allan deviation curves. Before performing IMU modeling, we have to identify error parameters with calibrated IMU data. As indicated before, velocity random walk parameter can be found from slope of -1/2 line, bias instability is shown in flat region and Allan deviation curve demonstrates rate random walk in slope of +1/2 region. Bias instability parameter equals to 1.506 times of the minimum point of the flat region. Allan deviation results of control grade inertial sensors are given in Figure 56 to Figure 61.

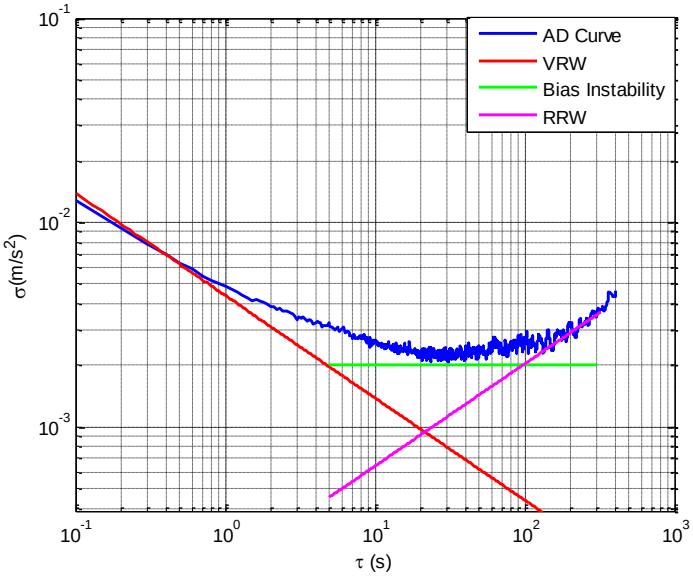

Figure 56 Allan deviation curve of the x-axis accelerometer of the MEMS IMU 1.

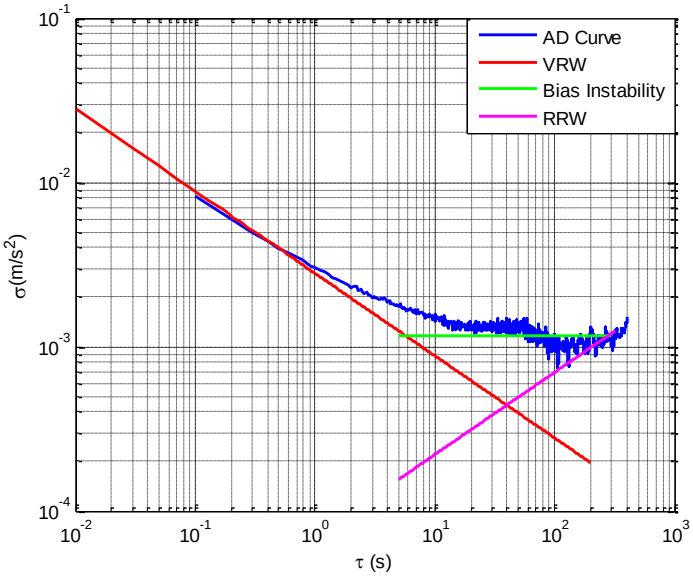

Figure 57 Allan deviation curve of the y-axis accelerometer of the MEMS IMU 1.

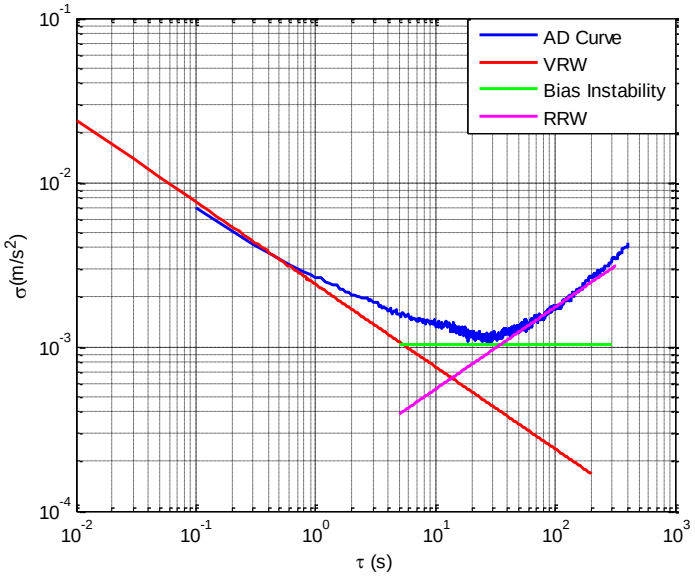

Figure 58 Allan deviation curve of z-axis accelerometer of the MEMS IMU 1.

Table 7 Error parameters of the accelerometers according to Allan Deviation curves.

Accelerometer	**Velocity Random Walk(mg/√Hz)**	**Bias Instability(m/s^2)**	**Rate Random Walk($m/s/h^{3/2}$)**	**Time constant (s)**
x-axis	0.4899	0.0031	75.6	20
y-axis	0.3062	0.0019	30.24	20
z-axis	0.2666	0.0016	64.8	20

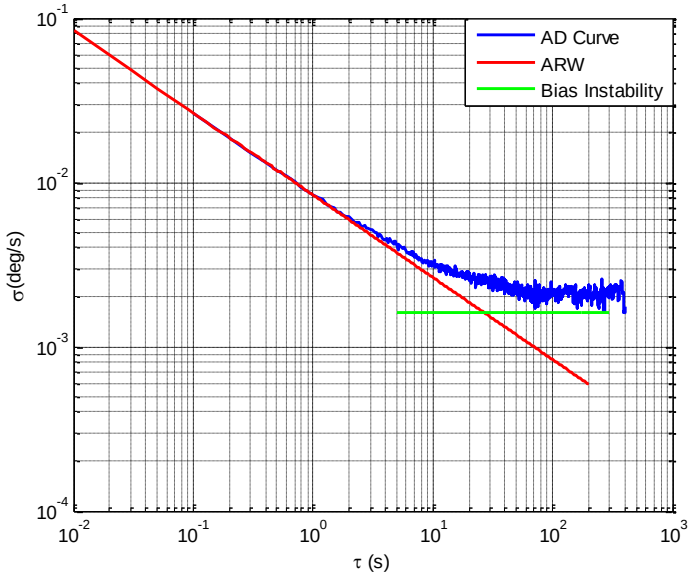

Figure 59 Allan deviation curve of x-axis gyroscope of the MEMS IMU 1.

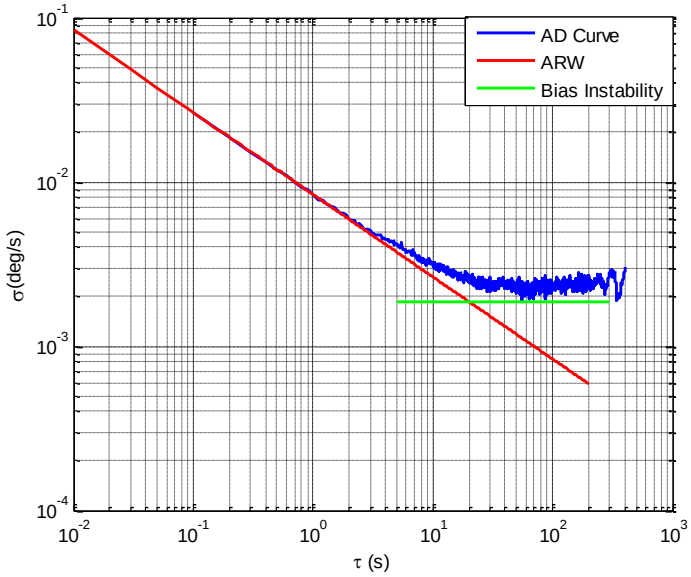

Figure 60 Allan deviation curve of the y-axis gyroscope of the MEMS IMU 1.

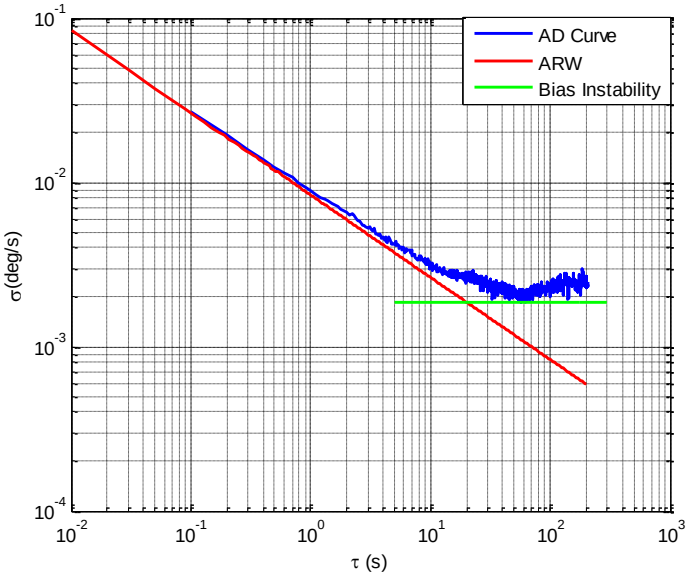

Figure 61 Allan deviation curve of z-axis gyroscope of the MEMS IMU 1.

Table 8 Gyroscope error parameters according to Allan deviation curve

Gyroscope	**Angle Random Walk(deg/√h)**	**Bias Instability (deg/h)**	**Time constant (s)**
x-axis	0.504	10.27	60
y-axis	0.504	10.14	50
z-axis	0.504	10.11	50

6.1.2 Estimation of Errors with Proposed Method for MEMS IMU 1

Same error components are identified by proposed method and each step of error parameter estimation will be explained in this section. First of all, we have to obtain natural logarithm equivalence of sigma and tau values for x-axis accelerometer and

we apply curve fitting method to prevent scattering. Fitted Allan deviation curve is given in Figure 62.

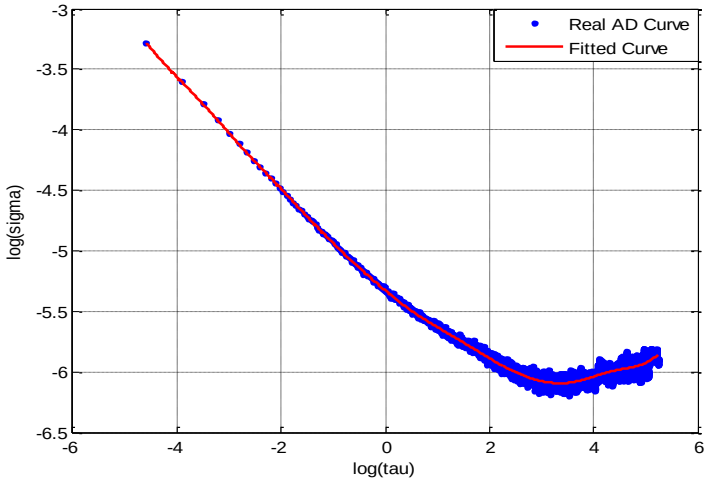

Figure 62 Real and fitted Allan deviation curves.

We perform the algorithm, which is stated in Section 4.4. According to algorithm, firstly we find the correlation time of bias instability. We set a threshold to estimate slope of zero, threshold value equals to 6.3×10^{-7} and it is constant for all sensors. In this example, correlation time of bias instability is 24 s. Additionally, we have to find local minimum points of the curve to define the starting time of the rate random walk.

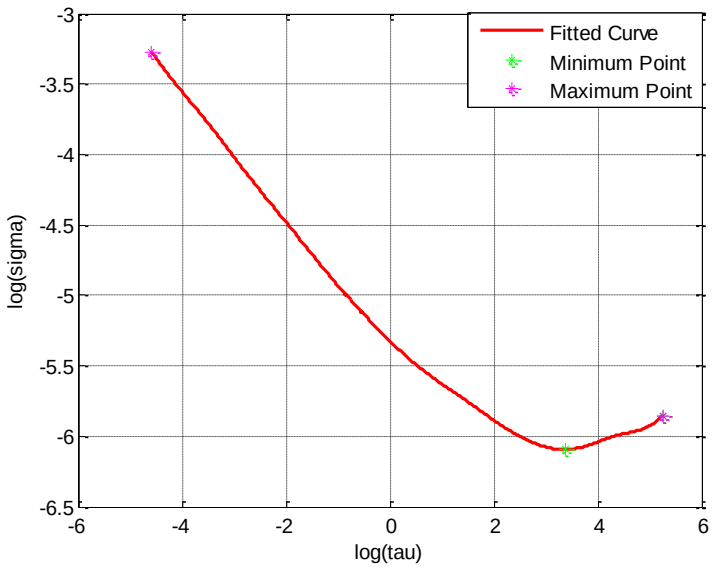

Figure 63 Minimum and maximum points of the fitted curve for x-axis accelerometer.

Figure 63 shows that minimum point of Allan deviation curve is 29.8 s. We have time indices about error terms and we can form the membership functions in accordance with the estimated correlation times.

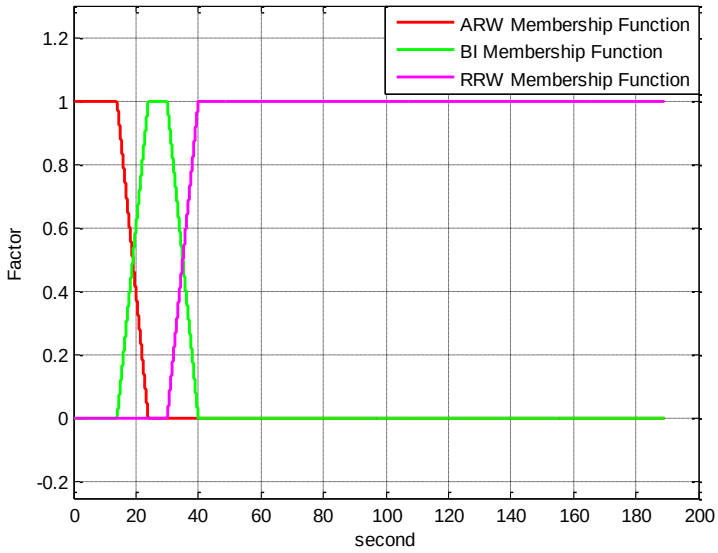

Figure 64 Membership functions for different error types.

Least square estimation, which is expressed in, (6.1) is performed to estimate three types of errors such as angle random walk, bias instability and rate random walk. Estimated errors are stated in the Table 9.

.

$$\underbrace{\begin{bmatrix}\sigma(\tau_1)\\ \sigma(\tau_2)\\ \vdots\\ \sigma(\tau_k)\end{bmatrix}}_{y} = \underbrace{\begin{bmatrix}\alpha_2(\tau_1)\frac{1}{\sqrt{\tau_1}} & \alpha_3(\tau_1)\sqrt{\frac{2\ln 2}{\pi}} & \alpha_4(\tau_1)\sqrt{\frac{\tau_1}{3}}\\ \alpha_2(\tau_2)\frac{1}{\sqrt{\tau_2}} & \alpha_3(\tau_2)\sqrt{\frac{2\ln 2}{\pi}} & \alpha_4(\tau_2)\sqrt{\frac{\tau_2}{3}}\\ & \vdots & \\ \alpha_2(\tau_k)\frac{1}{\sqrt{\tau_k}} & \alpha_3(\tau_k)\sqrt{\frac{2\ln 2}{\pi}} & \alpha_4(\tau_k)\sqrt{\frac{\tau_k}{3}}\end{bmatrix}}_{H} \underbrace{\begin{bmatrix}N\\ B\\ K\end{bmatrix}}_{x} \tag{6.1}$$

Table 9 Error parameters of x-axis accelerometer.

Parameter	x-axis accelerometer
Velocity random walk (N) (mg/√Hz)	0.4924
Bias Instability (B)(m/s^2)	0.0037
Rate Random Walk (K) (m/s/h$^{3/2}$)	86.4
Time constant	24

Same process is applied for y-axis accelerometer and the fitted curve is demonstrated in Figure 65.

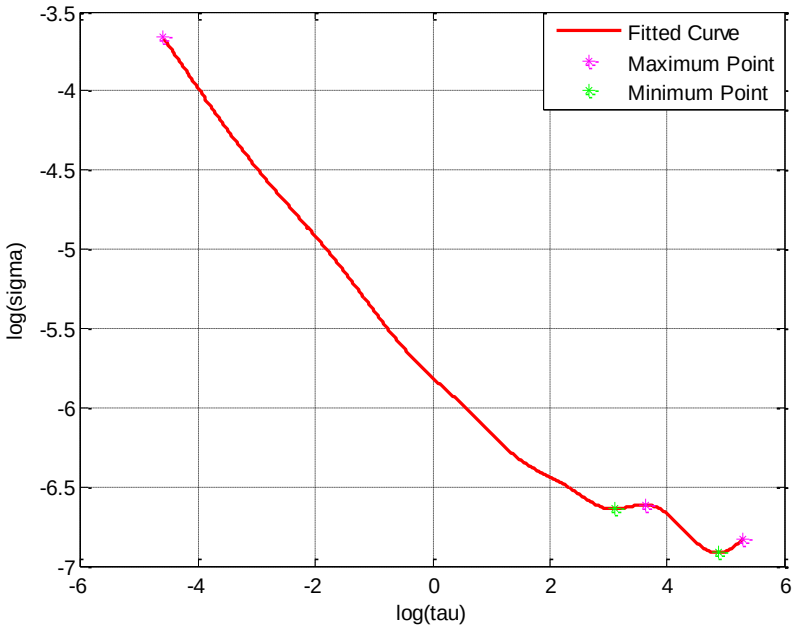

Figure 65 Minimum and maximum points of the fitted curve for y-axis accelerometer.

There are two local minimum points in the Figure 65. First one is due to the bias instability, but it is ignored, because we use the threshold approximation to estimate the time constant value. Second minimum point states starting time of rate random walk. Time constant of the bias instability and rate random walk is 21 s and 133 s, respectively. Relevant membership functions are shown in Figure 66 and error parameters are given in the Table 10.

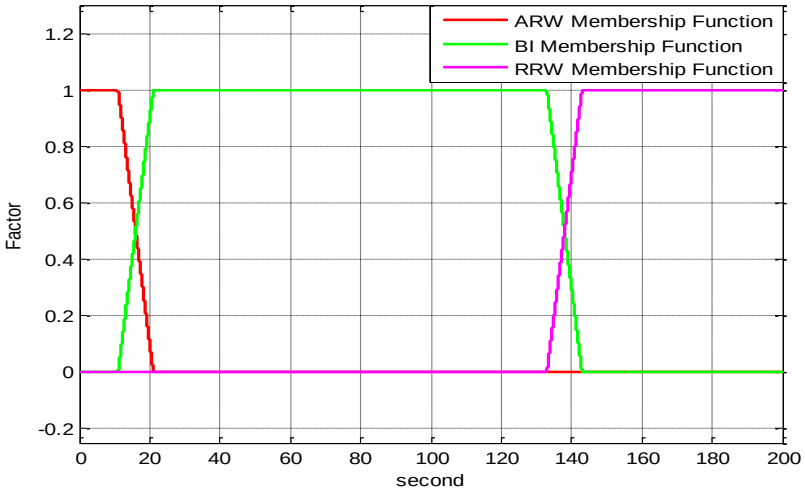

Figure 66 Membership functions for y-axis accelerometer.

Table 10 Error parameters of y-axis accelerometer

Parameter	y-axis accelerometer
Velocity random walk (N) (mg/√Hz)	0.3051
Bias Instability (B)(m/s^2)	0.0017
Rate Random Walk (K) (m/s/h$^{3/2}$)	21.6
Time constant (s)	21

Fitted Allan deviation curve is shown in Figure 67 for z-axis accelerometer.

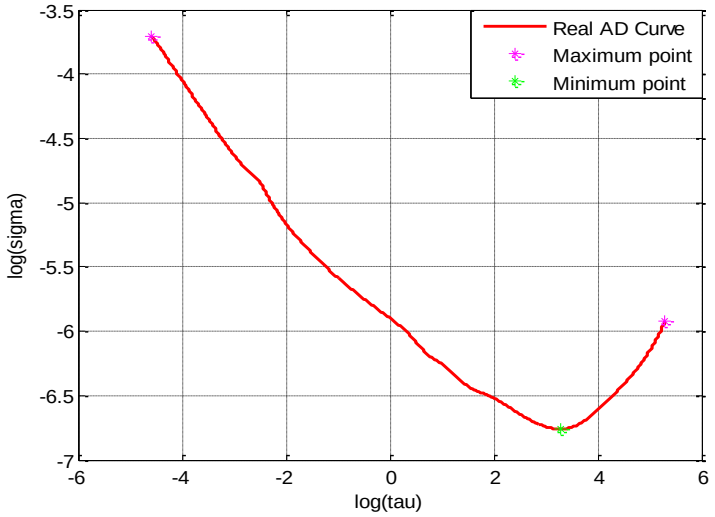

Figure 67 Maximum and minimum points for fitted curve of z-axis accelerometer.

z-axis accelerometer has a local minimum at 29 s. Slope investigation gives that correlation time of bias instability is 23 s. We can form the membership functions for z-axis accelerometer. Estimation results are given in Table 11.

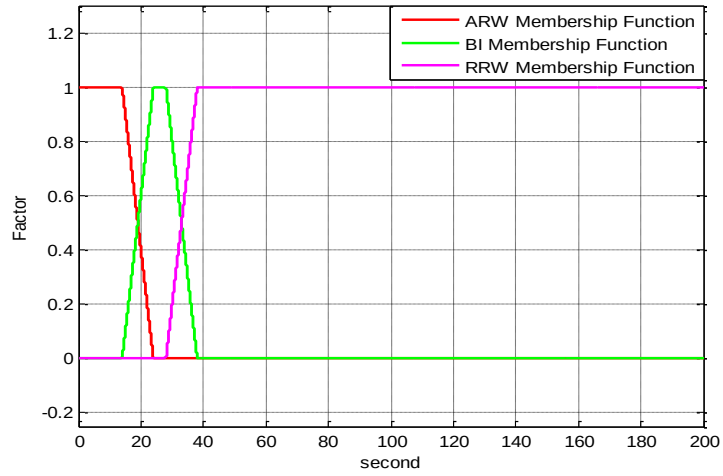

Figure 68 Membership functions for z-axis accelerometer.

Table 11 Error parameters for z-axis accelerometer.

Parameter	z-axis accelerometer
Velocity random walk (N) (mg/√Hz)	0.27
Bias Instability (B)(m/s^2)	0.0019
Rate Random Walk (K) (m/s/h$^{3/2}$)	66.3
Time constant (s)	23

x-axis gyroscope of the MEMS IMU 1 is inspected by the proposed method. Firstly, fitted Allan deviation curve is given in Figure 69.

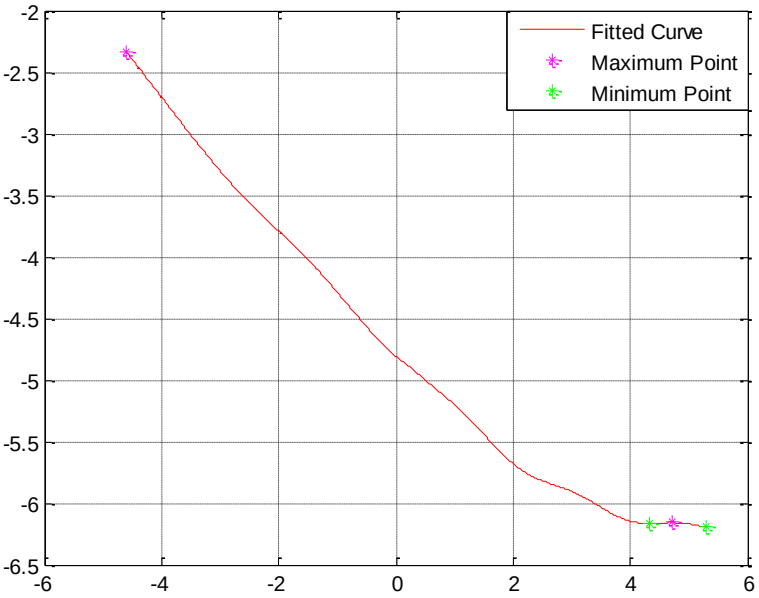

Figure 69 Fitted function for x-axis gyroscope.

There are two minimum points in this figure, but these are not the indication of the rate random walk because these are only due to the deviation of the bias instability. We can extract the correlation time of bias instability with our threshold method.

Correlation time of bias instability is 57 s and membership functions are shown in Figure 70 for x-axis gyroscope. Results are given in the Table 12.

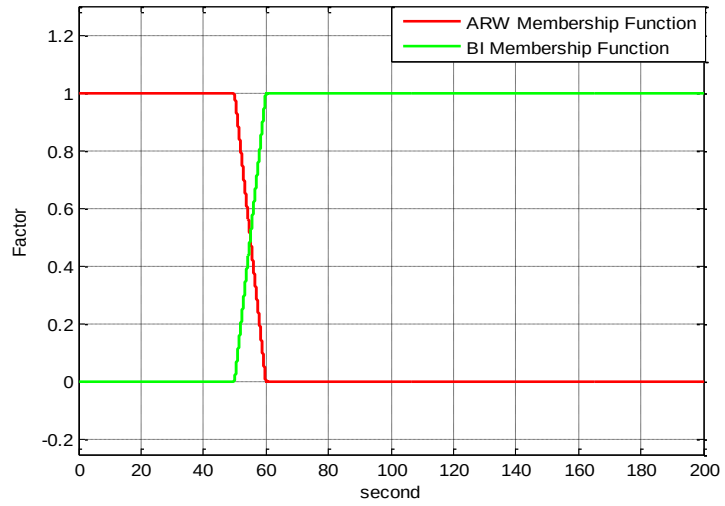

Figure 70 Membership functions for x-axis gyroscope of the MEMS IMU 1.

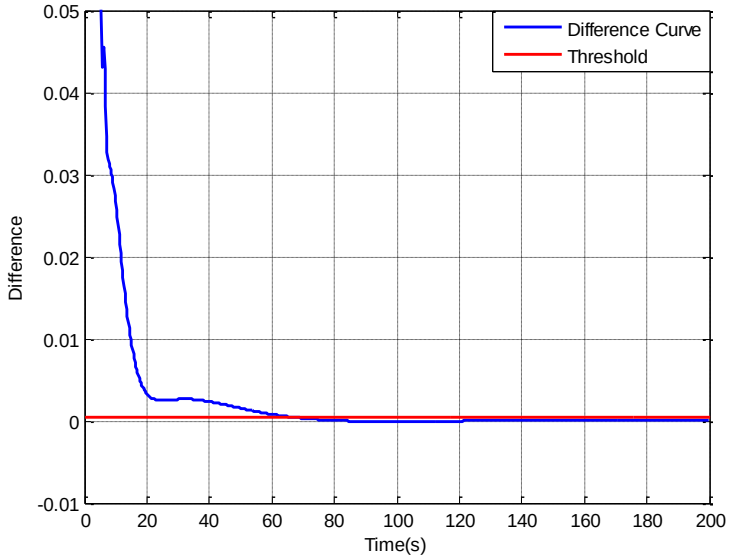

Figure 71 Applying threshold value to x-axis gyroscope of the MEMS IMU 1.

Table 12 Error parameters of x-axis gyroscope.

Parameter	x-axis gyroscope
Angle random walk (N) (deg/√h)	0.552
Bias Instability (B)(deg/h)	11.52
Time constant (s)	54

Fitted curve for y-axis gyroscope is given in Figure 72 .

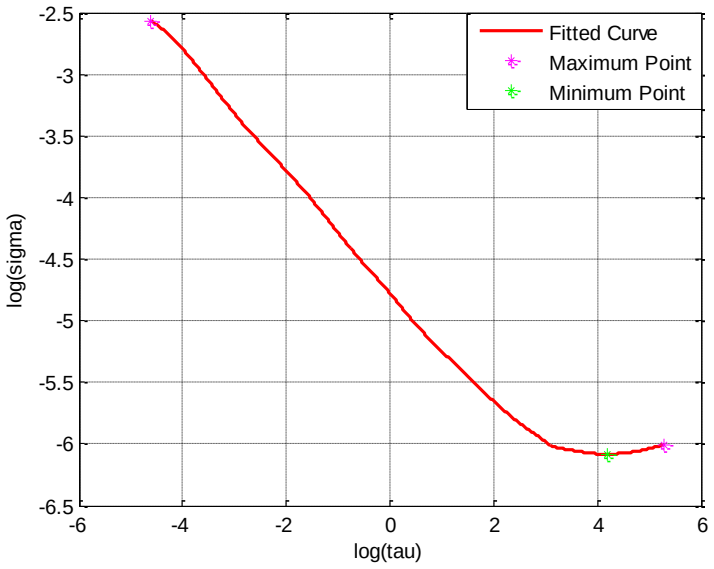

Figure 72 Fitted curve, maximum and minimum points for y-axis gyroscope.

This curve also has the minimum point but it is not the starting time of rate random walk, therefore, rate random walk equals to zero. Correlation time of bias instability is nearly 30 s according to threshold method. Determined error parameters are given in the Table 13.

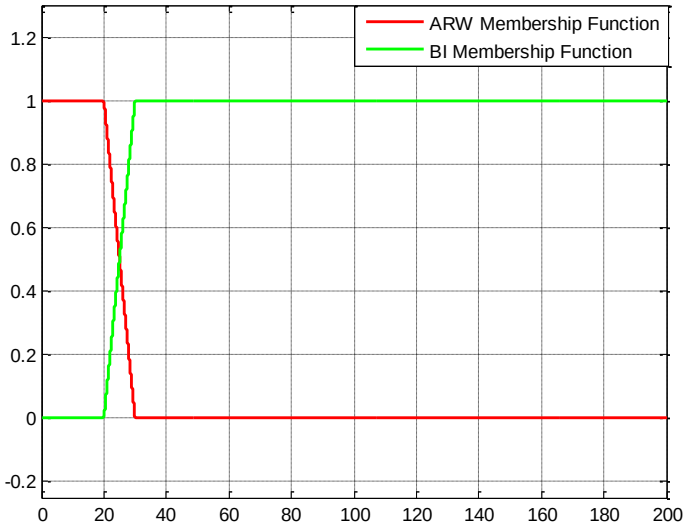

Figure 73 Membership functions for the y-axis gyroscope of the MEMS IMU 1.

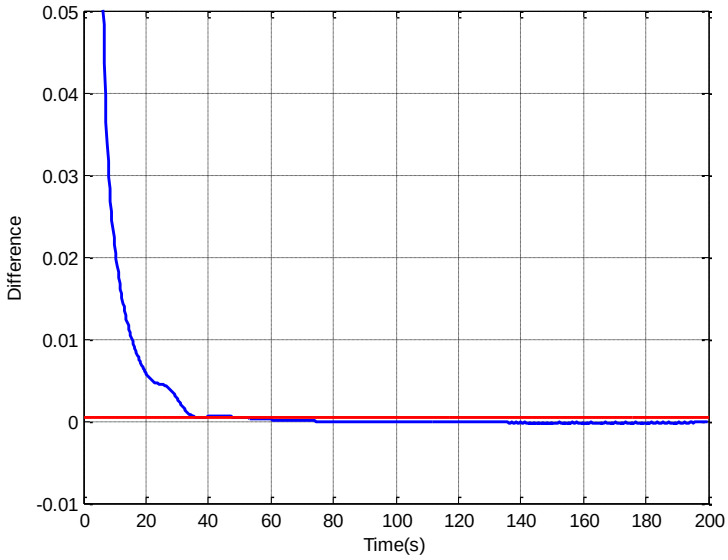

Figure 74 Applying threshold value to y-axis gyroscope of the MEMS IMU 1.

Table 13 Error parameters for the y-axis gyroscope.

Parameter	y-axis gyroscope
Angle random walk (N) (deg/√h)	0.522
Bias Instability (B)(deg/h)	12.96
Time constant (s)	30

Fitted curve of z-axis gyroscope is shown in Figure 75.

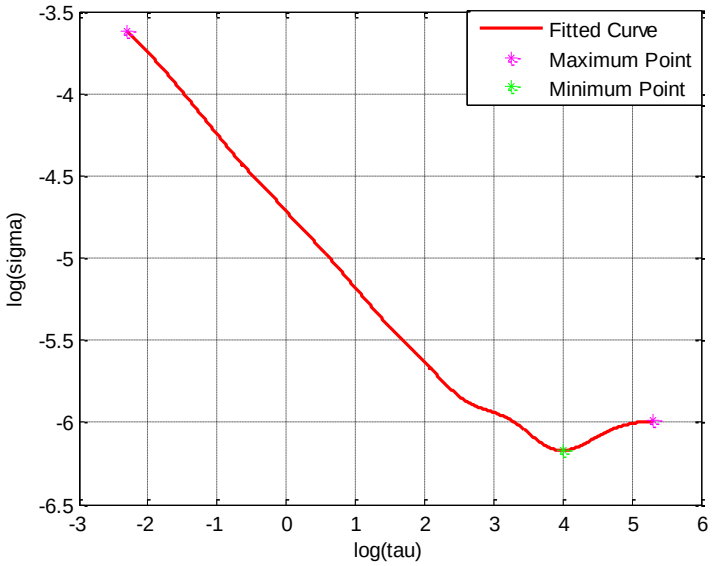

Figure 75 Fitted curve for z-axis gyroscope.

There is a minimum point in Figure 75, but slope of the curve becomes zero at the end of the curve. Therefore, rate random walk is not a dominant error term in this region. It is also considered as the bias instability. Minimum point in the Figure 75 indicates that this point is the correlation time of bias instability. Membership functions are given in the following figure.

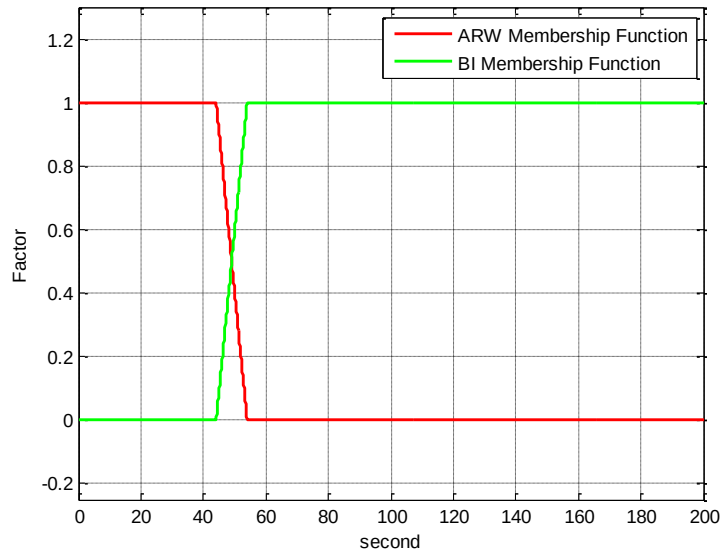

Figure 76 Membership functions for z-axis gyroscope of MEMS-IMU 1.

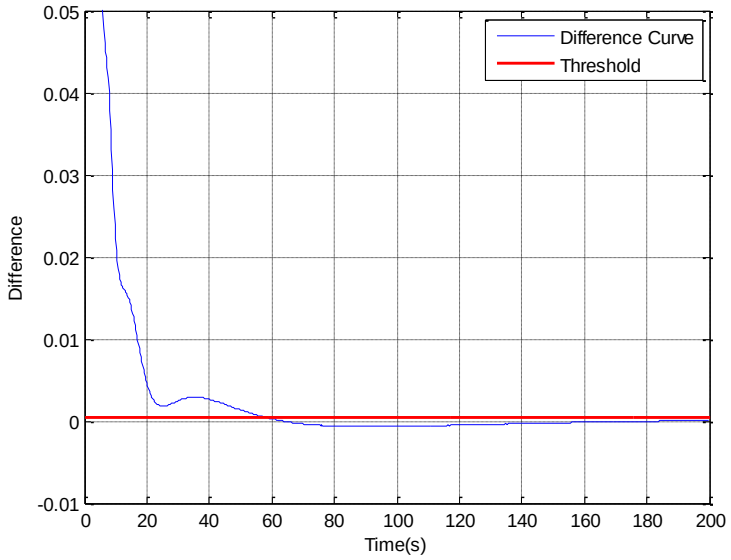

Figure 77 Applying threshold value to z-axis gyroscope of the MEMS IMU 1.

Table 14 Error parameters of z-axis gyroscope.

Parameters	z-axis gyroscope
Angle random walk (N) (deg/√h)	0.552
Bias Instability (B)(deg/h)	12.96
Time constant (s)	50

To sum up, we estimated all of the sensor errors for the MEMS IMU 1. We will generate random and deterministic errors and compare with the real Allan variance curve.

6.1.3 Noise Generation for the MEMS IMU 1

IMU random error parameters are shown in Table 7 and Table 8 for line method and from Table 9 to Table 14 for the proposed method. These parameters are used in IMU error modeling. Deterministic errors are modeled with their 1σ value, for example if bias repeatability value is 10 mg bias can be modeled by random generator with variance of 10 mg. In this example, maximum expected IMU bias is ±30 mg (3σ value). IMU modeling is based on white noise process, Gauss Markov process and random walk process.

Low-pass filter is employed by the IMU model because all random error generators produce wide-band errors hence; it causes differences between real data and simulated data. Accurate modeling of the filter is an important problem when true parameters of the low-pass filter are unknown.

Parameters of x-axis accelerometer are taken from Table 7, Table 9 to Table 10. According to Table 7, resulting random error generator equations can be given for x-axis accelerometer as,

$$
\begin{gathered}
dt = 0.001s \\
0.4899 \frac{mg}{\sqrt{Hz}} \text{x} 9.7987 \frac{m}{s^2} \text{x} \sqrt{1000\,Hz} = 0.1518 \frac{m}{s^2} \\
y_{vrw}[k] = 0.1518 \frac{m}{s^2} w[k] \\
w[k] \sim N(0,1)
\end{gathered}
\tag{6.2}
$$

As stated below, 1σ value of white noise is 0.1512 m/s^2, and correlated noise is modeled by Gauss-Markov process and the parameter of Gauss-Markov process is demonstrated by,

$$
\begin{gathered}
x[k+1] = e^{-\frac{0.001s}{20s}} x[k] + 0.0031 \frac{m}{s^2} \sqrt{1 - e^{-2\frac{0.001s}{20s}}}\, w[k] \\
w[k] \sim N(0,1)
\end{gathered}
\tag{6.3}
$$

According to Equation (5.28), rate random walk is expressed as follows,

$$
\begin{gathered}
x[k+1] = x[k] + 0.0003 \frac{m}{s^2} w[k] \\
y[k] = x[k] \\
w[k] \sim N(0,1)
\end{gathered}
\tag{6.4}
$$

All sensors are modeled with the same structures but different parameters (i.e., the line method and the proposed method) and comparisons of simulated data and real data are given in Figure 78 to Figure 80.

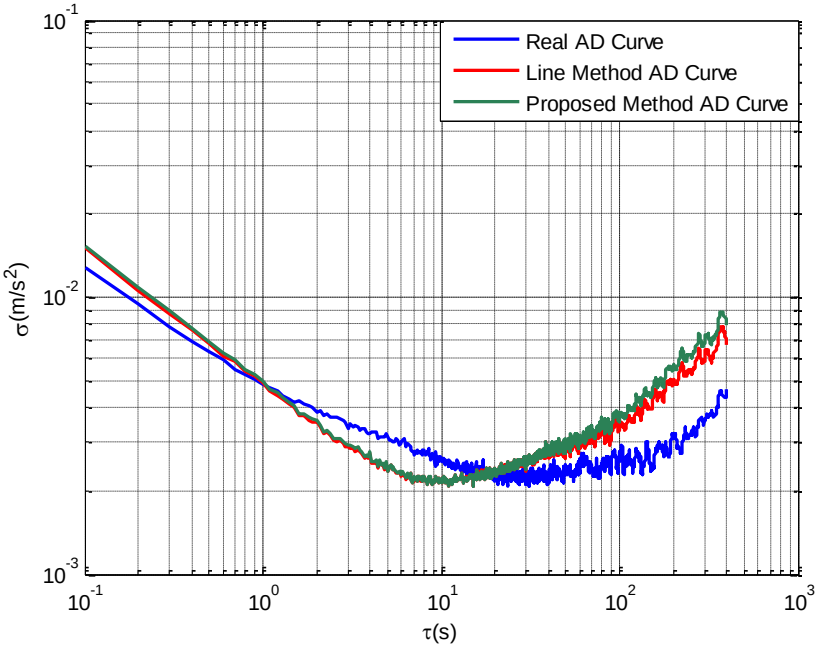

Figure 78 Comparison of Allan deviation curve of real data and simulated data for x-axis accelerometer.

Allan deviation curve of simulated data somehow match with Allan deviation curve of real data but bias instability cause main difference between two curves. Additionally, it is supposed that real Allan deviation curve does not represent real sensor behavior due to the temperature. Differences between exact value and simulated error are not huge.

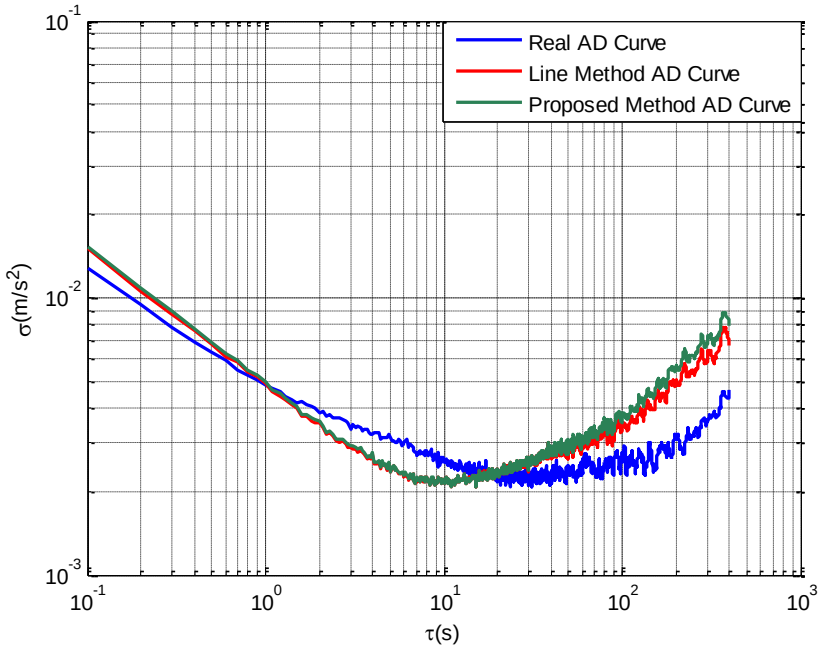

Figure 79 Allan deviation curves of real data and simulated data for y-axis accelerometer of the MEMS IMU 1.

The main problem of this IMU is both temperature and correlated noise are around τ = 100 s which cannot be modeled easily. Temperature causes deviations from true error characteristic and causes some errors on estimated error parameters. Therefore, differences occur between real data curve and the simulated data curve.

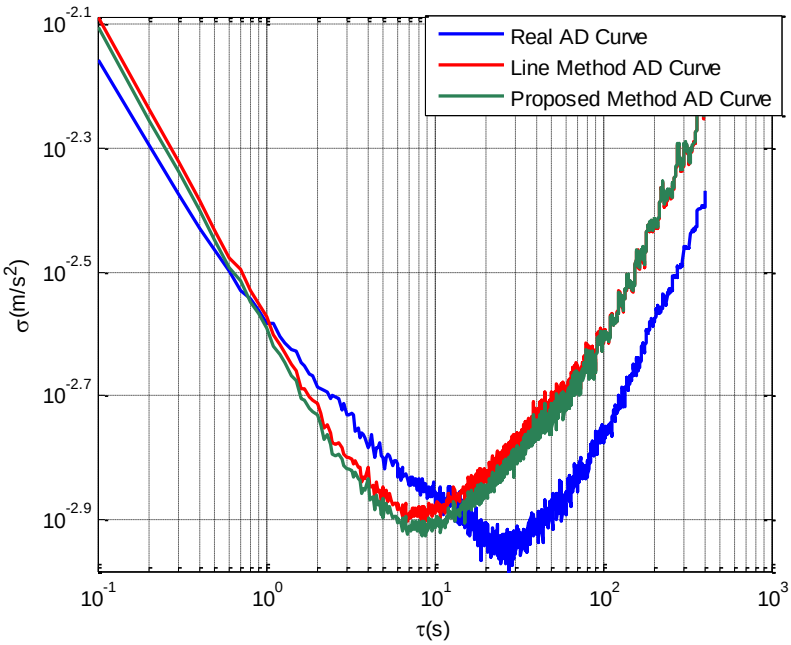

Figure 80 Allan deviation curves of real data and simulated data for z-axis accelerometer of the MEMS IMU 1.

Main problem in Figure 80 is small time scale of bias instability error. Summations of all errors cause deviation from real Allan deviation curve. For instance, summation of bias instability and velocity random walk increases the noise level at $\tau<10$ s region. Additionally, summation of rate random walk and bias instability causes variation of Allan deviation curve.

Rate random walk is not included the gyroscope models because slope of +1/2 region cannot be obtained from the Allan deviation curves. Yet, other errors have the same modeling structures with the accelerometers. Error parameters are taken from Table 8, Table 12, Table 13 and Table 14. Comparisons are shown in Figure 81 to Figure 83.

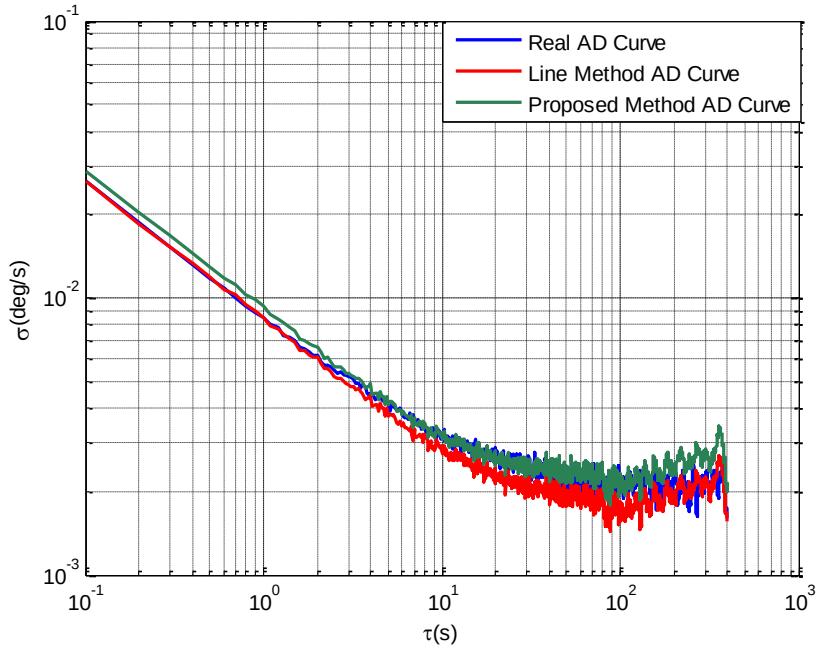

Figure 81 Allan deviation curves of real data and simulated data for x-axis gyroscope of the MEMS IMU 1.

Curves are slightly different from each other; it means that the suggested error model is enough for modeling this gyroscope. Nevertheless, the proposed method estimates are more accurately than the line method.

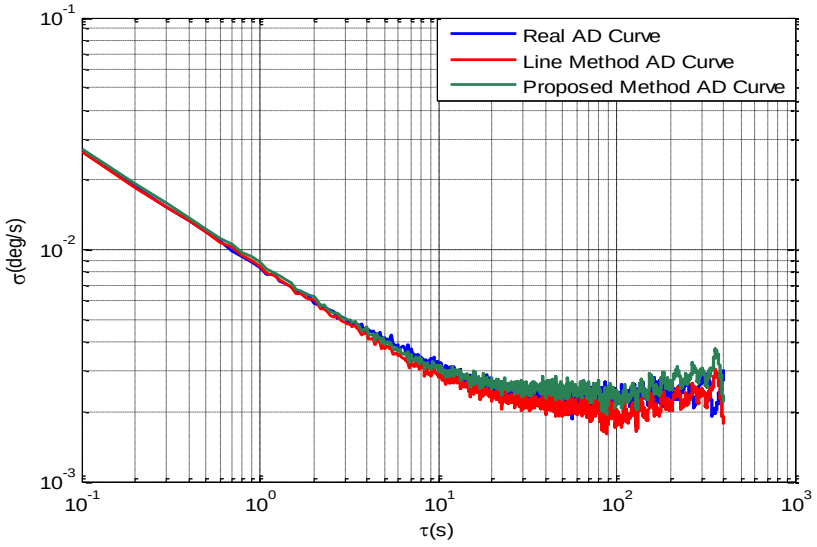

Figure 82 Allan deviation curves of real data and simulated data for y-axis gyroscope of the MEMS IMU 1.

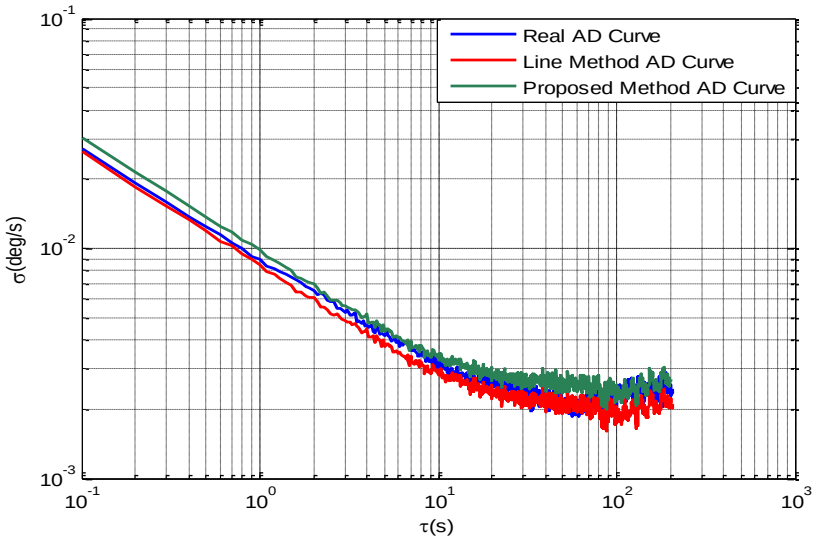

Figure 83 Allan deviation curves of real data and simulated data for z-axis gyroscope of the MEMS IMU 1.

Error identification techniques find different results for each error term. Sometimes slightly different results are obtained even if temperature dependency of bias and scale factor errors are modeled. Yet, residuals of temperature dependent part of deterministic errors still affect the output of the sensor.

6.1.4 Estimation of Sensor Errors with Traditional Line Method for the MEMS IMU 2

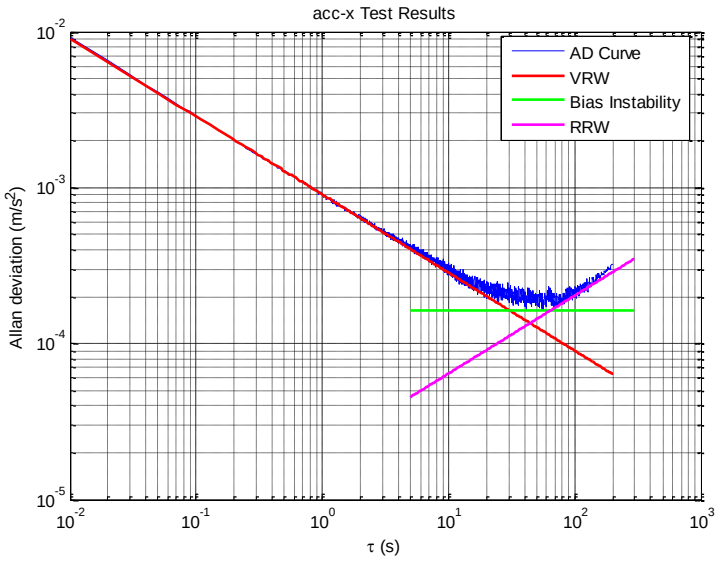

Figure 84 Allan deviation curve of x-axis accelerometer of the MEMS IMU 2.

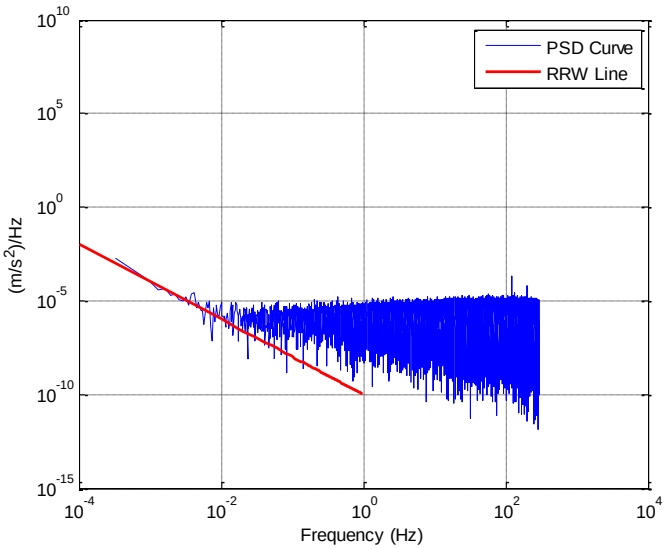

Figure 85 PSD curve of x-axis accelerometer of the MEMS IMU 2.

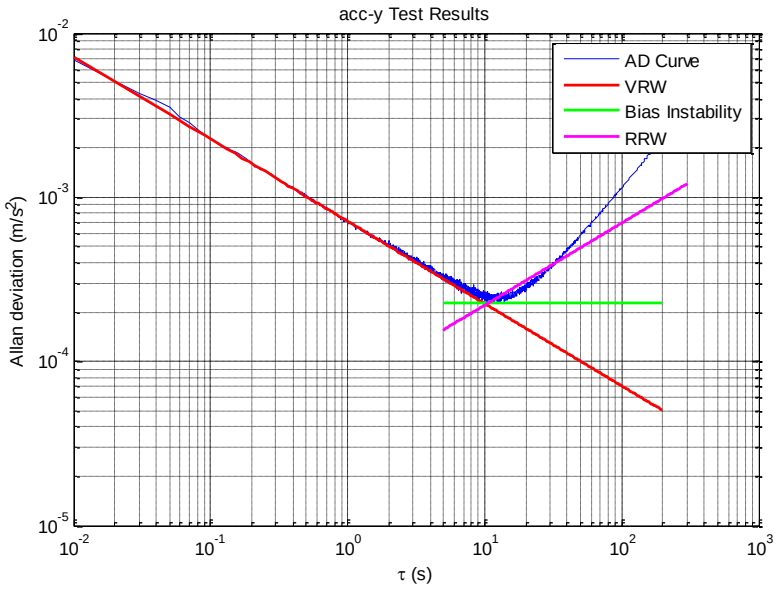

Figure 86 Allan deviation curve of y-axis accelerometer of the MEMS IMU 2.

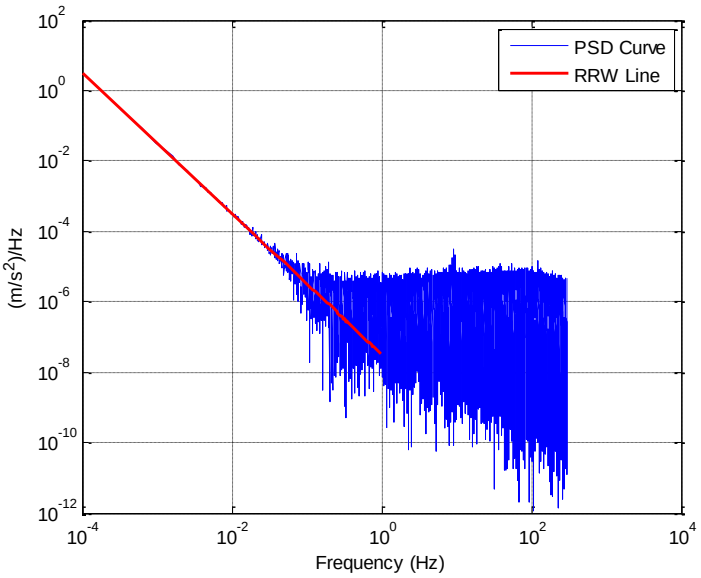

Figure 87 PSD curve of y-axis accelerometer of the MEMS IMU 2.

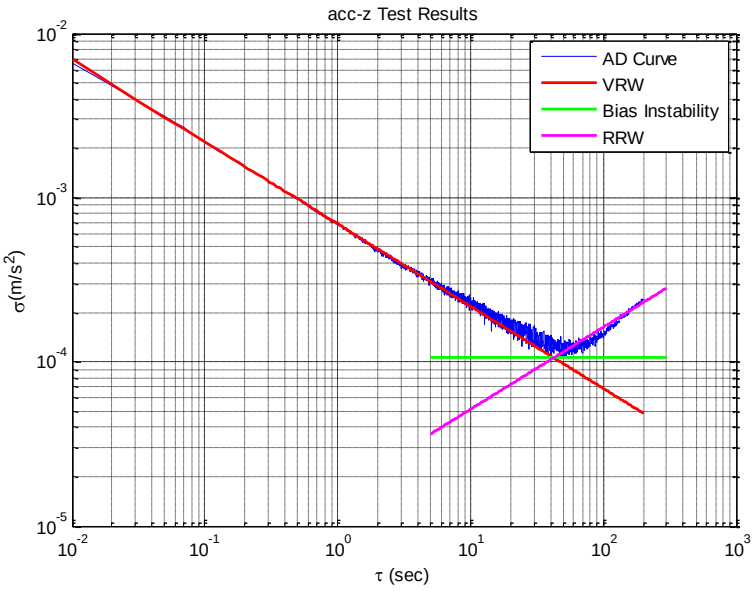

Figure 88 Allan deviation curve of z-axis accelerometer of the MEMS IMU 2.

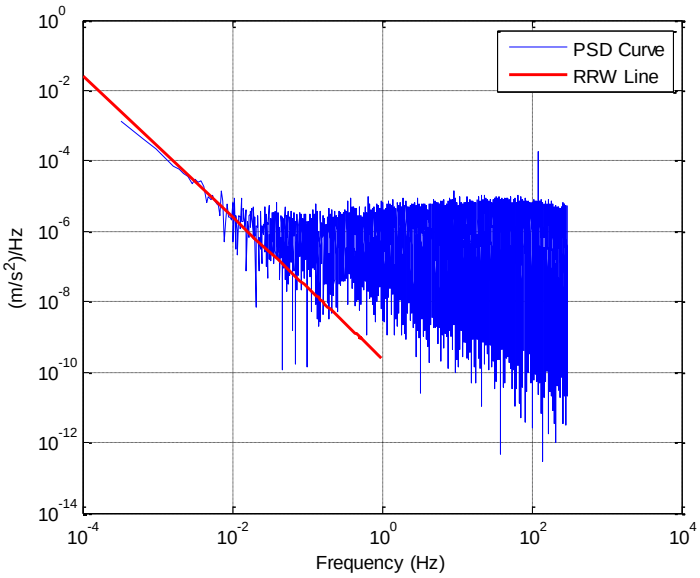

Figure 89 PSD curve of z-axis accelerometer of the MEMS IMU 2.

Table 15 Identified accelerometer error parameters of the MEMS IMU 2.

Accelerometer	**Velocity Random Walk(mg/√Hz)**	**Rate Random Walk(m/s/h$^{3/2}$)**
x-axis	0.0925	8.64
y-axis	0.0729	4.96
z-axis	0.0706	5.83

Bias instability is not modeled because it does not have any effect on the accelerometer output as shown in Figure 84 to Figure 88. We decide which error affects the output of sensor according to the location of the lines. PSD method is useful in these kinds of situations.

Figure 85 shows that dominant error terms are rate random walk and angle random walk for x-axis accelerometer sensor. The same result is also valid for other accelerometers. Therefore, if one cannot decide about dominant noise terms, PSD function gives important outcomes about noise characters.

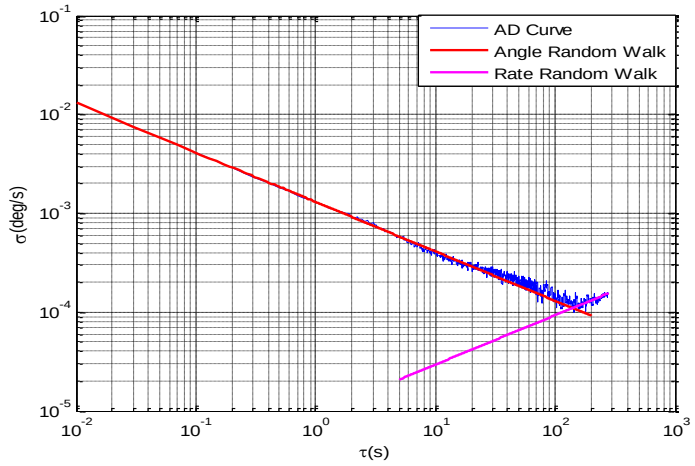

Figure 90 Allan deviation curve of x-axis gyroscope of the MEMS IMU 2.

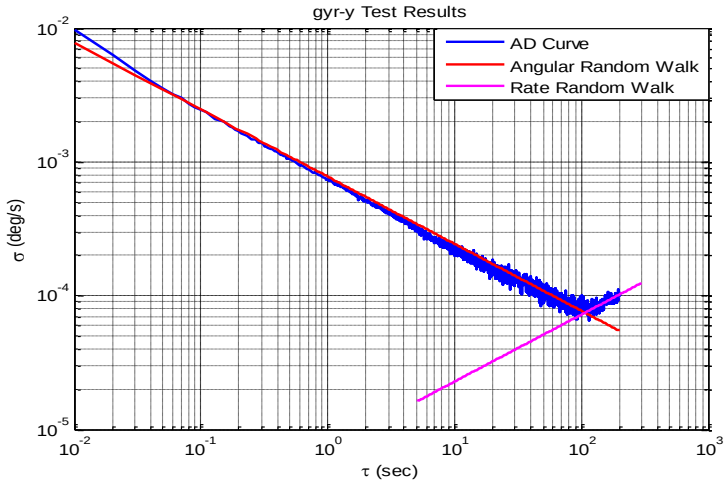

Figure 91 Allan deviation curve of y-axis gyroscope of the MEMS IMU 2.

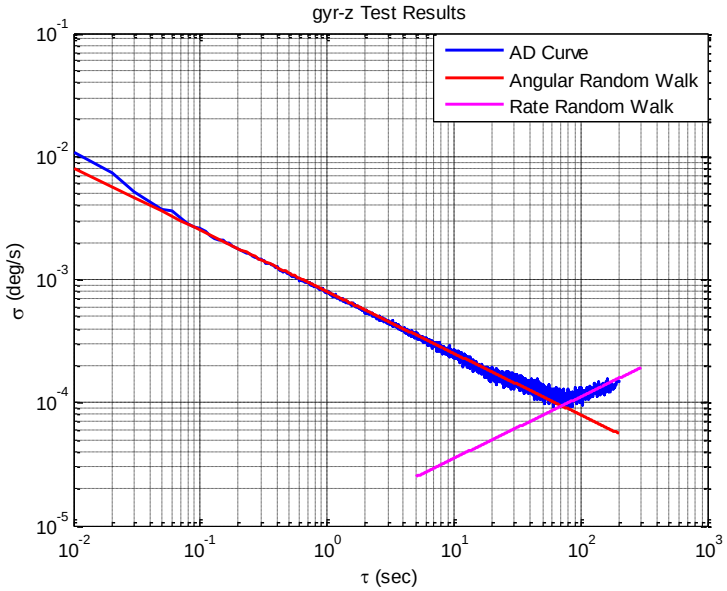

Figure 92 Allan deviation curve of z-axis gyroscope of the MEMS IMU 2.

As the lines indicated, gyroscopes generally have only angle random walk and rate random walk on the output of the sensor. Moreover, we cannot draw a unique line for bias instability and rate random walk. For example, Allan deviation results start to oscillate at higher tau values. Therefore, it is very hard to draw a specific line on Allan deviation curve.

Table 16 Identified gyroscope error parameters of the MEMS IMU 2.

Gyroscope	**Angle Random Walk(deg/√h)**	**Rate Random Walk (deg/h/√s)**
x-axis	0.078	0.0583
y-axis	0.0448	0.043
z-axis	0.048	0.0677

6.1.5 Estimation of Sensor Errors with Proposed Method for the MEMS IMU 2

The same procedures with the MEMS IMU 1, are treated to investigate Allan deviation curves of the MEMS IMU 2. Firstly, a curve is fitted to Allan deviation curve and then we extract the correlation times of specific error terms.

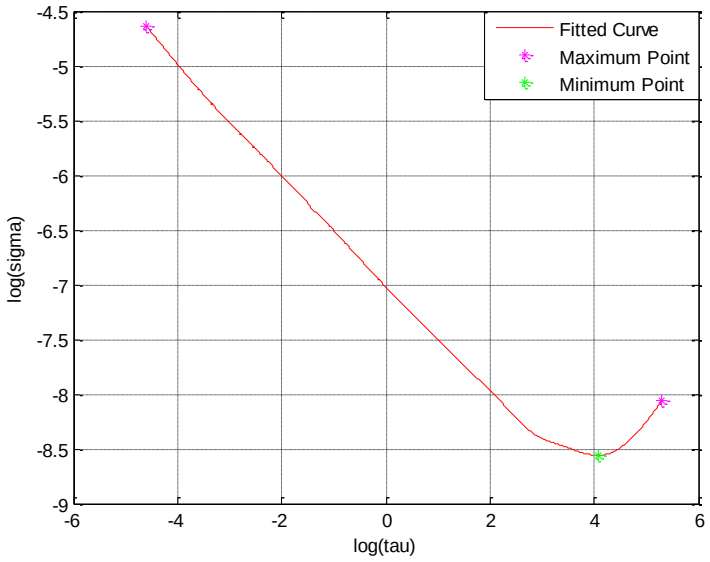

Figure 93 Fitted curve of x-axis accelerometer of the MEMS IMU 2.

Figure 93 implies that starting time of the rate random walk is 58 s. Additionally, threshold method finds 55 s for the correlation time of bias instability. This condition occurs when the data is affected by rate random walk and velocity random walk. It can be supposed that bias instability parameter can be identified between τ = 55 s and τ = 58 s, but modeling bias instability causes unexpected behavior of Allan deviation curve. Therefore, this data is affected by rate random walk and velocity random walk.

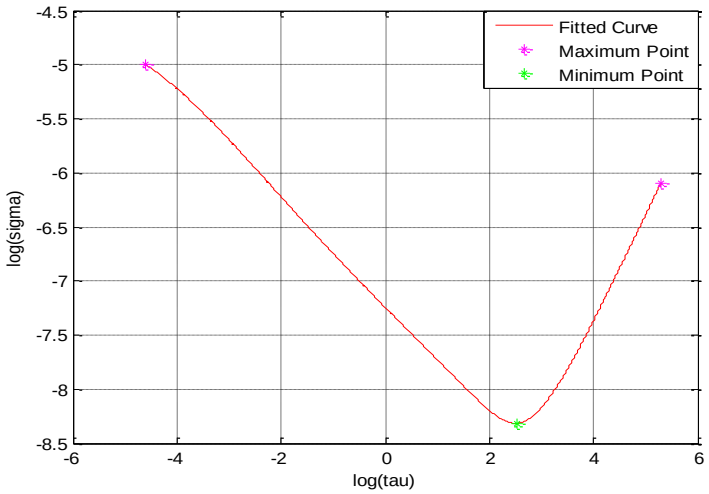

Figure 94 Fitted curve of y-axis accelerometer of the MEMS IMU 2.

Figure 94 shows that the starting time of the rate random walk is 12 s. Bias instability does not correlate the data, because both threshold method and local minimum point approach finds same time value (τ = 12 s). This data is certainly affected by velocity random walk and rate random walk.

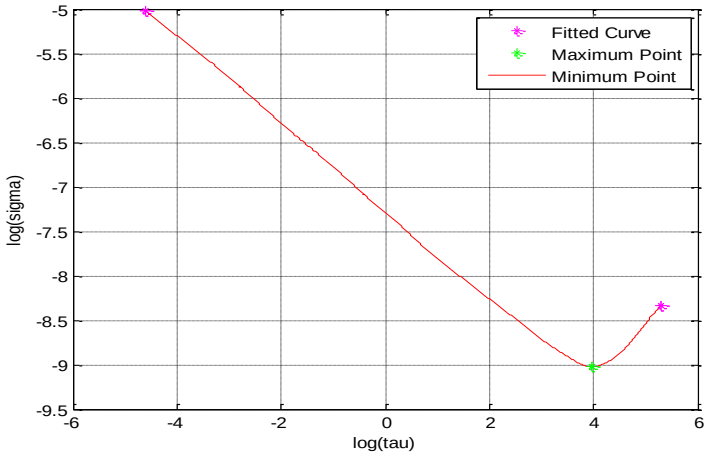

Figure 95 Fitted curve of z-axis accelerometer of the MEMS IMU 2.

According to Figure 95, z-axis accelerometer is also affected by the velocity random walk and rate random walk. It has one minimum point and the threshold method finds the same point for slope of zero regions. Time index of minimum point is 52 s. Bias instability can be considered as the corresponding value of this minimum point. Yet, both bias instability and velocity random walk have the same time index. Additionally, fitted curve always increases after 52 s. To sum up, this data contains velocity random walk and rate random walk.

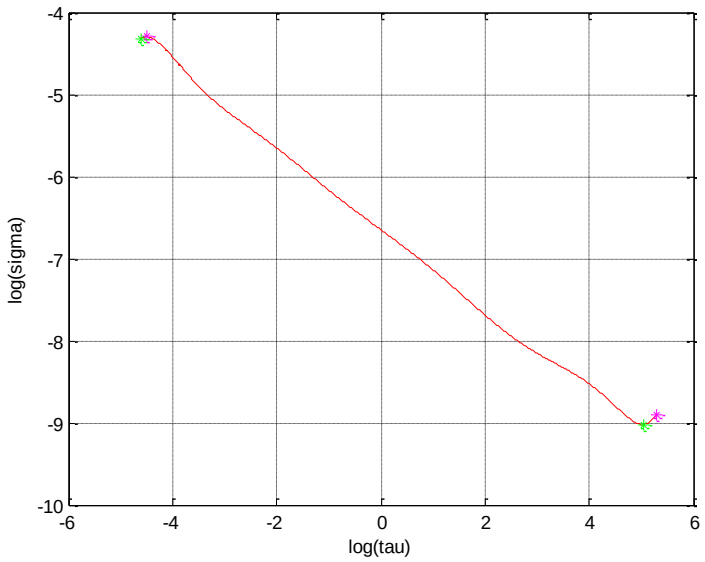

Figure 96 Fitted curve of x-axis gyroscope of the MEMS IMU 2.

Starting time of rate random walk is 155 s and the correlation time of bias instability is 152 s according to threshold method. Bias instability is not available in this time range. Thus, angle random walk and rate random walk are taken into account.

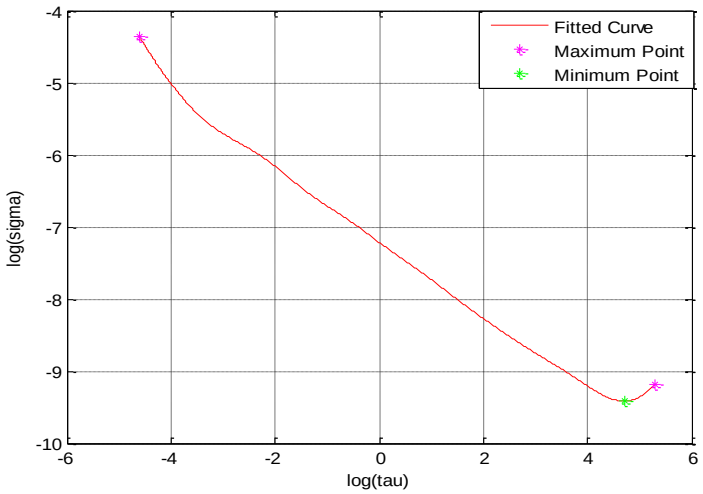

Figure 97 Fitted curve of y-axis gyroscope of the MEMS IMU 2.

Starting time of the rate random walk noise is 110 s. Additionally, threshold method finds that the correlation time of bias instability is 107 s. Therefore, bias instability is supposed as the dominant error term with only a very short time range.

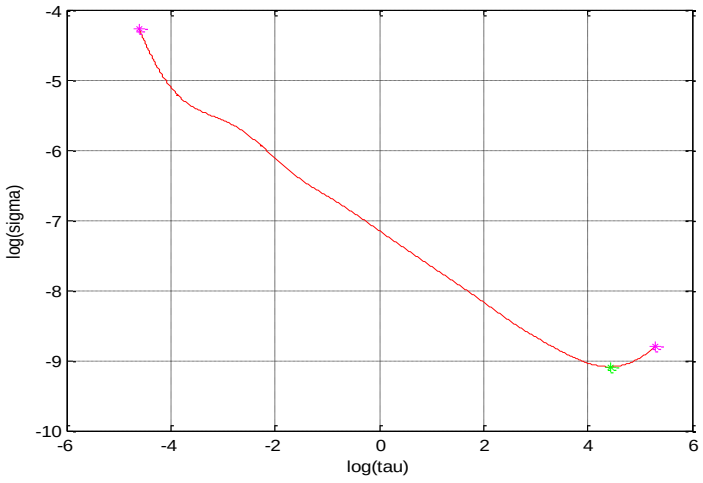

Figure 98 Fitted curve of z-axis gyroscope of the MEMS IMU 2.

In Figure 98, minimum point occurs at 51 s and flat region starts 50 s. Therefore, bias instability is not included in models, rate random walk and angle random walk errors are modeled. Resultant membership functions are given in Figure 99 and Figure 100.

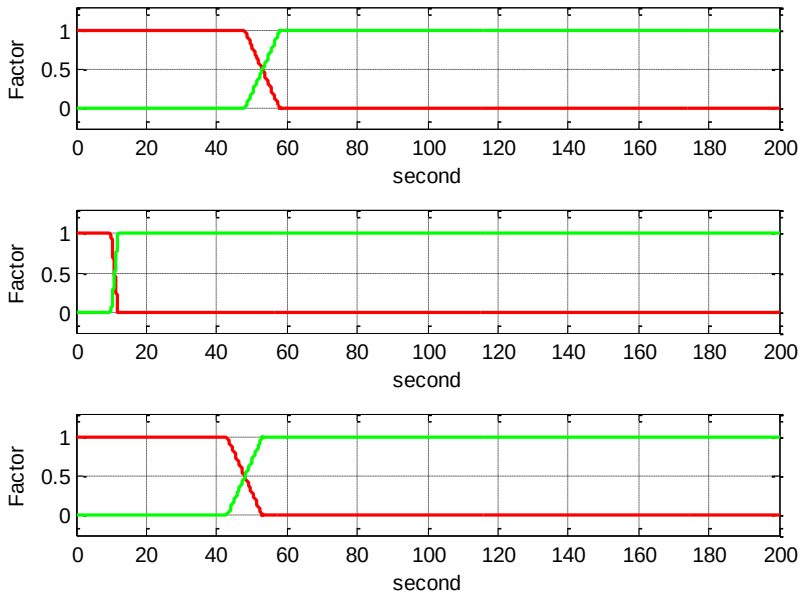

Figure 99 Membership functions of x, y, z axes accelerometers respectively (up to bottom). Red line indicates membership function of angle random walk, green line states membership function of rate random walk.

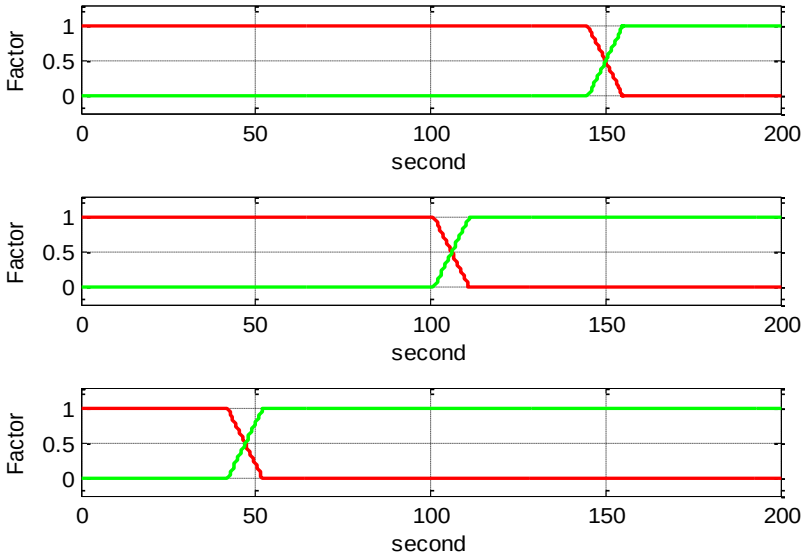

Figure 100 Membership functions of x, y, z axes gyroscopes respectively (up to bottom). Red line indicates membership function of angle random walk, green line states membership function of rate random walk.

Error parameters are estimated by the least-square estimation and are shown in Table 17 and Table 18.

Table 17 Accelerometer error parameters with proposed method.

Accelerometers	**Velocity Random Walk(mg/√Hz)**	**Rate Random Walk (m/s/h$^{3/2}$)**
x-axis	0.0956	8.1
y-axis	0.0741	5.08
z-axis	0.0710	5.96

Table 18 Gyroscope error parameters with proposed method.

Gyroscopes	Angle Random Walk(deg/√h)	Rate Random Walk (deg/h/√s)
x-axis	0.078	0.0590
y-axis	0.0466	0.0446
z-axis	0.0419	0.0691

Angle random walk on x-axis gyroscope is higher than other axes because measurement range is two times higher than other axes. Inertial sensors are modeled with estimated parameters and comparisons are made between real Allan deviation curve and Allan deviation curve of the simulated data.

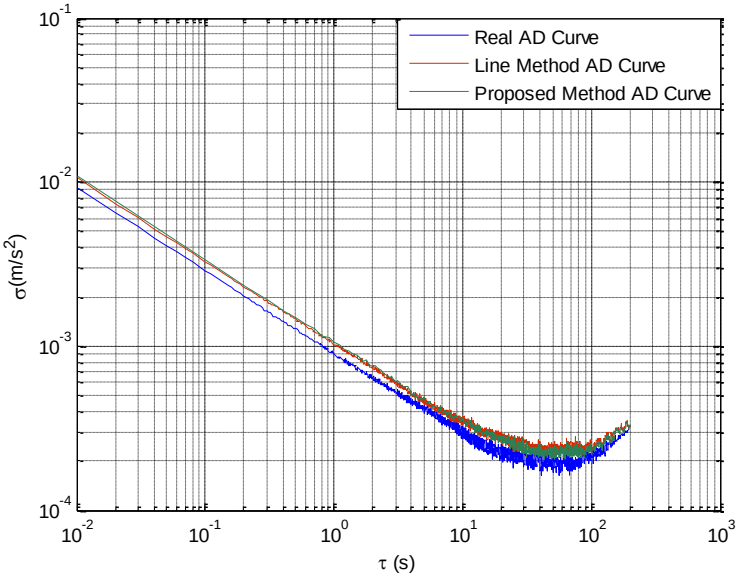

Figure 101 x-axis accelerometer comparison result.

Parameters of the proposed method are slightly better than that of the line method, but there are still some differences between real Allan deviation curve and the

proposed method, especially in the velocity random walk region. These differences sometimes occur due to the filter or isolator parameters.

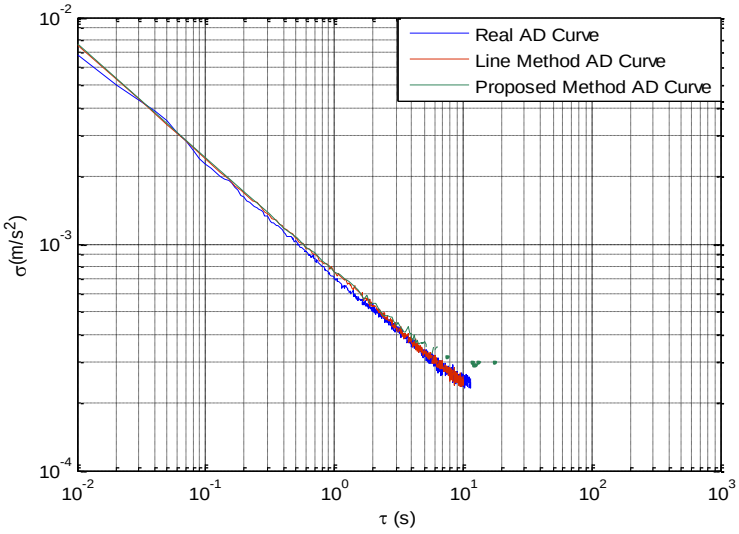

Figure 102 y-axis accelerometer comparison result.

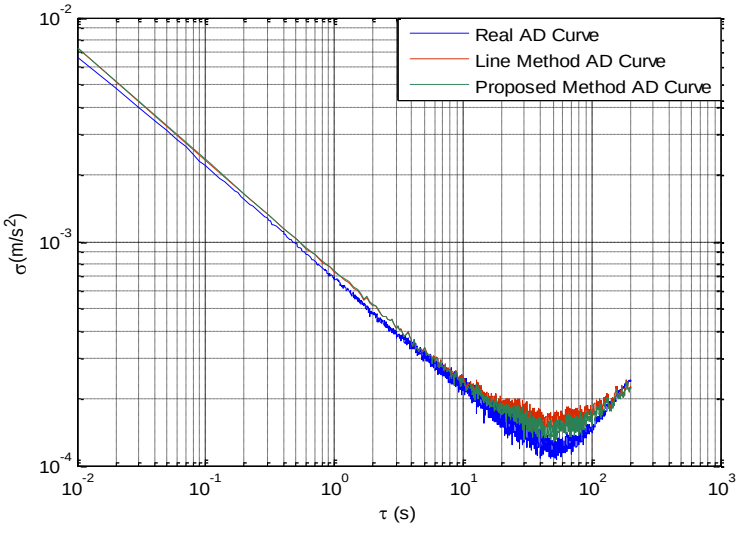

Figure 103 z-axis accelerometer comparison result.

Figure 102 and Figure 107 shows that the proposed method produces more accurate results than the traditional line method. Additionally, three curves reach the same value at the end of the curve.

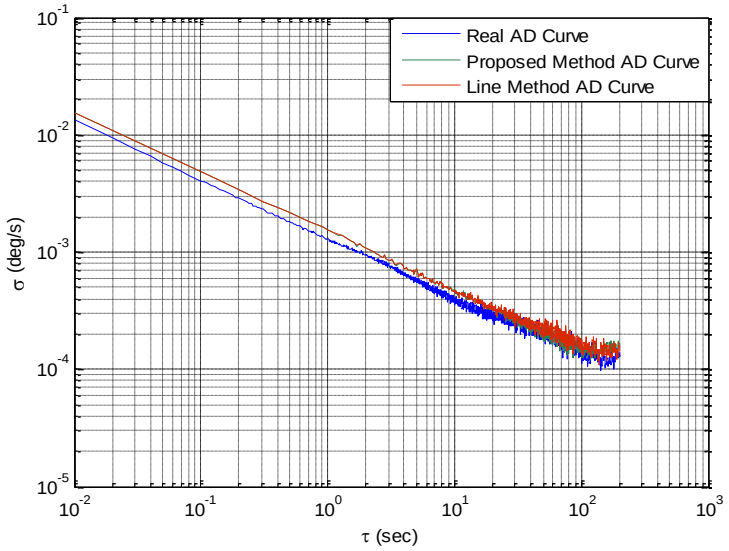

Figure 104 x-axis gyroscope comparison result.

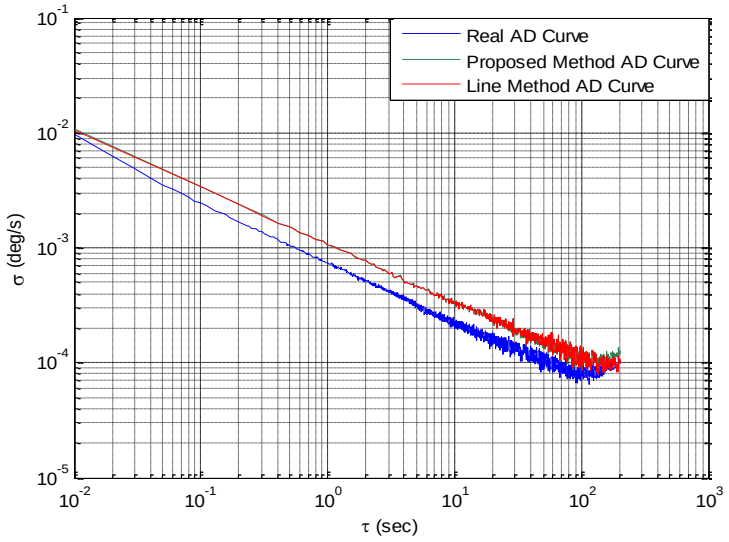

Figure 105 y-axis gyroscope comparison result.

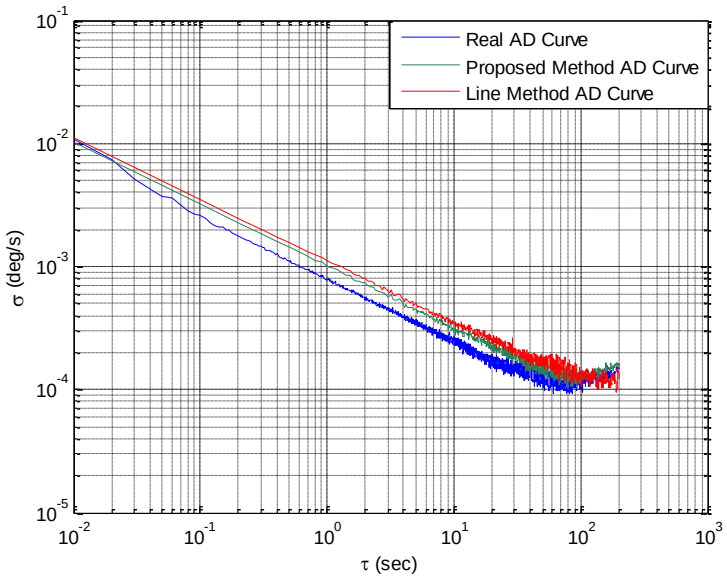

Figure 106 z-axis gyroscope comparison result.

Gyroscope results show two error identification results are enough to produce nearly the same results with real Alan deviation curve, but small dissimilarities are observed from the figures. Yet, parameters of the line method cause deviation from the real Allan deviation curve as shown in Figure 106.

6.2 Modeling Quartz Sensor

Quartz sensors use quartz material to measure physical quantity. Therefore, magnitudes of random error parameters are very low for quartz sensor and repeatability values of deterministic errors are better than MEMS sensors. These sensors are in the tactical grade class. For example, bias repeatability value of this sensor is 1 mg (1σ-value). This is twenty times better than control grade accelerometers. Deterministic error parameters are demonstrated in Table 19. Deterministic errors are modeled with zero mean and known variance. Random error parameters are estimated by both the line method and the proposed method, but

detailed analysis of the proposed method is not given in this section. PSD analysis shows that bias instability and angle/velocity random walk is dominant error terms for quartz sensor. Allan deviation results are shown in Figure 107 to Figure 112.

Table 19 Deterministic error parameters of the quartz sensor.

Sensor Type	**Error Parameter**	**Magnitude**
Accelerometer	Scale Factor (3σ) ppm	600
	Bias (3σ) (mg)	3
	Misalignment (3σ) mrad	5.6
Gyroscope	Scale Factor (3σ) ppm	600
	Bias (3σ) (deg/h)	3
	Misalignment (3σ) mrad	5.6

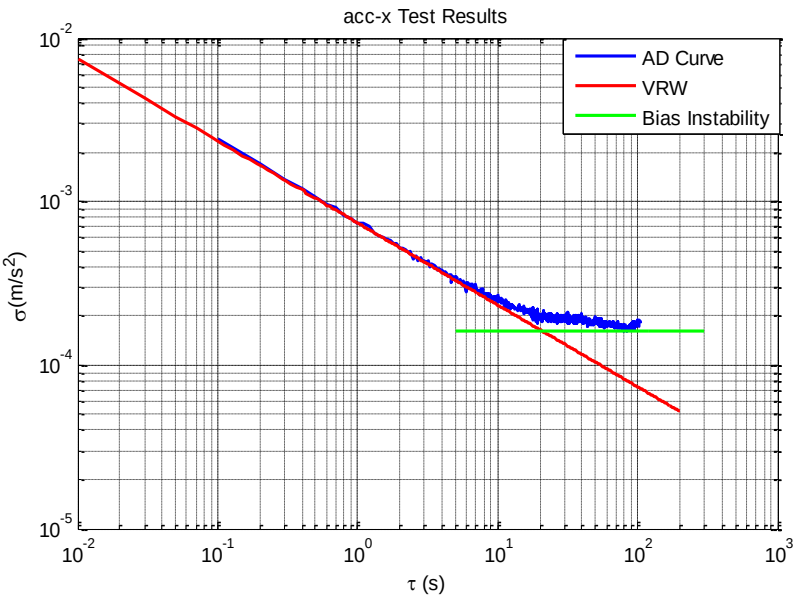

Figure 107 Allan deviation curve of x-axis accelerometer of the quartz IMU.

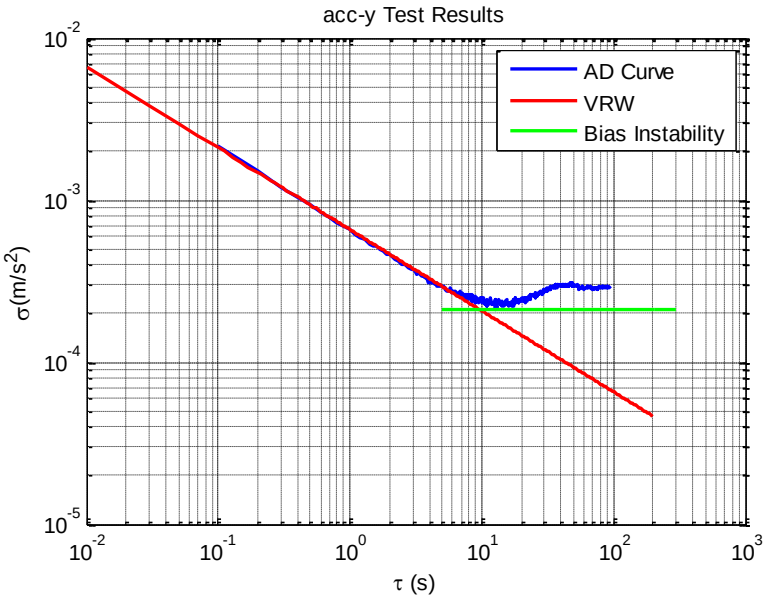

Figure 108 Allan deviation curve of y-axis accelerometer of the quartz IMU.

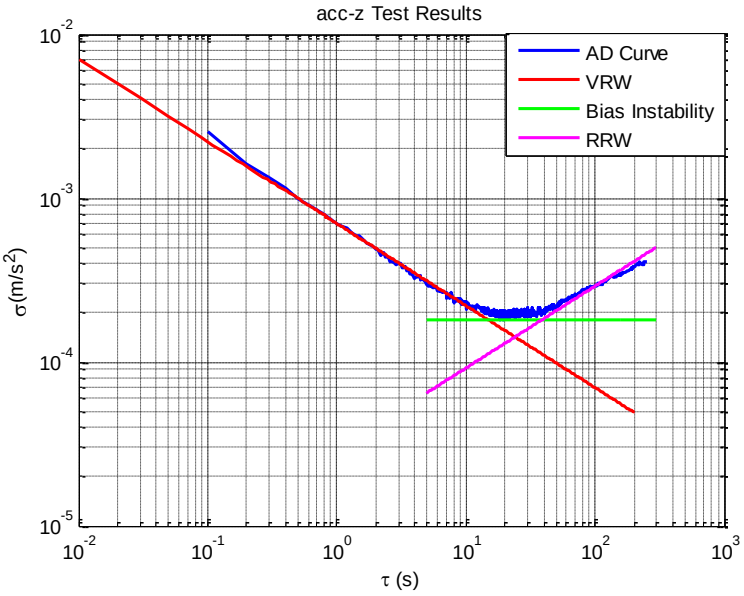

Figure 109 Allan deviation curve of z-axis accelerometer of the quartz IMU.

According to figures, only z-axis accelerometer has rate random walk. Moreover time range of bias instability is very short for z-axis accelerometer; therefore, bias

instability is not the dominant error in Figure 109. Additionally, x-axis and y-axis accelerometers do not have rate random walk error. Detailed error parameters are demonstrated in Table 20 and Table 21.

Table 20 Identified error parameters of the quartz accelerometer with line method.

Accelerometer	**Velocity Random Walk(mg/√Hz)**	**Bias Instability(m/s^2)**	**Rate Random Walk($m/s/h^{3/2}$)**	**Time constant (s)**
x-axis	0.0757	0.000243	-	30
y-axis	0.0674	0.00032	-	10
z-axis	0.0716	0.00027	10.8	20

Table 21 Identified error parameters of the quartz accelerometer with proposed method

Accelerometer	**Velocity Random Walk(mg/√Hz)**	**Bias Instability(m/s^2)**	**Rate Random Walk($m/s/h^{3/2}$)**	**Time constant (s)**
x-axis	0.0846	0.00027	-	30
y-axis	0.0741	0.00042	-	13
z-axis	0.0796	0.0002	11.65	22

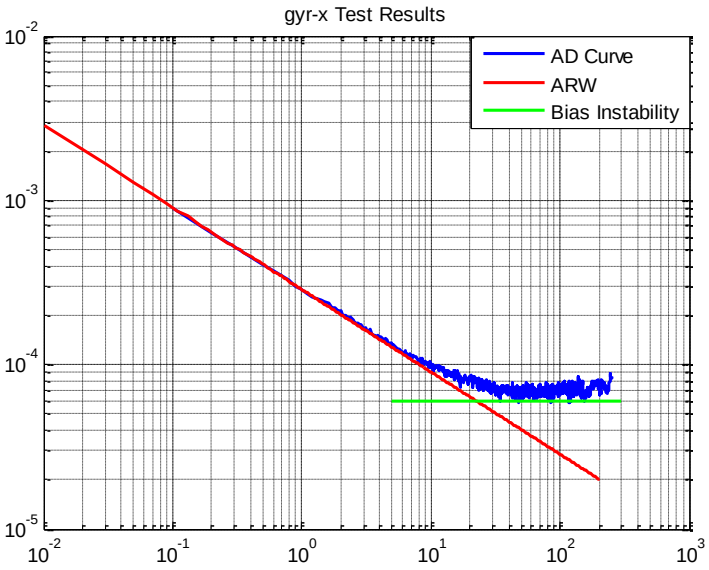

Figure 110 Allan deviation curve of the x-axis gyroscope of the quartz IMU.

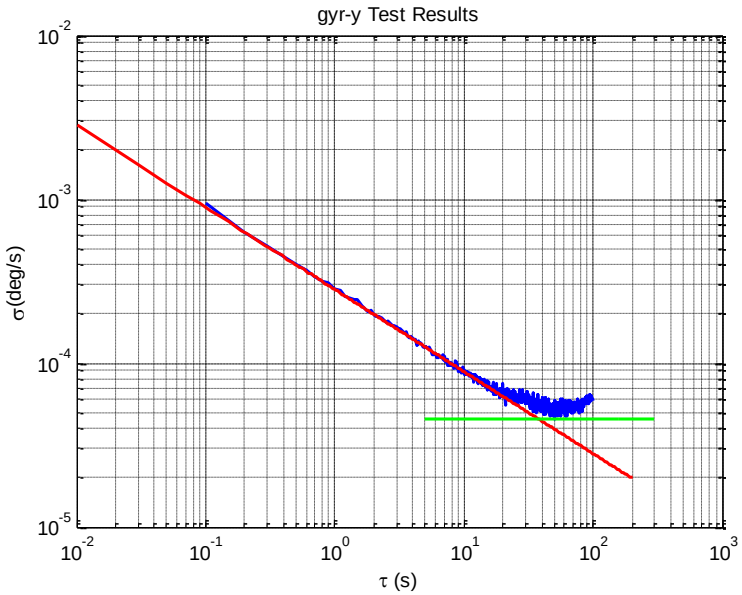

Figure 111 Allan deviation curve of y-axis gyroscope of the quartz IMU.

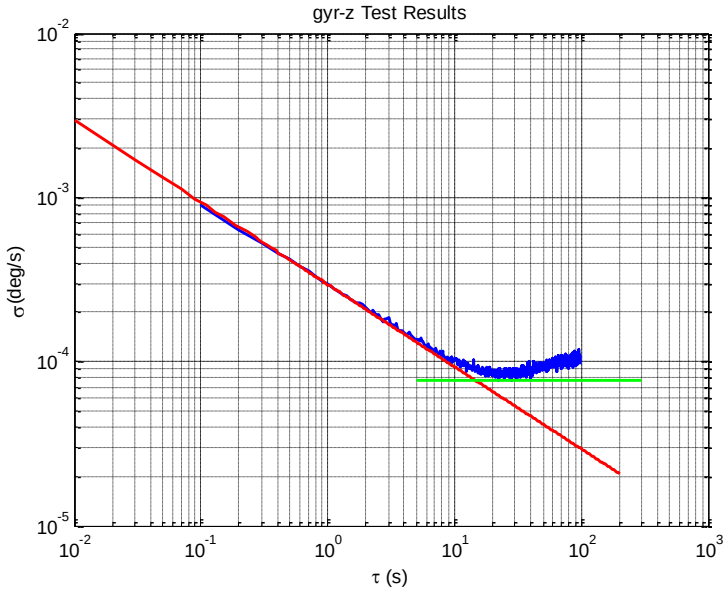

Figure 112 Allan deviation curve of z-axis gyroscope of the quartz IMU.

Bias instability and angle random walk are dominant error terms for quartz gyroscopes; therefore, these two errors are modeled. Gyroscope error levels are lower than MEMS IMU 1 and MEMS IMU 2, due to the accuracy of quartz structure.

Table 22 Identified error parameters of the quartz gyroscope with the line method.

Gyroscope	**Angle Random Walk(deg/√h)**	**Bias Instability (deg/h)**	**Time constant (s)**
x-axis	0.017	0.21	30
y-axis	0.016	0.17	30
z-axis	0.017	0.27	20

Yet, one can obtain these bulges if details are increased in the Allan deviation curve (decrease the time difference between two tau values). This problem is discussed in Section 4.3.1.5 for more details.

Table 23 Identified error parameters of the quartz gyroscope with the proposed method.

Gyroscope	**Angle Random Walk(deg/√h)**	**Bias Instability (deg/h)**	**Time constant (s)**
x-axis	0.0176	0.37	42
y-axis	0.0173	0.25	50
z-axis	0.0175	0.23	20

As can be seen in the figures, noise levels are better than MEMS sensors, especially for gyroscopes. Therefore, noise levels are important indicators of IMU classification. Bias instability is a critical parameter, because it is non-stationary, hence; total error increases with data size. Moreover, angle random walk is the dominant error term and it is primarily used for sensor classification but bias instability is another major term for long-range applications. This quartz IMU is in the tactical level because both deterministic and stochastic errors are in the tactical grade levels as indicated in Table 3.

Before simulations, we have to know filter characteristic of the IMU; but we only know the minimum bandwidth from the manual of the IMU. We do not have any additional information about the exact bandwidth. PSD is a good solution when frequency dependent characteristic come into question. We first evaluate the PSD function of the quartz IMU and then establish a filter, which determines the bandwidth of the IMU.

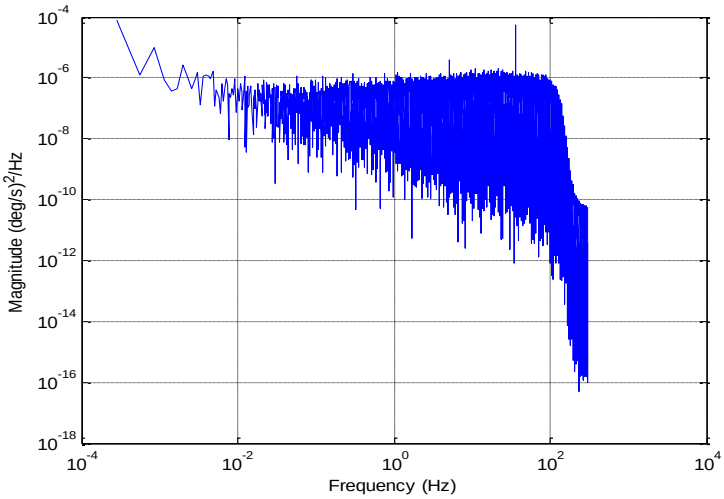

Figure 113 PSD curve of the quartz gyroscope.

According to Figure 113, bandwidth of the quartz sensor is nearly 100 Hz maybe we cannot evaluate exact -3dB point from the figure, but we have an approximate bandwidth. Accuracy of modeling is highly dependent on the accurate modeling of the filter.

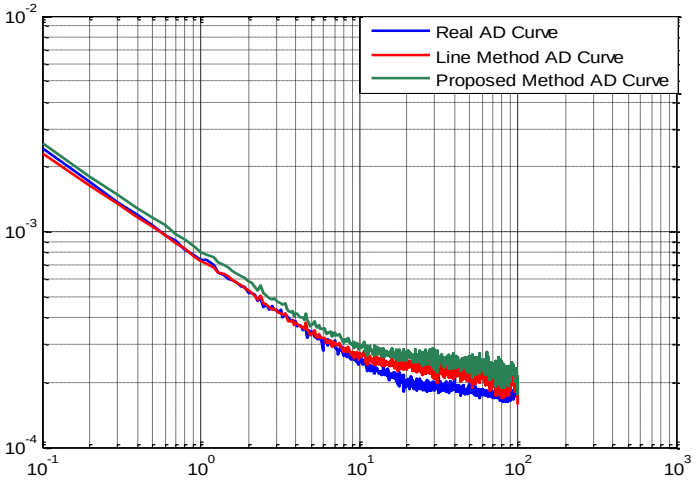

Figure 114 Modeling results of x-axis accelerometer.

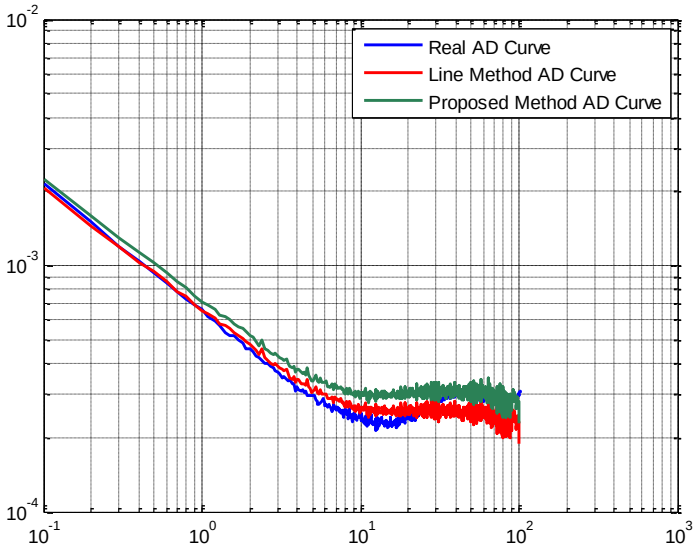

Figure 115 Modeling results of y-axis accelerometer.

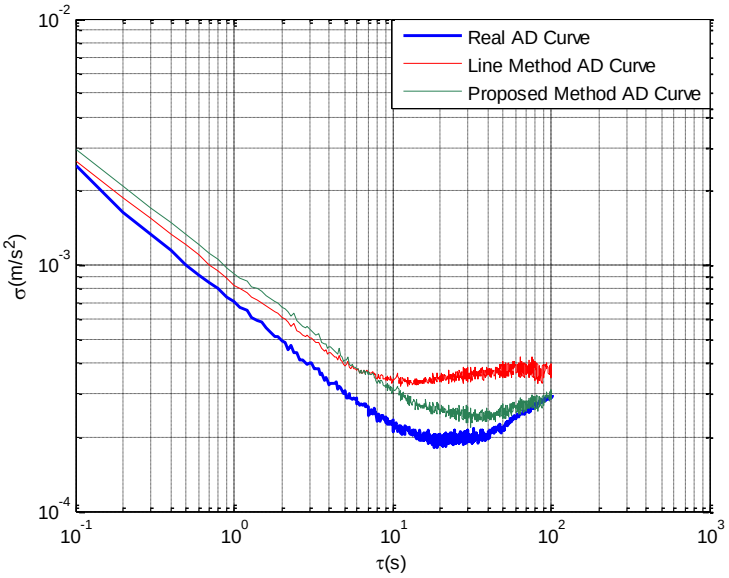

Figure 116 Modeling results of z-axis accelerometer.

Differences occur between curves due to the summation of the different errors. For example, summation of the angle random walk and bias instability generates higher

errors than expected. This situation happens owing to the small time range of the bias instability and existence of rate random walk.

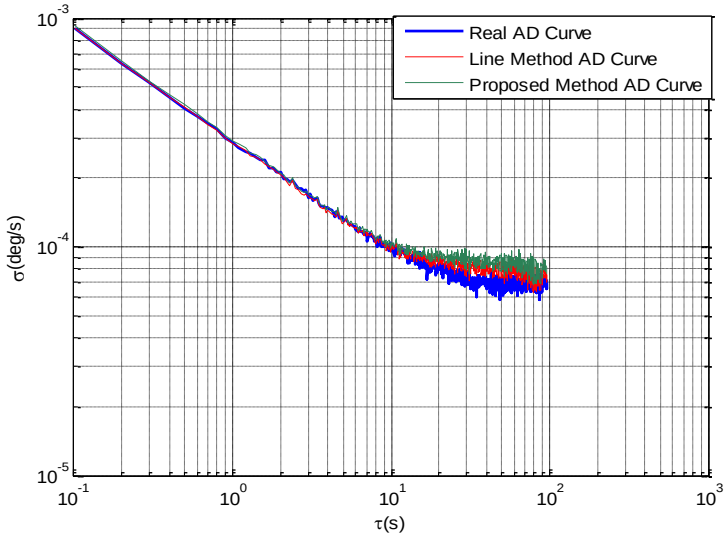

Figure 117 Modeling results of x-axis gyroscope.

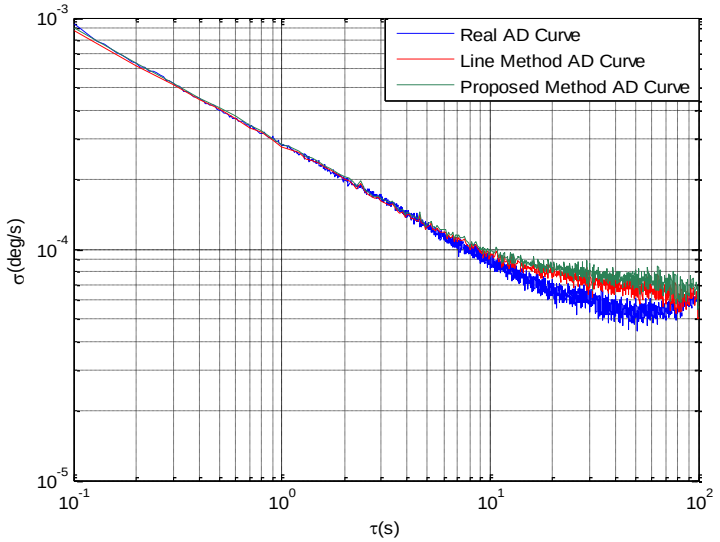

Figure 118 Modeling results of y-axis gyroscope.

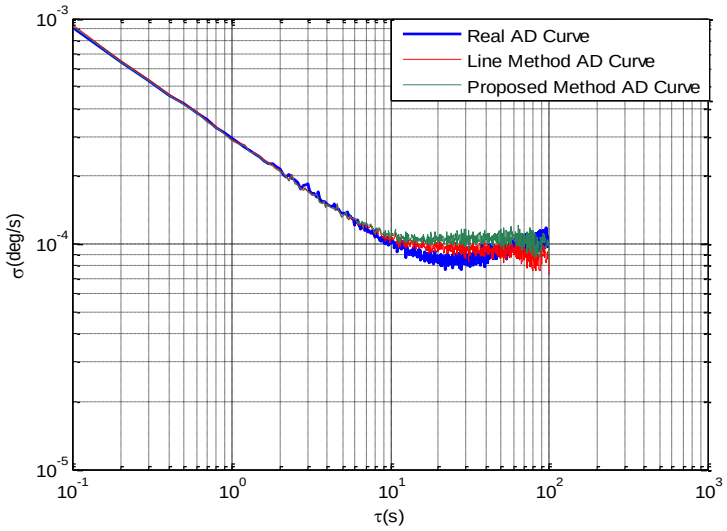

Figure 119 Modeling results of z-axis gyroscope.

6.3 Modeling Optical sensor

Optical sensors usually suffer from bias instability, quantization error and angle random walk. This type of sensors measure phase difference between two light beams. Phase difference is measured from fringe patterns. Sampling time of rate integrating sensor is not enough to count whole fringe patterns and remainder of movement is included in the output of the next output [29]. Hence, small errors occur due to the remainder. Remainder is the source of the quantization error [29]. Quantization error occurs in the rate integrating sensors; other type of sensors (i.e., MEMS) generally do not include this error term.

6.3.1 Ring Laser Gyro (RLG)

Ring laser gyroscopes use laser beams; therefore, their noise levels and magnitude of deterministic errors are very low. Hence, ring laser gyros are tactical grade sensors. Yet, dither movement is the main reason of the sinusoidal component in Allan

deviation curve of ring laser gyroscopes. Thus, slope of -1 can be obtained in Allan deviation curve of the gyroscopes, but origin of this slope is the sinusoidal component. Additionally, PSD analysis shows that angle random walk and quantization errors are the dominant error terms for RLGs. Allan deviation curves of RLG are demonstrated in Figure 120 to Figure 122.

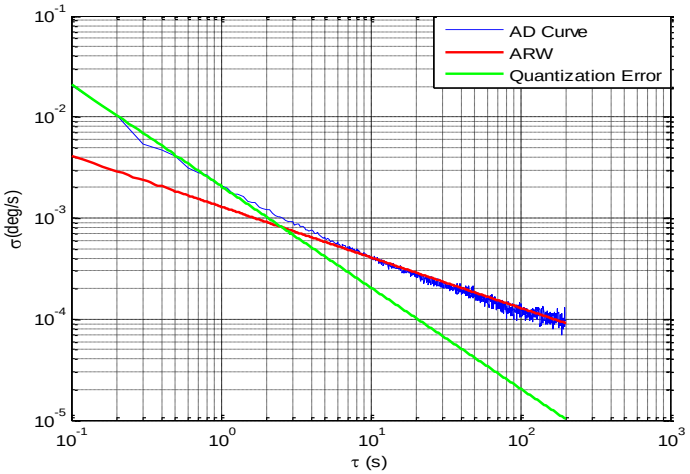

Figure 120 Allan deviation curve of x-axis RLG.

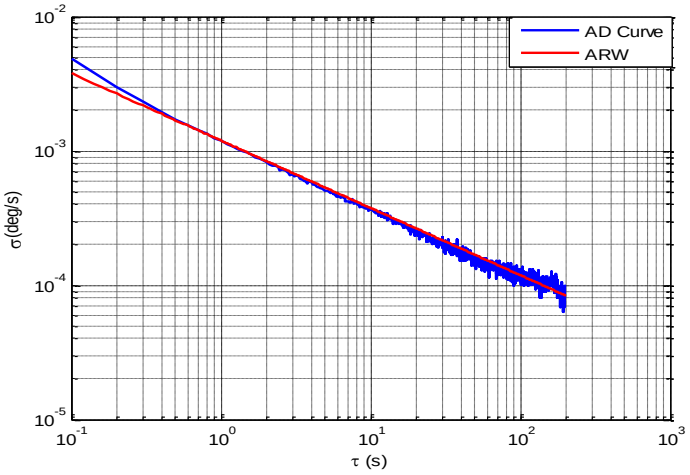

Figure 121 Allan deviation curve of y-axis RLG.

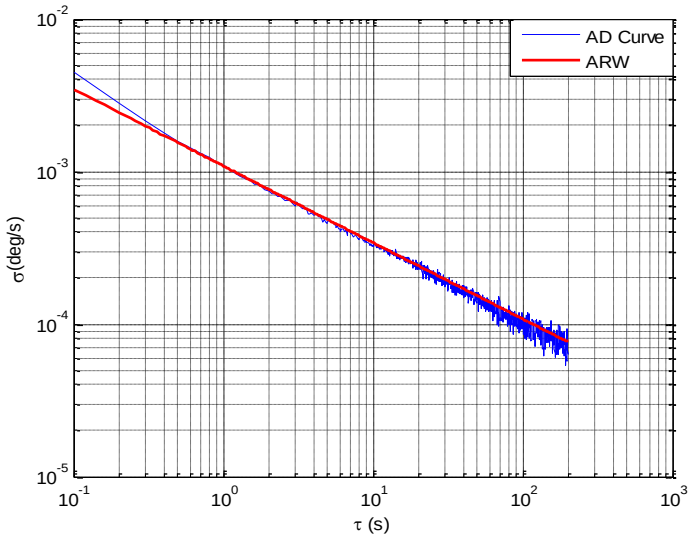

Figure 122 Allan deviation curve of z-axis RLG.

Table 24 Error parameters of the ring laser gyroscopes.

Gyroscope	**Angle Random Walk(deg/√h)-Line Method**	**Angle Random Walk(deg/√h)-τ = 1 sec equivalence**	**Quantization error (arcsec)-Line Method**
x-axis	0.078	0.126 (higher than manual)	4.822
y-axis	0.071	0.073	2.125
z-axis	0.065	0.066	2.116

Table 24 shows that angle random walk of x-axis gyroscope is higher than defined angle for random walk parameter in IMUs manual, according to $\tau = 1$ sec equivalence. RLG sensors are generally affected by dithering moreover; Allan deviation curve shows dither components in the short correlation time (0.1 s $<\tau <$ 10 s). Therefore, this situation causes inaccurate determination of angle random walk and quantization error in the Allan deviation curve. We have to analyze this sensor with the proposed method to find the exact angle random walk and quantization error.

PSD is used for identification of quantization error of RLG sensor, because sinusoidal components due to the dither are shown by Allan deviation curve. Hence, parameter of quantization error is affected. PSD is more reliable than Allan deviation method when quantization error comes into question, because both sinusoidal errors due to dither and quantization error can be shown to be slope of -1 region in the Allan deviation curve.

PSD plots of RLG sensors are shown in Figure 123 to Figure 125. Frequency averaging is applied to the PSD and then quantization error parameters are identified.

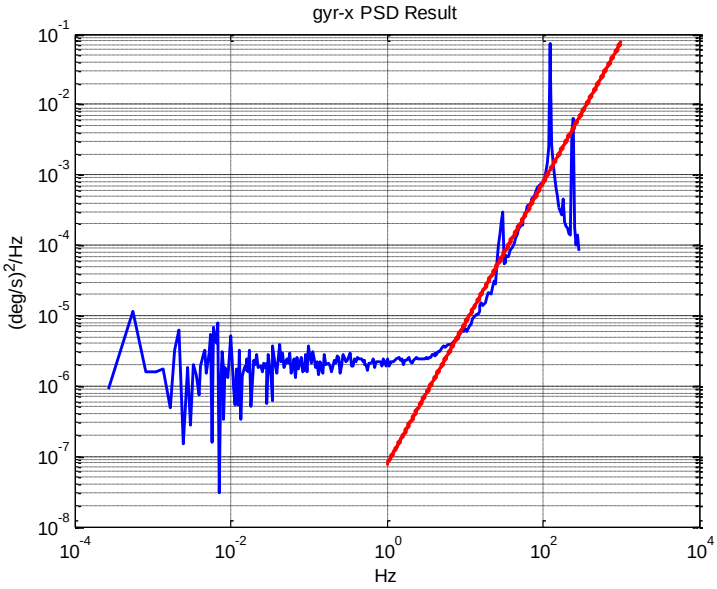

Figure 123 Identification of quantization error of the x-axis gyroscope with PSD method.

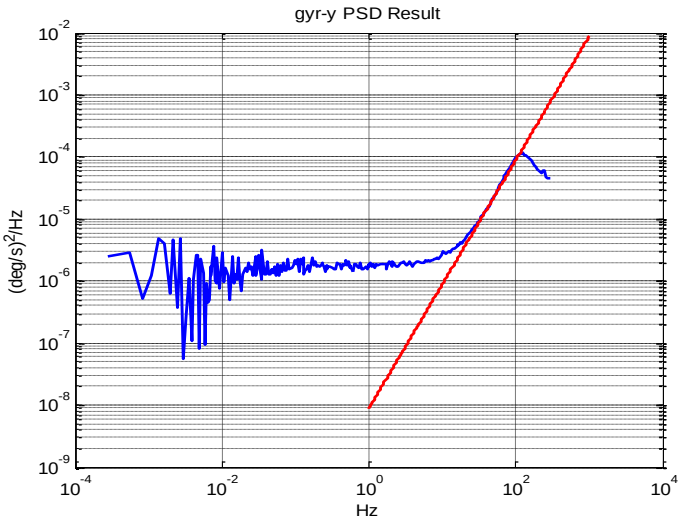

Figure 124 Identification of quantization error of the y-axis gyroscope with PSD method.

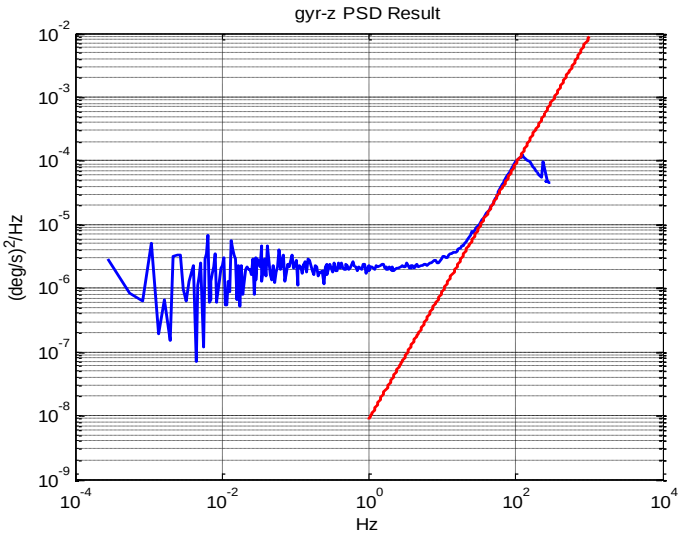

Figure 125 Identification of quantization error of the z-axis gyroscope with PSD method.

Quantization error is the dominant term in 0.1s < $\tau \leq$ 0.5s range and angle random walk is the dominant term in 0.5s < τ < 200 s, hence; membership functions are generated according to this information. The proposed method is applied to the

Allan deviation data to estimate error terms. Table 25 indicates that the proposed method is effective for investigating quantization noise because it estimates very similar parameters with the PSD method.

Table 25 Quantization error of the RLG sensors for different methods.

RLG	**Quantization error (arcsec)- Line Method**	**Quantization error (arcsec)- PSD**	**Quantization error (arcsec)- Proposed Method**
x-axis	4.822	2.808	2.946
y-axis	2.125	0.923	0.761
z-axis	2.116	0.828	0.775

Table 26 Estimated error parameter comparison for the proposed method and Allan deviation method.

RLG	**Angle Random Walk(deg/√h)- Line Method**	**Angle Random Walk(deg/√h)- $\tau =$ 1 sec equivalence**	**Random Walk (deg/√h)- Proposed Method**
x-axis	0.082	0.126(higher than manual)	0.091
y-axis	0.071	0.073	0.066
z-axis	0.065	0.066	0.062

The proposed method estimates the angle random walk in the normal range that is defined in producer manual. This result shows that the line method results are affected from the sinusoidal or other disturbances. As shown in Allan deviation

curves, angle random walk level is nearly the same with the quartz sensor, but RLG has better white noise characteristic than MEMS sensors. RLG has additional dither movement and this movement has to be inserted in RLG models as indicated before.

Resulting Allan deviation curves and modeling results are shown in Figure 126 to Figure 128.

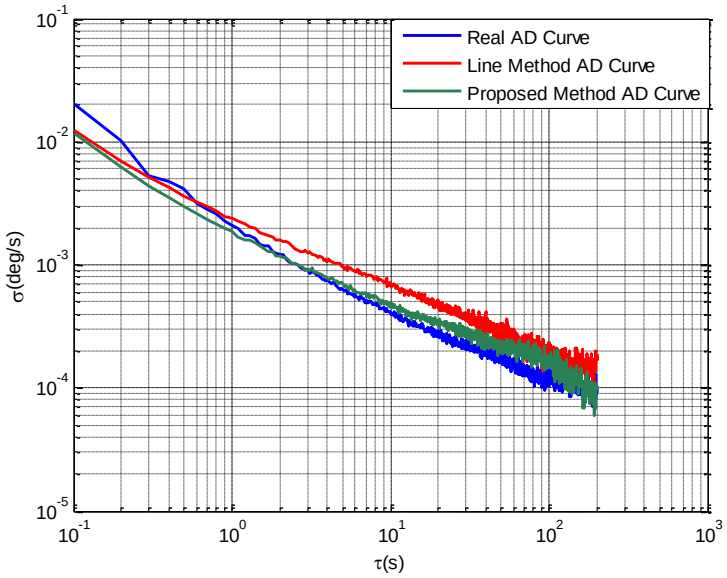

Figure 126 Comparison of Allan deviation curves of real and simulated data for x-axis RLG.

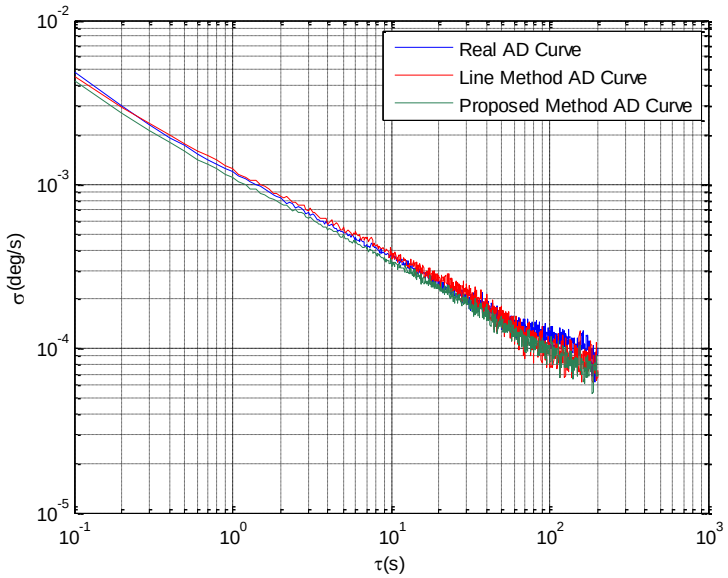

Figure 127 Comparison of Allan deviation curves of real and simulated data for y-axis RLG

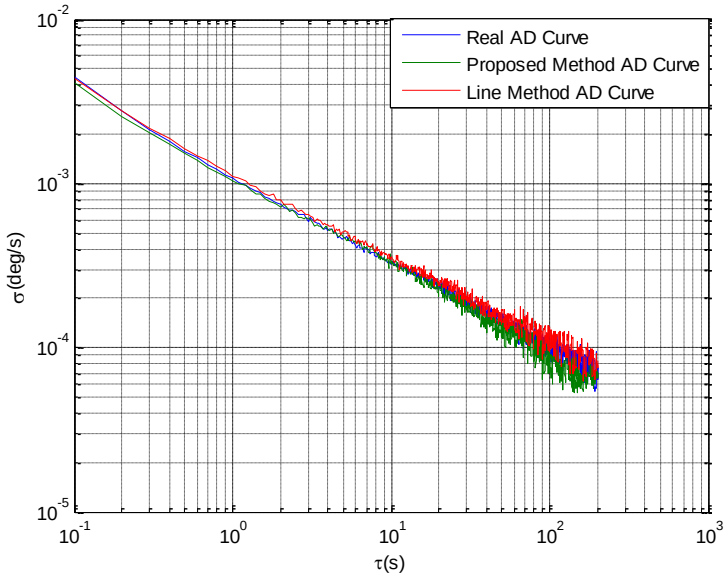

Figure 128 Comparison of Allan deviation curves of real and simulated data for z-axis RLG.

Correlation time of bias instability is very long for RLG sensors, therefore it does not included in this work. Quantization error and angle random walk are the dominant error terms, especially when angle random walk characteristic has to be inspected deeply because it affects all time scale in the Allan deviation curve.

6.3.2 Fiber optic gyroscope

FOG sensors are, either rate integrated type or rate sensors, depending on their electronic read-out circuit. Therefore, quantization error can be seen in the measurements of FOGs. Sometimes, angle random walk is more dominant than quantization error for open-loop FOG sensors. This is the reason of why we cannot obtain quantization error for some open-loop FOGs. On the other hand, quantization error is minimized in close-loop operation. However, quantization error is also encountered in Allan deviation curves, but with amplitude being smaller than that of RLG sensors.

Two types of fiber optic gyroscope are investigated in this thesis. Open-loop FOG sensors are simple, low cost and low power devices and they are in the tactical grade. Output of an open-loop FOG is generally voltage but thermal errors affect the output. On the other hand, closed-loop FOG sensors have high dynamic range but they require high power and additional read-out circuits. Hence, these type sensors are more expensive than open-loop fiber optic gyroscopes but close-loop FOG sensors are in the navigational grade class. It should be noted that, before investigating random errors, PSD method should be used.

6.3.2.1 Open-Loop FOG sensor

Allan deviation curve and PSD curve of single-axis open-loop FOG sensor are shown in Figure 129 and Figure 130. Error parameters are identified with Allan deviation method and PSD method, error parameters are shown in Table 27.

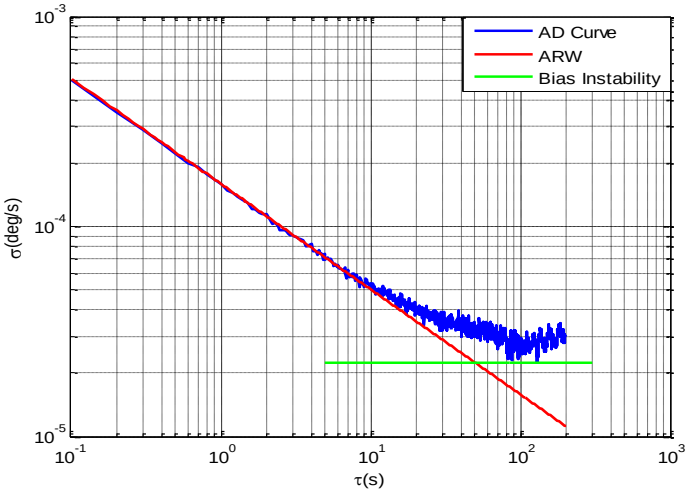

Figure 129 Allan deviation curve of the open-loop FOG sensor.

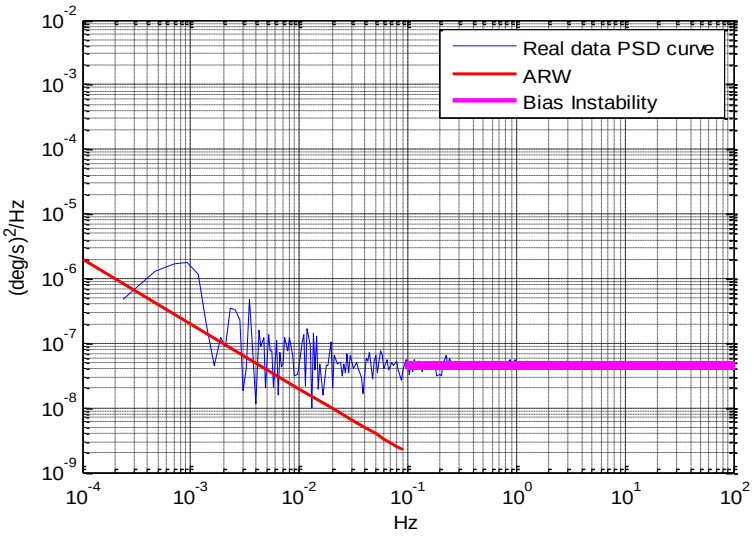

Figure 130 PSD curve of the open-loop FOG sensor.

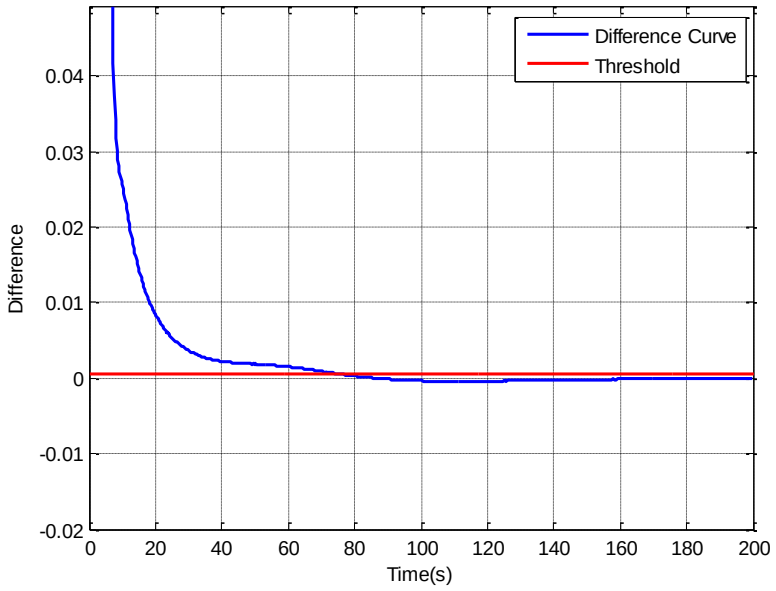

Figure 131 Applying threshold value to the open loop FOG sensor.

0.5 s < $\tau \leq$ 65 s is the dominant region for angle random walk and 65 s < $\tau \leq$ 100 s is the dominant region for bias instability. 65 s is found by threshold method; therefore membership functions are formed according to this information. As previously stated, transition region between angle random walk and bias instability is selected as 10 s. Figure 130 shows that this data includes bias instability and angle random walk because output of open-loop FOG sensor is generally voltage. Therefore, data contains dominant angle random walk; quantization noise is not observed from open loop RLG sensor.

Table 27 Error parameters of open-loop FOG sensor. These parameters are identified with Allan deviation method and PSD method.

Error Parameter	**Allan Deviation Curve-Line Method**	**PSD Method**	**Proposed Method**
Bias Instability (deg/h)	0.1182	0.1215	0.135
Angle Random Walk(deg/√h)	0.0092	0.0092	0.0093
Time Constant (s)	60	Not Applicable	65

According to Figure 130, filter is not included in the algorithm of the sensor. It means that there is no need for a filter model. There is no quantization error because +2 slope is not observed from PSD curve. In addition, Allan deviation curve does not show quantization error. Therefore, only bias instability and angle random walk noises are modeled for open-loop FOG sensor.

Deterministic error parameters are given in Table 28. These parameters are taken from the manual of the FOG sensor. G-dependent bias can be ignored due to the structure of optical sensors.

Table 28 Deterministic error parameters of the open-loop FOG.

Error Parameter	**Magnitude**
Scale Factor (3σ) ppm	2900
Bias Error (3σ) (deg/h)	10

Deterministic and random error parameters are included in the sensor model and comparison of Allan deviation curve of real data and simulated data is given in Figure 132.

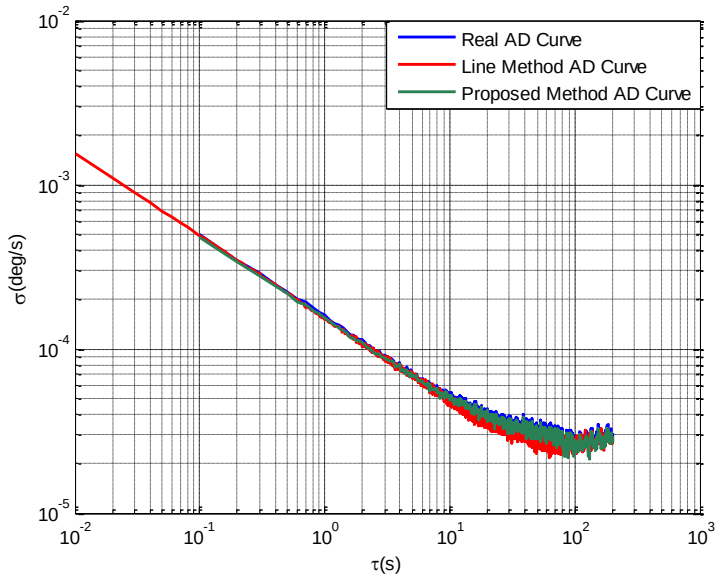

Figure 132 Comparison between simulation results and real data

The proposed method is somewhat better than the line method, but one important observation is that error parameters are estimated by any of the methods for the low-noise sensors. They produce very similar results, because the sensor is not affected by other noise terms (i.e., sinusoidal noise or exponentially correlated noise).

6.3.2.2 Close-loop FOG Sensor

Navigation grade close-loop FOG sensor is investigated in this thesis. Quantization error is identified by PSD method and this error is modeled by Equation (5.15).

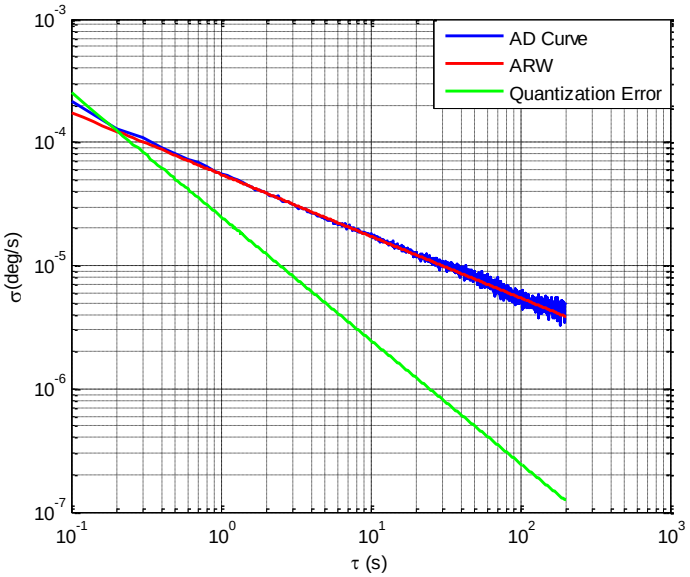

Figure 133 Allan deviation curve of the close-loop FOG sensor.

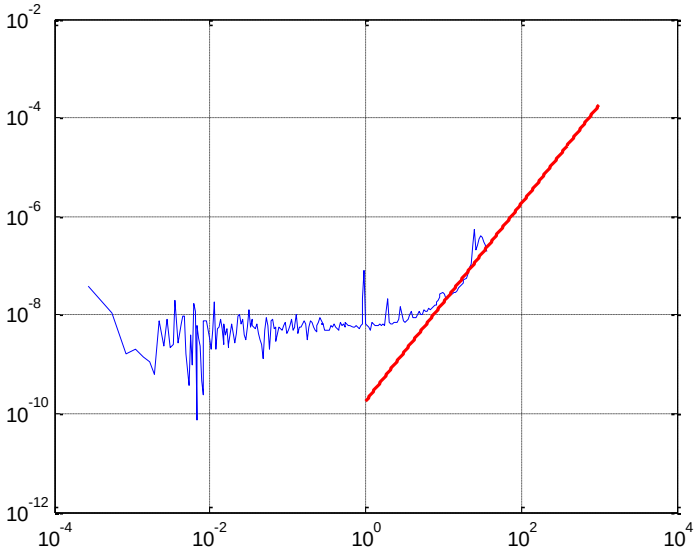

Figure 134 PSD curve of the FOG sensor.

According to Figure 133 and the proposed method, estimated error parameters are given in Table 29.

Table 29 Estimated error parameters of the close-loop FOG sensor

Error Parameter	**Allan Deviation-Line Method**	**Allan Deviation-Proposed Method**
Angle Random Walk(deg/√h)	0.0037	0.0034
Quantization Error (arcsec)	0.0576	0.074

Quantization error is formed as,

$$\begin{aligned} x[k] &= 0.0103\,w[k] \\ y[k] &= x[k] - x[k-1] \\ w[k] &= White\,sequence \end{aligned} \tag{6.5}$$

Sigma value of white noise can be generated by the following equation:

$$\begin{aligned} \Delta t &= 0.002\,s \\ \sigma_N &= \frac{0.0034}{\sqrt{\Delta t}} \\ y[k] &= \sigma_N w[k] \\ w[k] &= White\ sequence \end{aligned} \tag{6.6}$$

FOG is modeled in accordance with Equation (6.5) and Equation (6.6). Bias instability is not observed from the PSD figures hence it is not included in the noise model.

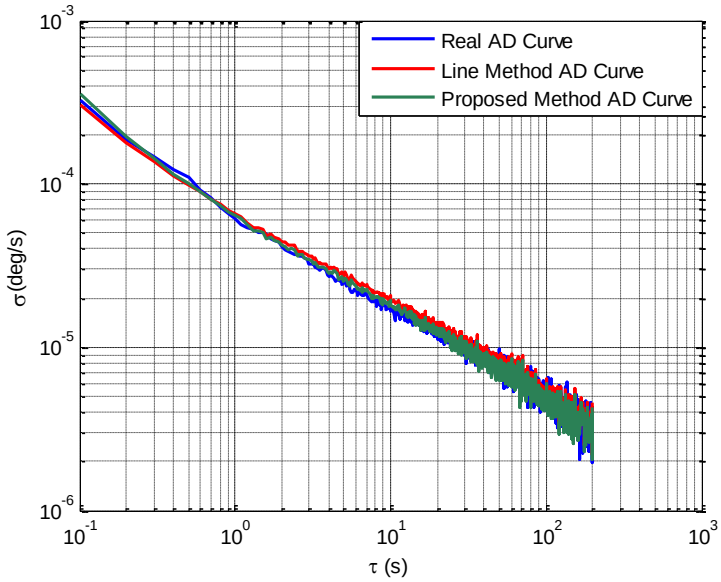

Figure 135 Comparison of Allan deviation curve of real data and simulated data for the close loop FOG sensor.

An angle random walk coefficient of closed-loop FOG sensor is better than other sensors. These noise levels are enough for sensitive angle measurements (e.g., aircrafts, UAVs, long-range missiles, etc.).

CHAPTER 7

CALIBRATION OF THE FOG SENSOR

Error estimation and error degradation processes are essential to increase the accuracy of sensors and navigation processes. The proposed method identifies random error parameters to be used. Additionally, some parameters are important to estimate errors. For example, sampling time and time constant form state transition matrix and process noise covariance matrix of bias instability.

As mentioned before, magnitude of deterministic errors change with temperature. Therefore, behavior of errors has to be investigated. Thus, calibration tests are performed under different temperatures to catch error characteristics. Temperature difference between two successive temperature points is selected carefully, because if these points are selected close to each other, test duration increases. Yet, optimal temperature steps are generally determined by several experiments.

Calibration tests are performed in the rate tables under different temperatures. Sensitivity and accuracy of rate table is also important to estimate sensor errors accurately. If exact turn rate is not captured, it can cause incorrect estimation of error parameters.

Multi-position tests are applied to determine sensor errors precisely [15], but six-position test is usually sufficient [3]. Multi-position tests increase the test duration; therefore, random errors correlate the output of the sensor.

Additionally, error parameters are estimated at each temperature and a polynomial is fitted to all temperature range. This polynomial is used in the IMU error compensation algorithm [6]. The same process is repeated for all deterministic errors.

Therefore, degree of polynomial is important for error compensation algorithms, because process time of algorithm depends on the multiplication operations in the error compensation algorithms [6].

Temperature difference is selected 10 ^{0}C in this thesis and a 4th degree polynomial is fitted to deterministic errors. For this application, open-loop FOG sensor is selected. Operating range of FOG sensor is between -40 ^{0}C and 75 ^{0}C. Therefore, we perform calibration tests under twelve different temperatures (-40 ^{0}C to 70 ^{0}C).

Residuals of deterministic errors are important but their magnitude change with turn-on to turn-on. This circumstance can be explained as the repeatability of the deterministic error. After several turn-on to turn-offs residual are distributed with zero mean and known variance.

Measurement equation for gyroscope can be stated with the following;

$$\hat{w}_x = S_{gx} w_x + M_{gxy} w_y + M_{gxz} w_z + B_{gx} + G_{gx} a_x + n_{gx} \tag{7.1}$$

g-dependent errors are negligible error terms for FOG and RLG sensors because they use laser beams instead of the solid structures. We perform the test with single-axis FOG sensor; therefore, misalignment parameters can be ignored. Equation (7.1) is simplified as,

$$\hat{w}_x = S_{gx} w_x + B_{gx} + n_{gx} \tag{7.2}$$

We only estimate bias and scale factor as the deterministic error. We can rewrite the equation in the vector form for simplicity.

$$\hat{w}_x = [S_{gx}\ B_{gx}] \begin{bmatrix} w_x \\ 1 \end{bmatrix} + n_{gx} \tag{7.3}$$

We collected data at different 28 angular rates in order to increase the sensitivity of the calibration process. Suppose that matrix U is formed by the mean value of the sensor output for each step of the multi-position test. Matrix A is formed by exact inputs to the rate table.

$$U = MA$$

$$U = [u_1 u_2 u_3 ... u_{28}] \tag{7.4}$$

$$u_n = mean\, value\, of\, the\, sensor\, output$$

$$A = [a_1 a_2 ... a_{28}]$$

$$a_n = \begin{bmatrix} w_x \\ 1 \end{bmatrix} \tag{7.5}$$

$$w_x, input\, of\, the\, rate\, table\, (reference\, input)$$

Least-square method estimates the deterministic error in the output of the sensor. It is a very simple method and accuracy is high enough for identification of the sensor errors [15]. Equation of least squares estimation is given by,

$$M = UA^T (AA^T)^{-1}$$

$$M, error\, component\, matrix \tag{7.6}$$

Before the calibration tests are performed, FOG sensor is aligned true north because FOG sensor has capability of the measuring the rotation of the Earth. Hence, if we do not remove this term from our measurements we will estimate inaccurate bias terms. Rotation of the Earth for the given latitude is,

$$\Omega_{lat} = \Omega_e sinL$$

$$\Omega_{lat} = rotation\, rate\, of\, the\, Earth\ for\, given\, latitude$$

$$\Omega_e = rotation\, rate\, of\, the\, Earth\, (\approx 15.041 \text{deg}/h) \tag{7.7}$$

$$L = latitude$$

Calibration tests are performed on the 39.987086^0 north latitude and rotation rate on this point is 0.00268 ^{o}/s.

Measurement range of sensor is ±500 ^{o}/s thus, we evaluate between -490 ^{o}/s to +490 ^{o}/s with 70 ^{o}/s increments. Sampling rate of the sensor is 0.001 s and total test

duration is 280 s for calibration tests. An example of calibration data is shown in Figure 136.

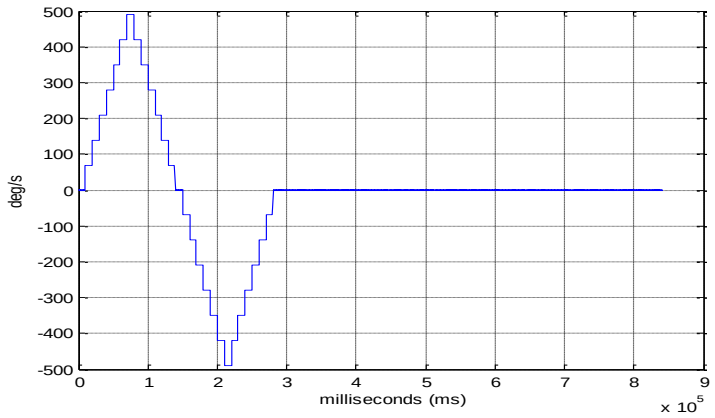

Figure 136 Calibration data of FOG sensor.

Deterministic error estimation and corresponding temperatures are given in Table 30.

Table 30 Estimated deterministic error terms under different temperatures.

Temperature (^{o}C)	**Bias (deg/h)**	**Scale Factor (ppm)**
-40 ^{o}C	2.1268	1199
-30 ^{o}C	1.8260	1002
-20 ^{o}C	0.9252	1099
-10 ^{o}C	1.6962	1149
0 ^{o}C	1.9759	880
10 ^{o}C	-0.6767	1349
20 ^{o}C	1.1252	919
30 ^{o}C	-1.2771	992
40 ^{o}C	-0.1760	1056
50 ^{o}C	-0.3761	869
60 ^{o}C	-1.6776	1084
70 ^{o}C	-1.5270	799

We can fit a polynomial according to parameters of the Table 30. Parameters and fitted curves are shown in Figure 137 and Figure 138.

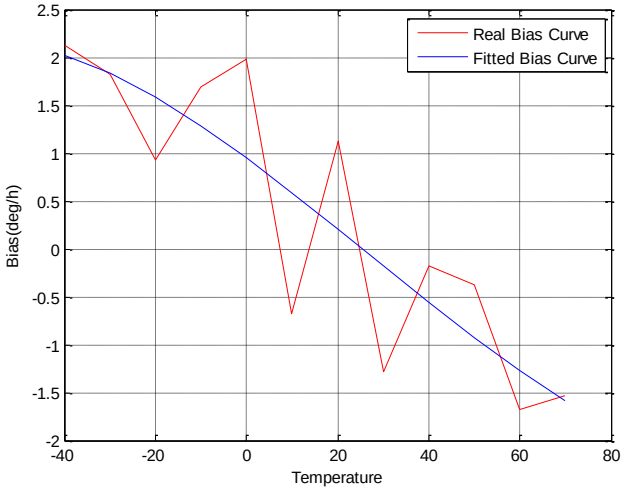

Figure 137 Real and fitted curves for bias error

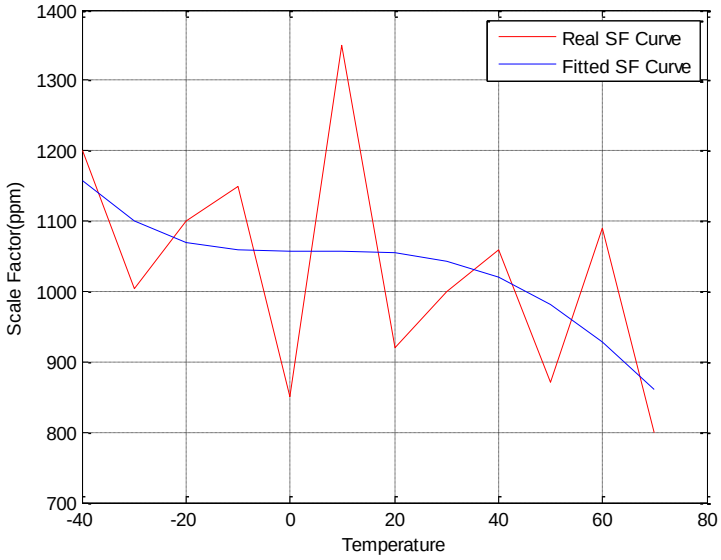

Figure 138 Real and fitted curves for scale factor error

Total angle error is investigated under room temperature (25 ^{0}C) at 10 ^{o}/s rotation rate. Thermal rate of FOG sensor is 1 ^{0}C/min, which means that temperature of sensor increases 1 ^{0}C per minute. This information can be used by error compensation algorithm. Total angle for given rotation rate is calculated by the following expression:

$$\theta_{total} = \sum_{k=1}^{t} w_k \, \Delta t$$
$$\Delta t = sampling\ time \tag{7.8}$$
$$w_k = sensor\ output$$

Angle error increases due to the summation operation. Two main cases are compared with each other to show efficiency of the calibration and error estimation.

- Angle error in raw data
- Angle error in only deterministic error calibrated data

Angle error is stated as the following expression:

$$\theta_{error} = \theta_{total} - \theta_{true}$$
$$\theta_{true} = \sum_{k=1}^{t} w_{true}\, dt \tag{7.9}$$

Uncompensated data is shown in figure for w_{true}=10 ^{o}/s input.

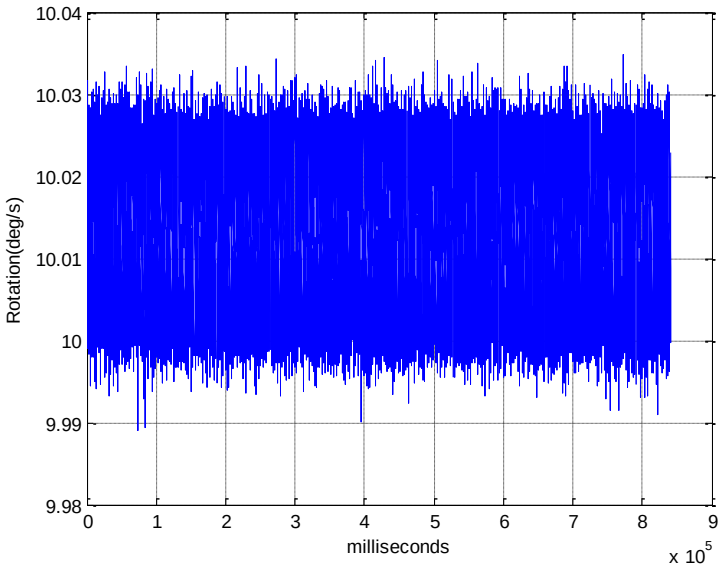

Figure 139 Uncompensated data for the FOG sensor.

Total angle error is calculated through the Equation (7.9) which is about 12 degrees after 840 seconds.

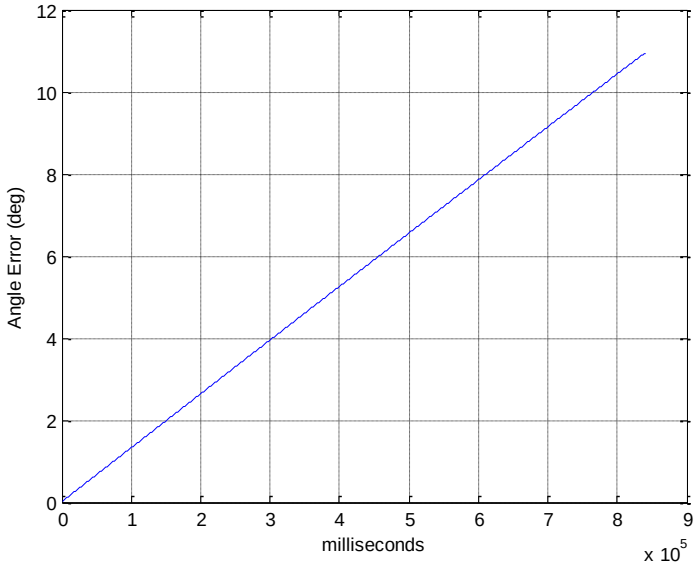

Figure 140 Total angle error on the uncompensated FOG data.

Total error is slightly low for the FOG sensor because bias and noise levels are very low even if sensor is not calibrated. Error compensation parameters are applied to data through Equation (7.10) then total angle error is evaluated again.

$$\begin{aligned} w_c &= \left(S_{gyr}{}^{-1} w_{uc} - B_{gyr} \right) \\ S_{gyr} &= Scale - factor\, error \\ B_{gyr} &= Bias\, Error \\ w_{uc} &= uncompensated\, angular\, rate \end{aligned} \tag{7.10}$$

Deterministic errors in Equation (7.11) are replaced with their polynomial equivalences.

$$\begin{aligned} S_{gyr} &= aT^4 + bT^3 + cT^2 + dT + e \\ B_{gyr} &= kT^4 + lT^3 + mT^2 + nT + r \end{aligned} \tag{7.12}$$

Polynomial coefficients for Equation (7.12) are given below.

$$\begin{aligned} S_{gyr} &= -4.2x10^{-9}T^4 + 1.96x10^{-6}T^3 - 1.31x10^{-4}T^2 - 0.0353T + 0.9517 \\ B_{gyr} &= 5.49x10^{-6}T^4 - 0.0011T^3 + 0.0113T^2 + 0.0871T + 1057 \\ T &= temperature \end{aligned} \tag{7.13}$$

Error compensated data is shown in Figure 141.

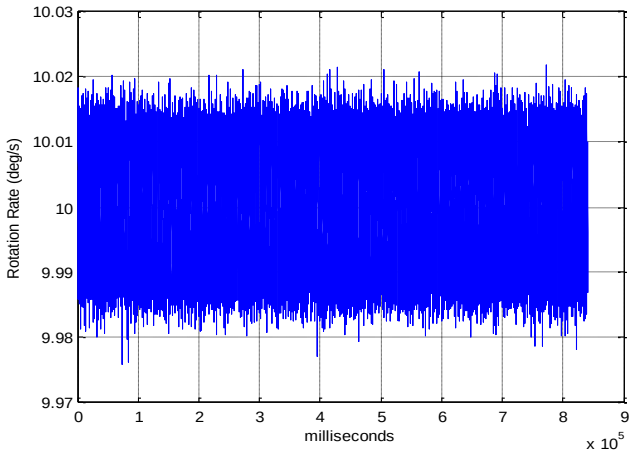

Figure 141 Compensated FOG data.

Residual bias is 0.05 deg/h after the compensation process. These error levels are applicable for long-range applications but some improvements are provided by Kalman filtering.

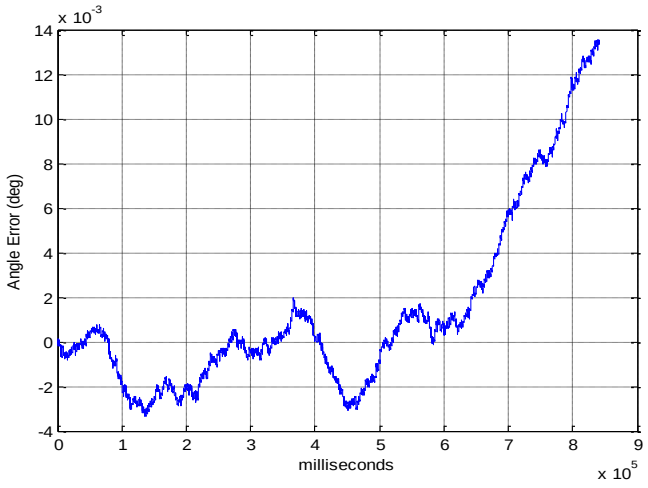

Figure 142 Total angle error for the compensated FOG data.

To sum up, temperature calibration is essential for an inertial sensor, but repeatability of errors causes angle, position or velocity error in the INS. This repeatability value

is somewhat random for specific turn-ons. If deterministic errors are not estimated correctly, errors in INS system grow dramatically.

CHAPTER 8

CONCLUSION

This study proposes that a method which estimate random error parameters from the Allan deviation results. This method is effective to find random error parameters of an inertial sensor and it solves problems of the line method. Line method generally has some estimation error if it is used for disturbed data. RLG sensor is one of the most important applications of the proposed method because corresponding value of $\tau = 1$ s is not suitable with the manual of RLG. Threshold value for correlation time of bias instability is somewhat easier than most of the probabilistic methods, but it requires some initial knowledge about the error characteristic on the Allan deviation curve of an inertial sensor. Membership functions are also used to identify stochastic errors successfully. Parameters of these functions can be adjusted adaptively regarding to empirical data.

Autocorrelation method is generally used to estimate time constant of a sensor but it can be used to detect periodic signals in a sensor output. It is very essential for navigation system design, because some systems cannot work with a specific sinusoidal noise, which has frequency in the bandwidth of the system.

PSD is one of the most important functions, which reveal error parameters, but it has deviations in high frequency ranges. PSD method requires frequency averaging but resolution of PSD is not good for low frequency components. PSD method also depends on line hence, determination of true line is very crucial. Moreover, quantization error can be estimated from PSD curve and it is not affected by dithering or other high frequency components. Because, sinusoidal noise has Dirac components on the PSD curve.

The most important error terms are deterministic errors. Magnitude of these errors changes with temperature and they have to be compensated with several calibration tests. Temperature tests are performed in a rate table under different temperatures. 4^{th} degree polynomial is fitted to interpolate deterministic errors. It seems enough to degrade sensor errors. Additionally, if temperature dependency of deterministic errors is not investigated, Allan deviation curves have undesired deviations. In that case, both the line method and the proposed method give inaccurate solutions.

REFERENCES

[1] S.M. Grewal, P.A. Andrews, G.C. Bar, *Global Navigation Satellite Systems, Inertial Navigation, and Integration*, Wiley, 2013.

[2] P.D. Groves, *Principles of GNSS, Inertial, and Multisensor Integrated Navigation Systems*, Artech House, 2008.

[3] P. Aggarwal, Z. Syed, A. Noureldin, N. El-Shimy, *MEMS-Based Integrated Navigation*, Artech House, 2010.

[4] P. Aggarwal et. al., "A Standard Testing and Calibration Procedure for Low Cost MEMS Inertial Sensors and Units", *Journal of Navigation*, vol. 61, pp. 323-336, 2007.

[5] Y. Günhan, "Detection and Compensation of Inertial Measurement Unit Errors", M.Sc. Thesis, Hacettepe University, 2014.

[6] B. Altınöz, D. Ünsal, "Look-up Table Implementation for IMU Error Compensation Algorithm", *IEEE/ION PLANS*, pp. 259-261, 2014.

[7] G.Q. Alex, F. Gianluca, F. Emanuela, D. Faibo, F. Carles, "A Comparison between Different Error Modeling of MEMS Applied to GPS/INS Integrated Systems", *Sensors 2013*, vol. 13, no. 8, pp. 9549-9588, 2013.

[8] J.O. Woodman, "An Introduction to Inertial Navigation", Technical Report, University of Cambridge, 2007.

[9] V. Saini, S.C. Rana, M.M. Kuber, "Online Estimation of State Space Error Model for MEMS IMU", *Journal of Modelling and Simulation of Systems,* vol. 1-2010, no. 4, pp. 219-225, 2010.

[10] A. Ünver , "Determination of Stochastic Model Parameters of Inertial Sensors", Ph.D. Thesis, Electrical and Electronics Eng. Dept., METU, 2013.

[11] H. Hou, "Modeling Inertial Sensors Errors Using Allan Variance", M.Sc. Thesis, Department of Geomatics Engineering, University of Calgary, 2004.

[12] S.W. Flenniken, "Modeling Inertial Measurement Units and Analyzing the Effect of their Errors in Navigation Application", M.Sc. Thesis, The Graduate

Faculty of Auburn University, 2005.

[13] A. Noureldin, T.B. Karamat, J. Georgy, *Fundamentals of Inertial Navigation, Satellite-based Positioning and their Integration*, Berlin Heidelberg: Springer-Verlag, 2013.

[14] D.H. Titterton, J.L. Weston, *Strapdown Inertial Navigation Technology*, The Institution of Electrical Engineers, 2004.

[15] D. Ünsal, "Estimation of Deterministic and Stochastic IMU Error Parameters", M.Sc. Thesis, Electrical and Electronics Eng. Dept., METU, 2012.

[16] H. Zumbahlen, *Linear Circuit Design Handbook*, Elsevier, 2008.

[17] Metra Mess- und Frequenztechnik, Introduction to accelerometers, http://www.new.mmf.de/introduction.htm, last visited on: 18/8/2015.

[18] Accelerometers, https://en.wikipedia.org/wiki/Piezoelectric_accelerometer, last visited on: 2/9/2015.

[19] T.K. Bhattacharyya, A.L. Roy, *Micro and Smart Devices and Systems*, Springer, 2014.

[20] Y. Yüksel, B.H. Kaygısız , "Notes on Stochastic Errors of Low Cost MEMS Inertial Units", Technical Report, University of Calgary, 2013.

[21] "IEEE Standard Specification Format Guide and Test Procedure for Single-Axis Interferometric Fiber Optic Gyros", IEEE Std 952, 1997.

[22] P.G. Savage, "Analytical Modeling of Sensor Quantization in Strapdown Inertial Navigation Error Equations", *Journal of Guidance, Control and Dynamics*, vol. 25, no. 5, pp. 833-842, 2002.

[23] G.R. Brown, P.Y. Hwang, *Introduction to Random Signals and Applied Kalman Filtering with Matlab Exercises and Solutions*, John Wiley & Sons, 1997.

[24] J.Skaloud, A.M. Bruton, K.P. Schwarz, "Detection and Filtering of Short Term (1/f) Noise in Inertial Sensor", *Journal of the Institute of the Navigation*, vol. 46, no. 2, pp. 97-108, 1999.

[25] A. Gelb, *Applied Optimal Estimation*, The M.I.T. Press, 1974.

[26] D.W. Allan, "Statistics of Atomic Frequency Standards", *Proceedings of IEEE*, vol. 54, no. 2, pp.221-230, 1966.

[27] M.M. Tehrani, "Ring Laser Gyro Data Analysis with Cluster Sampling Technique", *Proceedings of SPIE*, vol. 412, 1983.

[28] S. Han, J. Wang, "Quantization and Colored Noises Error Modeling for Inertial Sensors for GPS/INS Integration", *IEEE Sensors Journal*, vol. 11, no. 6, pp. 1493-1503, 2011.

[29] C. Jekeli, *Inertial Navigation Systems with Geodetic Applications*, Walter de Gruyter, 2001.

[30] X. Niu, Y. Li, H. Zhang, Q. Wang, Y. Ban, "Fast Thermal Calibration of Low-Grade Inertial Sensors and Inertial Measurement Units", *Sensors 2013*, vol. 13, no.9, pp. 12192-12217, 2013.

[31] S. Nassar , "Improving the Inertial Navigation Syste (INS) Error Model for INS and INS/DGPS Applications", Ph.D. Thesis, Department of Geomatics Engineering, University of Calgary, 2003.

[32] T.J. Ross, *Fuzzy Logic with Engineering Applications*, 3rd edition, Wiley, 2010.

APPENDIX A

INTRODUCTION TO RANDOM PROCESSES

General problem in linear system analysis is finding a relationship between input and output. Deterministic systems have obvious expressions to determine their response or output. This situation is not possible in random input-output problems. Random-input problems are defined with a small amount of descriptors. Random processes are defined with their autocorrelation function, power spectral density function, etc. In other words, these functions are important descriptors of a random process.

Stochastic errors are generally modeled as random processes. Modeling inertial sensor errors gives the opportunity to understand real behavior of an IMU in a dynamic system. Performance of an INS is directly related with true knowledge of stochastic error models of an inertial sensor [1, 4]. Stochastic errors have to be modeled as close as the real data to decrease INS position and velocity errors.

A.1 White Noise

White noise is a stochastic process which has a constant PSD function. Therefore, white noise effects on all frequency range. "White" term is derived from this property because white light contains all visible frequencies [23].

Autocorrelation function of a white noise can be given by,

$$R_w(\tau) = N\delta(\tau) \tag{A.1}$$

PSD function of white noise is calculated by Equation (4.7). It is given by,

$$S_w(jw) = N \tag{A.2}$$

For simplicity, it is assumed that spectral amplitude of white noise is unity. Equation (A.2) also gives some important outcomes because white noise can be used in linear time-invariant systems to extract minimum phase transfer function as described in detail at Section A.3.

A.2 Random Walk Process

Random walk process can be defined as follows: a man after taking k steps in arbitrary directions (e.g., backward and forward) with equal step size l, average distance is zero and standard deviation of this travel is $l\sqrt{k}$. The above discussion is explained as,

$$d = a_1 + a_2 + ... + a_k$$
$$d, total\ distance\ after\ taking\ k\ steps$$
$$E[a_n] = 0\ where\ n = 1, 2, ..., k$$

Mean value of each step is zero because if the experiment is repeated too much time each step has equal probability of being $-l$ or $+l$

$$E[a_i a_j] = 0\ where\ i \neq j$$
$$E[a_i a_j] = l^2\ where\ i = j$$

$$E[d^2] = E[a_1 a_1] + E[a_2 a_2] + E[a_3 a_3] + ... + E[a_k a_k] + 2(E[a_1 a_2] + E[a_1 a_3] + ...) \tag{A.3}$$

Last term in Equation (A.4) can be omitted. Variance calculation of distance is given in Equation (A.4). Thus, variance of distance is equals to $l^2 k$.

$$Var(d) = E[d^2] - E[d]^2$$
$$E[d^2] = l^2 k \qquad \text{(A.4)}$$
$$E[d]^2 = 0$$

In general, continuous time representation of random walk signal is the output of an integrator while input is white noise as shown in Figure 143.

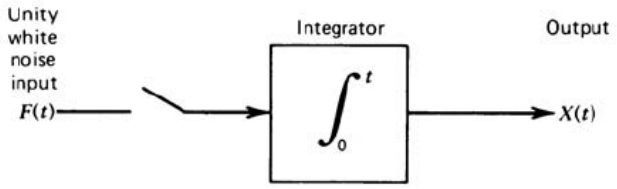

Figure 143 Block diagram of random walk generation [23].

According to Figure 143,

$$x(t) = \int_0^t F(m)dm$$
$$x(t), random\,walk\,process \qquad \text{(A.5)}$$

Mean value of the output is,

$$E[X(t)] = E\left[\int_0^t F(m)dm\right] = \int_0^t E[F(m)]dm = 0 \qquad \text{(A.6)}$$

Variance of this process is given by,

$$E[x^2(t)] = E[\int_0^t F(m)dm \int_0^t F(k)dk] = \int_0^t \int_0^t E[F(m)F(k)]dm\,dk \qquad \text{(A.7)}$$

$$E[F(m)F(k)] = R_F(m-k)$$
$$R_F(m-k), \textit{autocorrelation function of } F. \tag{A.8}$$

Autocorrelation function of white noise is a Dirac delta function [23]. Therefore, autocorrelation function given in Equation (A.8) can be rewritten as,

$$E[F(m)F(k)] = R_F(m-k) = \delta(m-k) \tag{A.9}$$

Substitution of Equation (A.9) into Equation (A.7) is stated below,

$$E[x^2(t)] = \int_0^t \int_0^t \delta(m-k)\,dm\,dk = \int_0^t dk = t \tag{A.10}$$

Resulting solution given in Equation (A.10) is very similar with Equation (A.4). Especially, correlated noises can be modeled as a random walk. This noise sources depend on the previous output due to the memory of excited electrons.

A.3 Gauss Markov Process

A process is first-order Gauss-Markov if probability distribution function only depends on one previous state of the process as shown in Equation (A.11).

$$t_1 < t_2 < \ldots < t_k \tag{A.11}$$
$$F[x(t_k) \mid x(t_{k-1}) \mid, \ldots, x(t_1)] = F[x(t_k) \mid x(t_{k-1})]$$
$$F[*], \textit{probability distribution function}$$

Gauss-Markov process is Gaussian process but it has an exponential autocorrelation [5]. Autocorrelation function of a Gauss-Markov process is given as,

$$R_x(\tau) = \sigma^2 e^{-|\tau|} \tag{A.12}$$

Computing the Fourier-Transform of autocorrelation function with Equation (4.7) gives Equation (A.13).

$$S_x(jw) = \int_{-\infty}^{\infty} \sigma^2 e^{-\beta|\tau|} e^{-jw\tau} d\tau \tag{A.13}$$

Due to the absolute value on tau (τ) we split into the integral in Equation (A.14) two parts which is expressed in the Equation (A.14).

$$S_x(jw) = \int_{-\infty}^{0} \sigma^2 e^{\beta\tau} e^{-jw\tau} d\tau + \int_{0}^{\infty} \sigma^2 e^{-\beta\tau} e^{-jw\tau} d\tau \tag{A.14}$$

$$S_x(j\omega) = \frac{2\sigma^2\beta}{\beta^2 + \omega^2} \tag{A.15}$$

Shaping filters are defined as a filter which converts its white noise input to desired spectral function. Shaping filters generally modifies input with minimum-phase transfer function. Analysis with white noise is simpler because PSD of white noise is unity and autocorrelation function of white noise is a Dirac delta function.

Figure 144: A simple shaping filter [3].

Gauss-Markov process can be considered as a shaping filter. PSD function of any linear time-invariant system is stated as,

$$S_x(j\omega) = H(j\omega)S_w(j\omega)H^*(j\omega) \tag{A.16}$$

"*" implies the complex conjugate operation. PSD function of a shaping filter is shown in Equation (A.17)

$$\begin{aligned} S_x(j\omega) &= 1.H(j\omega).H^*(j\omega) \\ S_w(j\omega) &= 1(PSD\,of\ white\,noise) \end{aligned} \tag{A.17}$$

PSD of shaping filter's output stated in (A.15). Transfer function of the shaping filter can be found according to Equation (A.17). Poles and zeros locations have to be on the left-hand side in the transfer function in order to obtain suitable shaping filter [23].

$$H(j\omega) = \frac{\sqrt{2\sigma^2\beta}}{\beta + j\omega}\ and\ H^*(j\omega) = \frac{\sqrt{2\sigma^2\beta}}{\beta - j\omega} \tag{A.18}$$

Shaping filter is stable system therefore we have to choose stable portion of the system response as indicated before and system transfer function is given as [23]:

$$T(s) = \frac{\sqrt{2\sigma^2\beta}}{\beta + s}\ for\ jw = s \tag{A.19}$$

$$\frac{x(s)}{w(s)} = \frac{\sqrt{2\sigma^2\beta}}{\beta + s} \tag{A.20}$$

$$x(s)(\beta + s) = w(s)\sqrt{2\sigma^2\beta} \tag{A.21}$$

Taking the inverse-Laplace transform gives the time-domain equation of the Gauss-Markov process.

$$\begin{gathered}\dot{x}(t) = -\beta x(t) + \sqrt{2\sigma^2\beta}\,w(t) \\ \omega(t) \sim N(0,1)\end{gathered} \tag{A.22}$$

$$y(t) = x(t) \tag{A.23}$$

$$\beta = \frac{1}{T_c} \tag{A.24}$$